NASA/TP-2004-212686

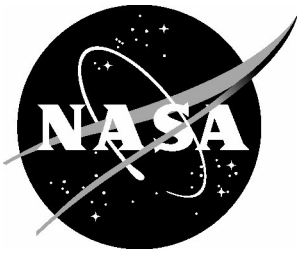

Supersonic Jet Exhaust Noise at High Subsonic Flight Speed

Thomas D. Norum, Donald P. Garber, Robert A. Golub, and Odilyn L. Santa Maria
Langley Research Center, Hampton, Virginia

John S. Orme
Dryden Flight Research Center, Edwards, California

January 2004

The NASA STI Program Office . . . in Profile

Since its founding, NASA has been dedicated to the advancement of aeronautics and space science. The NASA Scientific and Technical Information (STI) Program Office plays a key part in helping NASA maintain this important role.

The NASA STI Program Office is operated by Langley Research Center, the lead center for NASA's scientific and technical information. The NASA STI Program Office provides access to the NASA STI Database, the largest collection of aeronautical and space science STI in the world. The Program Office is also NASA's institutional mechanism for disseminating the results of its research and development activities. These results are published by NASA in the NASA STI Report Series, which includes the following report types:

- TECHNICAL PUBLICATION. Reports of completed research or a major significant phase of research that present the results of NASA programs and include extensive data or theoretical analysis. Includes compilations of significant scientific and technical data and information deemed to be of continuing reference value. NASA counterpart of peer-reviewed formal professional papers, but having less stringent limitations on manuscript length and extent of graphic presentations.

- TECHNICAL MEMORANDUM. Scientific and technical findings that are preliminary or of specialized interest, e.g., quick release reports, working papers, and bibliographies that contain minimal annotation. Does not contain extensive analysis.

- CONTRACTOR REPORT. Scientific and technical findings by NASA-sponsored contractors and grantees.

- CONFERENCE PUBLICATION. Collected papers from scientific and technical conferences, symposia, seminars, or other meetings sponsored or co-sponsored by NASA.

- SPECIAL PUBLICATION. Scientific, technical, or historical information from NASA programs, projects, and missions, often concerned with subjects having substantial public interest.

- TECHNICAL TRANSLATION. English-language translations of foreign scientific and technical material pertinent to NASA's mission.

Specialized services that complement the STI Program Office's diverse offerings include creating custom thesauri, building customized databases, organizing and publishing research results ... even providing videos.

For more information about the NASA STI Program Office, see the following:

- Access the NASA STI Program Home Page at ***http://www.sti.nasa.gov***

- E-mail your question via the Internet to help@sti.nasa.gov

- Fax your question to the NASA STI Help Desk at (301) 621-0134

- Phone the NASA STI Help Desk at (301) 621-0390

- Write to:
  NASA STI Help Desk
  NASA Center for AeroSpace Information
  7121 Standard Drive
  Hanover, MD 21076-1320

NASA/TP-2004-212686

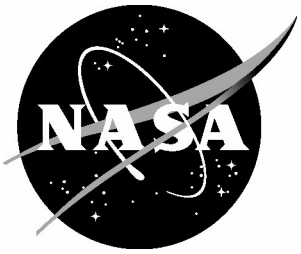

Supersonic Jet Exhaust Noise at High Subsonic Flight Speed

Thomas D. Norum, Donald P. Garber, Robert A. Golub, and Odilyn L. Santa Maria
Langley Research Center, Hampton, Virginia

John S. Orme
Dryden Flight Research Center, Edwards, California

National Aeronautics and
Space Administration

Langley Research Center
Hampton, Virginia 23681-2199

January 2004

Available from:

NASA Center for AeroSpace Information (CASI)
7121 Standard Drive
Hanover, MD 21076-1320
(301) 621-0390

National Technical Information Service (NTIS)
5285 Port Royal Road
Springfield, VA 22161-2171
(703) 605-6000

Abstract

An empirical model to predict the effects of flight on the noise from a supersonic transport is developed. This model is based on an analysis of the exhaust jet noise from high subsonic flights of the F-15 ACTIVE Aircraft. Acoustic comparisons previously attainable only in a wind tunnel were accomplished through the control of both flight operations and exhaust nozzle exit diameter. Independent parametric variations of both flight and exhaust jet Mach numbers at given supersonic nozzle pressure ratios enabled excellent correlations to be made for both jet broadband shock noise and jet mixing noise at flight speeds up to Mach 0.8. Shock noise correlated with flight speed and emission angle through a Doppler factor exponent of about 2.6. Mixing noise at all downstream angles was found to correlate well with a jet relative velocity exponent of about 7.3, with deviations from this behavior only at supersonic eddy convection speeds and at very high flight Mach numbers. The acoustic database from the flight test is also provided.

Introduction

The F-15 ACTIVE Aircraft Acoustics Flight Test was performed in the fall of 1997 at NASA Dryden Flight Research Center. The test was developed to improve the understanding of the effects of high subsonic flight speed on the generation and propagation of aircraft jet exhaust noise, with application to the acoustic footprint of the flight of a High Speed Civil Transport during climb to cruise. It was a cooperative effort involving NASA Dryden Flight Research Center and NASA Langley Research Center, together with major American aircraft engine and airframe manufacturers.

A flight test six years earlier provided the aeroacoustics community with some relevant flight data (ref. 1). This previous test was also performed at Dryden and consisted of flights of F-18 and F-16 aircraft. Some control over flight conditions useful to acoustic testing was obtained for the F-18 by maintaining one of the two engines at flight idle. However, because the F-16 has only one engine, that same level of control was unattainable for this aircraft, resulting in undesirable aircraft acceleration during flyovers. Nevertheless, enough useful acoustic data were obtained during this test to show that the theory of the effects of flight on simple acoustic sources was insufficient to predict the observed trends in the data (ref. 2).

The ensuing years brought the development of actively controlled exhaust nozzles for an F-15 aircraft to extend thrust vectoring capability to high speed flight (ref. 3). This nozzle was also seen as an ideal tool for obtaining variations of the nozzle internal geometry that are required to parametrically study the effects of flight on supersonic jet exhaust noise, resulting in the F-15 ACTIVE Aircraft Acoustic Flight Test.

For the F-15 flight test, nozzle control was combined with flight procedures that incorporated small angle climbs or dives designed to maintain constant flight speed during the time the aircraft was traversing the acoustic measuring range, resulting in test data, which through a unique data reduction procedure, have generated an excellent acoustic database for equivalent level high speed flyovers at parametrically varied aircraft speed and nozzle conditions. The acoustic spectra of the database are presented in this report, along with major findings regarding effects of high subsonic flight speed on supersonic jet mixing

noise and broadband shock noise. Preliminary studies of these data were undertaken in references 4 and 5.

Nomenclature

ALT	nominal aircraft altitude above ground level, ft
A_e	nozzle exit area, ft2
A_8	nozzle throat area, ft2
c_f	ambient speed of sound at flight altitude, ft/s
D	Doppler factor, $1 - M_f \cos \psi$
DGPS	Global Positioning System (with differential corrections)
F_g	nozzle gross thrust, lbf
INS	Inertial Navigation System
M_e	nozzle exit Mach number
M_f	aircraft flight Mach number
M_j	fully expanded jet Mach number
M_{rel}	jet relative Mach number, V_{rel}/c_f
m	exponent; slope of straight line curve fit
NPR	nozzle pressure ratio
OASPL	overall sound pressure level to frequency of 1.5 kHz, dB
OASPL_{SN}	OASPL for shock noise correlation, normalized by $\beta' M_j^{5.5}$, dB
PLA	power lever angle, deg
PSD	noise source power spectral density (1 Hz bandwidth), dB
p_a	ambient pressure at flight altitude, psia
p_e	nozzle exit static pressure, psia
p_8	exhaust nozzle total pressure, psia
R	source to observer distance at noise emission time, ft

R_r source to observer distance at noise reception time, ft

T_a ambient temperature at flight altitude, deg R

T_8 nozzle exhaust total temperature, deg R

V_e nozzle exit velocity when nozzle divergent section is shock free, ft/s

V_f aircraft flight velocity, ft/s

V_j fully expanded jet velocity, ft/s

V_{rel} jet relative velocity, $V_j - V_f$, ft/s

w_8 exhaust gas mass flow rate, lbm/s

β' shock strength parameter, $\sqrt{\left|M_e^2 - M_j^2\right|}$

γ exhaust gas specific heat ratio

σ standard deviation from straight line fit

ψ emission time observer angle measured from upstream direction, deg

ψ_r reception time observer angle measured from upstream direction, deg

Flight Operations

A photograph of the F-15 ACTIVE Aircraft in flight is given in figure 1. The aircraft is powered by two Pratt & Whitney F-100 engines. To reduce thrust and hence the tendency of the aircraft to accelerate at the desired acoustic test conditions, it was decided that the right engine would be maintained at flight idle during most of the testing. Prior to the flight test, good estimates of conditions that could be flown were obtained by using the engine operating deck and the F-15 ACTIVE simulation facility. The small climb/dive angle of the aircraft required to maintain the desired constant speed at a given engine condition and given nominal altitude was thus obtained prior to the actual flight.

A typical flyover began with both engines at the desired condition and the aircraft accelerating/decelerating as it approached the test range at an altitude somewhat lower/higher than the desired nominal altitude. Just prior to reaching the acoustic array, the pilot would bring the right engine throttle to flight idle and pitch to the climb/dive angle required to maintain a constant velocity at that engine condition. The left engine throttle setting and aircraft speed were maintained constant throughout the acoustic range, with the aircraft passing through the nominal altitude when directly over the center of this range. The maximum climb angle was about 15°.

Test Conditions

For the typical military fighter aircraft, standard engine operation at subsonic flight speeds and low altitude requires that the supersonic exhaust nozzle be operated in the overexpanded mode, resulting in the nozzle exit static pressure being lower than the ambient pressure. This lower pressure results in shocks within the jet plume and acoustic emission in the direction forward of the aircraft being dominated by jet broadband shock noise (ref. 2). Since the strength of the shock structure is dependent on both nozzle pressure ratio and ratio of nozzle exit to throat areas, the ability to change this area ratio allowed some control of the overexpansion. However, because the extent of this control was seldom large enough to obtain a fully expanded nozzle for the desired engine conditions, most runs were made with overexpanded exhaust flow.

The nozzle area ratio was controlled by varying the nozzle exit diameter. For most flights, this ratio was maintained at its smallest allowable setting to minimize the degree of overexpansion of the exhaust jet of the powered engine. Larger exit areas were set to increase overexpansion during the sequence of runs that were expressly aimed at evaluating jet broadband shock noise.

There were eight series of runs performed during the test, labeled as the 100 series through the 800 series. The 100 series of runs was aimed at measuring exhaust jet mixing noise at a typical takeoff Mach number (0.32) over a range of low nozzle pressure ratios (1.2 to 2.4). In the 200 series, an aircraft Mach number (0.32 to 0.90) versus NPR (2.2 to 4.8) schedule was chosen as typical of an aircraft climbout from takeoff to cruise. The 300 series was aimed at evaluating low altitude noise propagation at a typical takeoff condition. The 400, 500, and 600 series of runs were aimed at evaluating broadband jet shock noise by holding NPR constant and using parametric variations of both nozzle exit area and aircraft Mach number, attainable by changing the climb angle for the different flight speeds. The 700 series had both engines operating at the same power setting and used the yaw vectoring ability of the exhaust nozzles to determine the effect of nonparallel exhaust jets. Finally, the 800 series was run at very high NPR (4.3) and flight Mach number (0.9) as the only part of the engine operating range that allowed for an underexpanded exhaust jet at reasonably low altitude.

Ten flights were conducted on five days, consisting of early- and mid-morning flights on 9/19, 9/23, 9/24, 10/2, and 10/3/97. (The week layoff in between was caused by a rare Mojave Desert hurricane.) In all, 52 different operating conditions were tested, with many being repeated, for a total of 92 runs. Table 1 lists flight and engine parameters for all runs. Runs were numbered by objective, not chronological order.

Weather and Tracking Data

Weather data for propagation modeling were obtained from two sources. The primary source was a series of rawinsonde soundings that provided pressure, temperature, humidity, wind speed, and wind direction as a function of altitude. Density was calculated from temperature, pressure, and humidity. The soundings were made before and after most of the flights. Because rawindsonde soundings are made by tracking the relatively slow ascent of a balloon carrying an instrument package, altitude measurements are a function of time. The second source of weather data was a 10-m tower, located near the microphones, that provided continuous measurements of temperature, wind speed, and wind direction at a variety of locations along its height. Weather changes continuously, so the tower data were used to determine whether to interpolate between rawinsonde releases (when tower data indicated gradual weather changes between runs) or to use a single rawindsonde release (when tower data indicated an abrupt weather transition between runs).

Tracking data were derived from three independent sources: an Inertial Navigation System (INS), a Global Positioning System with differential corrections (DGPS) for enhanced accuracy, and C-band radar, each sampled at a rate of two samples per second. The INS was used only for pitch, roll, and yaw attitude data. The DGPS provided the most accurate position data but did not work all the time. DGPS data were used when they were available. Radar data were always available but were used only when DGPS was unavailable. Small but systematic differences between DGPS and radar were observed when both were working, so a correction based on those differences was applied to the radar to improve its accuracy.

Acoustic Data Acquisition and Reduction

The acoustic data were obtained from an array of 20 equally spaced 0.5-in. condenser microphones placed on 6-ft wooden ground boards located directly under the flight path. The separation distance between microphones was 300 ft. Narrowband spectra at various emission angles were obtained by ensemble averaging 0.5-s spectra derived from each microphone by the following procedure.

As detailed in appendix A, a ray-tracing procedure was used to determine the propagation path of sound from each aircraft tracking position to the position of each of the 20 microphones. The aircraft attitude data and the resultant ray directions were used to obtain acoustic emission angles and corresponding emission times associated with each combination of tracking position and microphone number. Acoustic emission angle versus emission time data were then interpolated to determine the acoustic emission time and aircraft position associated with specified emission angles (that ranged from 30° to 160° in steps of 5°) for each microphone. The same ray-tracing procedure was then used to determine reception time and (frequency dependent) propagation losses for each combination of emission angle and microphone number. A 0.5-s power spectrum was calculated for each of the microphones at each of the reception times associated with the specified emission angles. Calculated propagation and ground board effects were then removed to transform received spectra to emitted spectra at a reference distance of 1 ft. For each emission angle, the emitted spectra for all microphones were averaged to generate an ensemble-averaged narrowband source spectrum which was then normalized to 1-Hz bandwidth. All acoustic results presented in this report are from these stationary far-field observer power spectral densities at a given emission angle that has been propagated back to the aircraft.

Power spectral densities are shown in appendix B for most runs. Repeat runs are overlaid to show the repeatability of the acoustic data. The spectra are given for emission angles as measured from the flight direction of 30° to 160° in 10° intervals. Also shown is the overall sound pressure level directivity computed from these spectra. Frequency is limited to 1.5 kHz because of the behavior that commonly arises at high frequency when measured flight spectra are propagated back to the source. This behavior, resulting from large atmospheric absorption corrections, consists of rising spectrum levels above 1 kHz that can be seen in the spectra at the extreme emission angles (i.e., the longest propagation paths). Two known reasons that could cause these rising levels include dynamic range limitations of the instrumentation and nonlinear propagation of the source noise. However, for the current experiments, the large dynamic range of the digital recordings precludes the former, and that the rising spectral behavior is enhanced as the flight speed increases, gives one doubt that the latter is the sole cause of this behavior. The actual cause for the rising spectra is unknown.

Analysis of Acoustic Data

Typical of high speed turbojet engines, the dominant noise measured during the F-15 flyovers consisted of exhaust jet broadband shock noise and jet mixing noise. Because both sources are broadband in nature, the overall sound pressure level (OASPL) is chosen as the best parameter to correlate the noise

data. Given that the measured peak frequencies of both sources are below 1 kHz, the OASPL that is computed by ignoring contributions above 1.5 kHz is a good representation of the true OASPL and is the value used in the data comparisons that follow.

Because the 400, 500, and 600 series of runs were specifically designed for shock noise studies, much of the acoustic analysis will concentrate on these series. Each of these series was divided into two subseries, denoted as the low and high series. For example, runs between 400 and 440 were in the low 400 series and those between 450 and 490 were in the high 400 series. Within each of the six subseries, flight speed was varied while attempting to keep constant both nozzle exit Mach number (i.e., the nozzle area ratio) and fully expanded jet Mach number (i.e., the nozzle pressure ratio). Because of constraints on the flight envelope and engine operating conditions at the low altitudes required for best acoustic measurements, only a small range of values was possible for the fully expanded Mach number during the shock noise studies.

The nominal conditions and the average of actual conditions for the six subseries of runs are given in table 2. Because supersonic jet broadband shock noise has been correlated in the past (ref. 6) with M_j, M_e, and the shock strength parameter $\beta' = \sqrt{\left|M_e^2 - M_j^2\right|}$, these parameters were controlled as follows. All 400 series runs had a nominal $M_j = 1.36$ and all 500 series runs had a nominal $M_j = 1.46$. Both low series had the same nominal $\beta' = 0.67$, and both high series had the same nominal $M_e = 1.71$. The 600 series had the same nominal exhaust conditions as the 500 series but had a higher nominal flight altitude.

A qualitative assessment of the effects of flight on noise spectra generated by an overexpanded jet can be seen in comparisons of figure 2 for data from the high 500 series. For this series, the nominal nozzle exit and jet fully expanded Mach numbers were 1.74 and 1.46, respectively. Spectra are shown for eight angles along with the OASPL directivity at flight Mach numbers of 0.46, 0.61, and 0.77. Because both the nozzle operating condition and the nozzle geometry were the same for the three runs, the figure shows the effect of flight Mach number on the noise from a given nozzle exhaust.

In the direction upstream of the aircraft ($\psi < 90°$), the spectra are dominated by broadband shock noise with a primary broadband peak at 500 to 700 Hz. As the flight Mach number increases, so do the spectral amplitudes, corresponding to a convective amplification of the shock noise. Near 90° only minor changes occur with flight speed. Here the broadband shock noise is still dominant, having a wider bandwidth and a spectral peak closer to 800 Hz. At 105° jet broadband shock noise (peaking at 1000 Hz) and jet mixing noise (comprising the lower frequency portion of the spectra) are seen to be comparable. Finally, in the downstream direction ($\psi > 120°$) the spectrum is dominated by mixing noise rather than shock noise. Mixing noise amplitudes decrease with flight speed, primarily due to the reduction of relative velocity between the exhaust jet and the ambient air. The last frame of figure 2 again shows that the effects of flight on the OASPL directivity are opposite in the upstream and downstream directions.

The consistency of this behavior for each of the four subseries of 400 and 500 runs is seen in the OASPL directivities at four flight speeds in figure 3. As in figure 2, upstream propagating shock noise is clearly amplified as flight speed increases, whereas downstream propagating mixing noise has a maximum near 140° and decreases in amplitude as flight speed increases. The angle at which the spectra switch from shock noise dominance to mixing noise dominance is approximately 105°. Hence, in the analysis of the jet noise to follow, broadband shock noise is assumed to produce the OASPL below 90° emission angle and mixing noise is assumed to produce the OASPL above 120° emission angle.

Jet Broadband Shock Noise

As is evident in figure 3, the dominant effect of flight on radiated broadband shock noise is the increase in noise level in the forward direction with flight speed. It is generally agreed that this increase in the propagated noise, called convective or dynamic amplification, can be modeled as a function of the Doppler factor in the form $(1 - M_f \cos \psi)^{-m}$, where m is an integer. Various theories and empirical formulations have chosen different values for the exponent m. Mani (ref. 7) and Tanna, Dean, and Burrin (ref. 8) chose $m = 4$, which is the exponent for the theoretical acoustic monopole in motion, and Stone (ref. 9) used $m = 1$ for his data correlations. In the more recent theory of Tam (ref. 6) this exponent is hidden by the use of source coordinates rather than the more customary observer coordinates. However, as shown in appendix C, when Tam's formulation is transformed to observer coordinates, his predicted amplification is equivalent to the Doppler factor with an exponent $m = 2$.

The broadband shock noise OASPL is correlated with the Doppler factor in figure 4 for the low 400 series, in figure 5 for the high 400 series, in figure 6 for the low 500/600 series, and in figure 7 for the high 500/600 series. (Note that although the 500 and 600 series had markedly different flight altitudes, the acoustic results have been propagated back to the aircraft so that the two series can be analyzed together.) These figures consist of plots for each of the four flight Mach numbers. In that flight Mach number is constant, the variation in the Doppler factor in each plot is due to changes in the noise emission angle. Also shown are the computed least squares straight lines. These lines fit the data well, although there are indications of less gradual increases in OASPL at the upstream angles than at angles close to 90°. The slope of the line m, which corresponds to the Doppler factor exponent, and the standard deviation of the data from the straight line fits σ, are given on each plot. The exponent m lies between 2 and 3 for all but one of the 16 plots, and the average standard deviation is 0.5 dB, which indicates an excellent correlation of the shock noise with Doppler factor. The average slope is $m = 2.5$, which is close to the Tam prediction $m = 2$.

The correlations in figures 4 through 7 show the variations in OASPL with the Doppler factor as the noise emission angle is changed. To see the corresponding variations as the flight Mach number is changed, the OASPL needs to be corrected because both nozzle and engine conditions could only be held nominally constant as the flight Mach number was varied. This correction is accomplished by independent evaluations of the variations in OASPL due to changes in β' and M_j as follows.

In the predictions of Tam, β' to the fourth power is the factor that has the strongest influence on the amplitude of broadband shock noise. The influence of β' on the flight data can be determined directly from comparisons of OASPL between the low subseries and the high subseries of any of the three series of runs. For these comparisons, exhaust nozzle pressure ratio and nozzle throat area are held constant while the exit area is changed, resulting in a change in β' due to a change in nozzle exit Mach number at a constant fully expanded jet Mach number. An example of these comparisons is given in figure 8, which shows OASPL directivities for the low and high 400 series of runs for each of the four flight Mach numbers. As expected, the jet mixing noise that dominates the downstream direction is unchanged because both the flight and fully expanded jet velocities are the same for each pair of runs being compared. In the upstream direction, greater shock noise results from the higher nozzle exit Mach numbers of the high subseries, which yield larger values of β' and a stronger shock structure in the jet plume.

A calculation based on the magnitude of the increase in OASPL with β' shows that the noise level difference is a function of the first power of β' rather than the fourth power, as proposed by Tam's theory (ref. 6), which can be seen in figure 9 where the noise directivities given in figure 8 are repeated with the OASPL normalized by the first power of β'. The resulting agreement of the upstream noise data is seen

to be excellent. The shock noise dependence on the first power of β' is further confirmed by a similar comparison between the low and high 500 series in figure 10.

In addition to a dependence on β', Tam's prediction for the amplitude of shock noise contains other factors involving the fully expanded velocity and/or fully expanded Mach number. To judge the influence of these other factors on the shock noise, the OASPLs of the low 400 series and low 500 series are compared at each of the four flight Mach numbers in figure 11. For each pair of runs compared, although the fully expanded Mach number is different, β' is kept relatively constant by increasing the nozzle exit diameter (and hence increasing M_e) as M_j is increased. Here both the downstream jet mixing noise and the upstream jet shock noise increase because of the increasing fully expanded jet velocity.

In an attempt to quantify the increase in shock noise due to the higher jet velocity, the OASPL at 90° and its value normalized by 10 log β' are correlated with both the fully expanded Mach number and fully expanded velocity in figure 12 for all runs in the 400 through 600 series.

Three things can be noted from the plots in figure 12. First, by comparing the left and right plots, the normalization of OASPL by the first power of β' does result in considerably less scatter around the straight line fit. Second, comparing the standard deviations of the two plots on the right indicates that fully expanded Mach number does better than velocity in correlating the data. Third, the power of the fully expanded Mach number that best correlates the broadband shock noise for these runs is the slope of the top right plot, which is 5.5 (rounded to the nearest 1/2 power).

Normalizing the data of figure 11 by M_j to the 5.5 power gives the directivities shown in figure 13. This figure shows that good agreement between normalized upstream noise levels is attained at all four flight Mach numbers.

Having shown the broadband shock noise amplitude can be correlated well by the product $\beta' M_j^{5.5}$, the influence of increasing flight Mach number on the dynamic amplification of this noise can now be determined. The normalized broadband shock noise $\mathrm{OASPL_{SN}}$, defined as

$$\mathrm{OASPL_{SN}} = \mathrm{OASPL} - 10 \log \beta' - 55 \log M_j \tag{1}$$

is shown at 9 angles from 30° through 70° versus the Doppler factor in figure 14. The results from all 44 runs in the 400/500/600 series are shown, with the variation in each plot indicating the effect of increasing flight Mach number at a given emission angle. The slope of the straight line fit, corresponding to the Doppler factor exponent, varies between 2.7 and 3.4, with the exponent increasing slightly as 90° is approached. The average of the standard deviation of the data is about 0.6 dB, again indicating excellent fit to the data. The average value of the Doppler factor exponent obtained from the flight Mach number variations is about 3.0, slightly higher than the value 2.5 that was obtained from the angle variations.

The effects of flight on jet broadband shock noise due to both flight Mach number and angle variations are combined in figure 15. The normalized OASPL versus Doppler factor is given for 528 data points consisting of all 44 runs at 5° increments from 35° to 90°. The straight line fit of the data from the over-expanded F-15 exhaust jets yields a broadband shock noise Doppler factor exponent of 2.6, with a standard deviation of 0.7 dB and an intercept of 155 dB.

The Doppler exponent obtained from the flight data indicates that the amplification given by $m = 4$, as obtained from the computation of a monopole in motion, overestimates broadband shock noise in flight

and also shows that the value of $m = 2$, which is applicable to Tam's prediction, is closer to the data than are other predictions.

In summary, by combining the results of figure 15, along with the previously found dependency of OASPL on β' and M_j, suggests that the source amplitude of the F-15 exhaust jet broadband shock noise in flight can be written as

$$< p^2 >_{\text{shock noise}} = 10^{15.5}\, \beta' M_j^{5.5} (1 - M_f \cos \psi)^{-2.6} \tag{2}$$

Comparison of Flight Spectra With Tam's Predictions

Tam's theory also provides a prediction of the broadband shock noise spectra. Comparisons of these predicted spectra with measured flight data are given in figures 16 and 17 for the low 400 series, at lowest and highest flight Mach numbers, respectively. As evident from the figures, the predictions yield a series of modes whose peak amplitudes decrease with increasing frequency. As the observer angle increases, the peak amplitude decreases and its frequency increases, in agreement with the measurements. These spectral comparisons are similar to those reported from the previous flight test of an F-18 aircraft (ref. 1). Comparisons for other runs in the 400 and 500 series show similar agreement.

Additional comparisons of measured and predicted spectra are given in figures 18 and 19 for data from the 800 series. This series contains the only pair of flights in which the nozzle exit area was able to be sufficiently varied at a given nozzle pressure ratio to obtain not only the usual highly overexpanded exhaust jet, but also a slightly underexpanded jet. Figure 18 presents spectra for the former case, where $\beta' = 0.86$, and figure 19 gives spectra for the latter case, where $\beta' = 0.27$.

Although figure 18 shows the good agreement between the predicted and measured spectral amplitude, the near fully expanded spectra of figure 19 show a significant underprediction. The values of the broadband shock noise primary mode spectral peak of the measured data show an average difference of about 4 dB between the two figures, versus about an 11 dB difference between the predicted values. This result indicates that when flying close to the fully expanded condition, real convergent-divergent nozzles can contain more shock noise than Tam predicts.

The broadband shock noise level dependence on the first power of β' that was found previously accounts for this measured noise level difference. It predicts the shock noise difference to be 10 log (0.86/0.27), or about 5 dB, which is very close to the measured peak spectral differences between figures 18 and 19.

A strong indication that the results of figure 19 for a slightly underexpanded jet hold equally well for a slightly overexpanded jet can be obtained from run 632. Unlike all the other runs during the flight test, the pilot used a throttle setting for run 632 that was somewhat higher than planned, which resulted in a higher than desired fully expanded velocity and a slight acceleration from the planned flight Mach number of 0.77 upstream of the microphones to an overhead value of 0.81. Because of the accelerated flight, the spectra from this run are not given in the acoustic database in appendix B, nor were they used in the analysis of the data in this report. However, because this pilot error yielded the only run with a slightly overexpanded exhaust jet, the measured acoustic results are given in figure 20 along with Tam's prediction for an assumed constant velocity equal to the overhead flight velocity. Note that the nozzle conditions of figures 19 and 20 yield the same degree of nonperfect expansion ($\beta' = 0.27$). An overlay of the two figures shows equivalent differences between the measured and predicted primary broadband shock noise peak levels. Figure 20 data lead to the conclusion that the Tam prediction underestimates the

broadband shock noise level for slightly overexpanded jets by the same amount that it does for slightly underexpanded jets.

Jet Mixing Noise

By explicitly expressing only the effects of flight velocity and the most dominant effects of fully expanded jet velocity on exhaust jet mixing noise, the mean square acoustic pressure at a given far-field distance from the nozzle is commonly expressed as (ref. 10):

$$< p^2 >_{\text{mixing noise}} = \frac{C V_j^n}{1 - M_f \cos\psi} \left(\frac{V_j - V_f}{V_j} \right)^{m(\psi)} \tag{3}$$

where the factor C contains additional parameters that are only weakly dependent on V_j. At static conditions equation (3) reduces to CV_j^n, where $n = 8$ gives the well known V^8 law for subsonic jets.

Attempts to assess the exponents n and m from the F-15 flight data led to the conclusion that the best correlation of the effects of flight can be obtained by setting $n = m$, which is equivalent to assuming that the correct noise variation can be obtained by replacing the jet velocity in the static case by the relative velocity, $V_j - V_f$, in the flight case. That this relationship correlates the jet mixing noise well can be seen from the measured noise data from the 100 series, during which the aircraft was maintained at the nominal flight Mach number 0.34, while the jet Mach fully expanded number was varied from 0.8 to 1.2. Data from the 100 series and the very low altitude 300 series (flown at the same flight Mach number of 0.34) are given in figure 21. Shown is the OASPL (normalized for the Doppler factor via eq. (3)) versus the jet relative Mach number (jet relative velocity nondimensionalized by the ambient sound speed) for $\psi = 120°$ to 160°. The relative Mach number ranged between 0.7 and 1.4 for these data. The slope of the straight line fit through the data represents the relative velocity exponent m. Excellent correlations (average $\sigma < 0.4$) are obtained, with a relative velocity exponent m varying between 6.7 and 7.7 over the entire range of downstream observer angles.

Figure 22 extends this correlation to the remaining low altitude data (the 400 and 500 series). Beyond the smallest angles the correlation is not good, with standard deviations from the curve fit greater than 1 dB. The reason for the absence of the excellent straight line fit of figure 21 is due to the change in the peak directivity angle of the mixing noise that was previously seen in figure 3. At a flight Mach number of 0.34, the peak directivity angle of the 400 and 500 series data is 135°, while the 100 series of runs have peak directivities closer to 145°. This change in the peak directivity angle likely results from the exhaust jet relative Mach number of the former being above 1.6, while the 100 series have relative Mach numbers less than 1.4. It is within this relative Mach number range that the convection velocity of the noise sources becomes supersonic, transforming the dominant jet mixing noise source from subsonic type mixing noise to Mach wave radiation. The result is a shift in peak directivity to smaller angles in the same manner as for a model static jet when supersonic convection velocities are reached by increasing jet temperature.

However, because the exhaust jet relative velocity decreases as the flight speed is increased, runs in the 400/500 series at higher flight Mach numbers have lower jet relative Mach numbers. Using the data for all low altitude flyovers at flight Mach numbers below 0.7 and jet relative Mach numbers up to 1.5 gives the correlations of figure 23. Good correlation of the jet mixing noise data is again obtained. A relative velocity exponent $m = 7.3$ and an average σ of about 0.7 dB are obtained. Hence, the good correlation of the jet mixing noise with relative jet velocity is maintained for flight Mach numbers up to

0.7 as long as the relative Mach number is below 1.5. (However, in addition to the OASPL for jet relative Mach numbers above 1.5 being below the curve fit, as seen in fig. 22, the OASPLs from the highest flight Mach number (0.77) fall above the curve fit and hence are not included in fig. 23.)

Figure 23 shows that the effects of flight on the exhaust jet mixing noise of the F-15 for all angles from 120° through 160°, flight Mach numbers between 0.3 and 0.7, and jet relative Mach numbers between 0.7 and 1.5, are well correlated by

$$< p^2 >_{\text{mixing noise}} = \frac{C}{1 - M_f \cos\psi} \left(\frac{V_j - V_f}{c_j} \right)^{7.3} \tag{4}$$

Concluding Remarks

The F-15 ACTIVE Aircraft Acoustics Flight Test has produced an excellent database for investigating the effects of high speed flight on the exhaust noise from overexpanded axisymmetric jets. A wide range of constant flight speeds was realized at a given engine and nozzle setting through the use of different aircraft climb angles. Through ensemble averaging of an array of ground-based microphones, unique data processing was used to obtain the noise from equivalent level flyovers at constant aircraft velocity. Aircraft attitude and weather measurements were incorporated to produce noise source spectra that show excellent agreement between flyovers at different altitudes. The measured spectra were dominated by jet broadband shock noise in the upstream direction and by jet mixing noise in the downstream direction. These results allowed for an evaluation of the effects of flight on both these components of nozzle exhaust jet noise.

The influence of the important parameters governing supersonic jet broadband shock noise production was able to be separated by the ability to control the exhaust nozzle exit area of the F-15 ACTIVE Aircraft, which allowed for independent evaluation of the influence of the fully expanded Mach number and the shock strength parameter β', enabling the effects of flight Mach number to be consistently evaluated. Results indicate that variations in the noise level at all upstream angles (35° to 90°) and flight Mach numbers (0.33 to 0.77) can be accounted for by a 2.6 power of the Doppler factor, which is closer to that predicted by Tam (shown in appendix C to be equal to 2) than to those of other theories. However, the F-15 data indicate that the shock noise amplitude has a smaller variation with the shock strength parameter β' than predicted by Tam's theory.

The effects of flight speed on supersonic jet mixing noise from the F-15 were found to be best correlated by simply replacing the jet absolute velocity by the jet relative velocity. A jet relative velocity exponent close to 7.3 was found for all observer angles beyond 120° and for flight Mach numbers to 0.7. This correlation proved to be excellent up to a jet relative Mach number of 1.5, beyond which the noise is likely dominated by Mach wave radiation.

References

1. Kelly, J. J.; Wilson, M. R.; Rawls, J., Jr.; Norum, T. D.; and Golub, R. A.: *F-16XL and F-18 High Speed Acoustic Flight Test Databases*. NASA/TM-1999-209529, 1999.

2. Norum, T. D.; Golub, R. A.; and Willshire, W. L.: Comparisons of Shock Noise Predictions With Flight Data. *First NASA/Industry High Speed Research Program Nozzle Symposium*. Long Davis, M. J., ed., Cleveland, Ohio, Nov. 17–19, 1992, pp. 30-1–30-13.

3. Doane, P.; Bursey, R.; and Schkolnik, G. S.: F-15 ACTIVE: A Flexible Propulsion Integration Testbed. AIAA 94-3360, June 1994.

4. Wat, J. K.; Yamamoto, K. J.; Golub, R. A.; and Garber, D. P.: Comparison of Jet Mixing Noise Predictions With Data at High Subsonic Mach Number. AIAA 99-1969, June 1999.

5. Wat, J.; Yamamoto; K.; and Golub, R.: Jet Shock Noise at High Subsonic Flight. AIAA 2000-1957, June 2000.

6. Tam, C. W. K.: Broadband Shock-Associated Noise From Supersonic Jets in Flight. *J. Sound & Vib.*, vol. 151(1), 1991, pp. 131–147.

7. Balsa, T. F.; Gliebe, P. R.; Kantola, R. A.; Mani, R.; Stringas, E. J.; and Wang, J. F. C.: *High Velocity Jet Noise Source Location and Reduction, Task 2—Theoretical Developments and Basic Experiments*. FAA-RD-76-79-2, II, May 1977. (Available from DTIC as AD A094 291.)

8. Tanna, H. K.; Dean, P. D.; and Burrin, R. H.: The Generation and Radiation of Supersonic Jet Noise, Volume IV—*Shock-Associated Noise Data*. AFAPL-TR-76-65, Vol. IV, U.S. Air Force, Sept. 1976. (Available from DTIC as AD A032 883.)

9. Stone, J. R.: Supersonic Jet Shock Noise Reduction. AIAA 84-2278, Oct. 1984.

10. Zorumski, W. E.: *Aircraft Noise Prediction Program Theoretical Manual*. NASA TM-83199, Pt. 2, 1982.

11. Pierce, A. D.: *Acoustics*. Acoustical Society of America, New York, 1989.

12. ANSI S1.26-1978: *American National Standard Method for the Calculation of the Absorption of Sound by the Atmosphere*. American National Standards Institute, New York, 1978.

13. Bass, H. E.; Sutherland, L. C.; and Zuckerwar, A. J.: Atmospheric Absorption of Sound: Update. *J. Acoust. Soc. Am.*, vol. 88, no. 4, Oct. 1990.

14. Roy, D.: Doppler Frequency Shift for Aircraft Noise in a Refractive Atmosphere. AIAA 84-2354, Oct. 1984.

15. Chien, C. F.; and Soroka, W. W.: Sound Propagation Along an Impedance Plane. *J. Sound & Vib.*, vol. 43, no. 1, 1975.

16. Pao, S. P.; Wenzel, A. R.; and Oncley, P. B.: *Prediction of Ground Effects on Aircraft Noise*. NASA TP-1104, 1978.

17. Delany, M. E.; and Bazley, E. N.: *Acoustical Characteristics of Fibrous Absorbent Materials*. NPL Aero Rep. Ac37, 1969.

Table 1. Measured and Computed Parameters for F-15 ACTIVE Flight Test

Run	PLA, deg	M_f	Alt, ft AGL	T_a, deg R	p_a, psi	p_8, psi	T_8, deg R	γ	w_8, lb/sec	A_8, sq ft	M_e	V_e, ft/sec	NPR	M_j	V_j, ft/sec	A_e/A_8	p_e/p_a	F_g, lb	V_{rel}, ft/sec	M_{rel}	β'	Run
110	31.0	0.329	1463	526.4	12.80	19.28	1040.2	1.373	119.14	2.819			1.506	0.793	1176	1.157	0.435	4054	807	0.717		110
120	35.4	0.333	1378	519.8	12.84	21.09	1062.5	1.372	133.92	2.855			1.642	0.878	1301	1.154	0.478	5082	930	0.832		120
121	38.4	0.335	1520	519.7	12.78	22.18	1081.9	1.370	142.24	2.888			1.736	0.929	1380	1.156	0.504	5748	1006	0.900		121
130	47.5	0.336	1423	520.6	12.82	25.77	1161.5	1.364	156.36	2.832	1.532	2114	2.010	1.057	1593	1.204	0.530	7316	1218	1.089	1.109	130
131	47.5	0.336	1614	520.0	12.73	25.80	1166.6	1.364	154.82	2.807	1.536	2123	2.026	1.064	1605	1.207	0.531	7300	1230	1.100	1.109	131
132	47.6	0.333	1551	520.6	12.76	25.93	1172.0	1.364	154.80	2.799	1.541	2133	2.032	1.066	1612	1.210	0.529	7325	1240	1.109	1.112	132
140	56.8	0.333	1463	519.7	12.80	28.41	1216.0	1.360	175.04	2.939	1.476	2107	2.219	1.137	1731	1.165	0.636	9057	1359	1.216	0.941	140
141	57.4	0.369	1651	519.0	12.72	29.19	1229.4	1.359	178.32	2.928	1.479	2122	2.295	1.164	1774	1.167	0.655	9478	1362	1.220	0.912	141
142	56.9	0.340	1852	518.8	12.62	28.28	1223.8	1.360	172.97	2.926	1.484	2122	2.241	1.145	1746	1.170	0.635	9028	1366	1.224	0.943	142
150	68.2	0.350	1185	526.5	12.94	32.59	1313.7	1.353	196.38	2.984	1.474	2189	2.519	1.236	1923	1.164	0.725	11403	1529	1.360	0.803	150
151	68.0	0.353	1536	526.6	12.77	32.33	1316.6	1.353	193.46	2.966	1.475	2192	2.532	1.240	1929	1.165	0.729	11278	1533	1.362	0.798	151
200	53.5	0.326	4566	518.9	11.40	24.23	1193.5	1.362	150.53	2.936	1.476	2088	2.126	1.103	1673	1.165	0.609	7500	1309	1.172	0.980	200
201	54.7	0.335	5390	514.9	11.05	24.10	1200.0	1.362	149.48	2.940	1.477	2095	2.181	1.124	1703	1.165	0.624	7597	1330	1.196	0.959	201
210	59.1	0.465	4894	517.8	11.26	27.68	1251.7	1.358	168.84	2.944	1.466	2128	2.459	1.217	1854	1.158	0.715	9446	1335	1.197	0.817	210
211	59.2	0.469	5023	517.3	11.20	27.68	1256.4	1.358	168.29	2.939	1.470	2136	2.471	1.221	1862	1.161	0.715	9457	1340	1.202	0.819	211
220	62.6	0.624	4817	517.0	11.29	31.60	1290.4	1.355	190.37	2.948	1.468	2162	2.799	1.314	1997	1.160	0.813	11565	1302	1.168	0.655	220
221	62.2	0.615	4949	516.6	11.23	31.17	1289.0	1.355	187.51	2.942	1.471	2165	2.775	1.307	1989	1.162	0.802	11335	1304	1.170	0.675	221
230	60.2	0.787	5247	514.9	11.11	33.10	1282.5	1.356	203.95	3.007	1.447	2133	2.980	1.358	2042	1.146	0.892	12717	1167	1.050	0.498	230
231	60.3	0.788	5128	515.4	11.16	33.26	1285.9	1.356	205.01	3.012	1.445	2134	2.981	1.359	2046	1.145	0.895	12805	1169	1.050	0.491	231
250	83.0	0.329	4612	516.7	11.38	36.35	1533.1	1.338	188.92	2.766	1.590	2497	3.195	1.411	2298	1.254	0.781	13192	1932	1.734	0.733	250
251	83.0	0.330	4955	515.6	11.23	36.19	1541.0	1.338	186.80	2.754	1.594	2508	3.223	1.417	2312	1.258	0.784	13124	1945	1.747	0.729	251
260	83.0	0.468	5348	515.4	11.06	39.16	1545.7	1.338	202.87	2.769	1.597	2515	3.539	1.482	2392	1.260	0.857	14808	1871	1.681	0.594	260
270	83.0	0.622	4272	520.5	11.53	44.69	1558.2	1.337	233.36	2.803	1.610	2540	3.877	1.544	2474	1.272	0.920	17651	1778	1.590	0.457	270
280	83.0	0.764	4426	518.9	11.46	47.04	1528.0	1.339	254.43	2.876	1.694	2604	4.105	1.582	2491	1.350	0.857	19344	1638	1.467	0.608	280
281	83.0	0.772	4696	517.5	11.34	46.88	1532.5	1.339	253.36	2.878	1.695	2608	4.133	1.586	2500	1.351	0.863	19334	1639	1.470	0.597	281
290	83.0	0.905	3859	521.2	11.71	50.67	1517.7	1.340	286.62	3.002	1.744	2645	4.328	1.616	2520	1.402	0.837	22038	1507	1.346	0.655	290
300	57.6	0.344	444	527.5	13.30	29.65	1248.0	1.358	182.50	2.972	1.466	2125	2.230	1.142	1759	1.159	0.648	9613	1372	1.218	0.920	300
301	57.6	0.331	472	527.6	13.28	29.60	1247.9	1.358	180.16	2.940	1.476	2135	2.228	1.141	1758	1.165	0.639	9474	1385	1.230	0.936	301
310	56.7	0.329	636	528.8	13.20	28.86	1234.2	1.359	178.66	2.974	1.462	2109	2.186	1.126	1730	1.156	0.639	9242	1359	1.205	0.933	310
400	77.8	0.335	1115	534.4	12.97	38.92	1497.5	1.341	208.41	2.817	1.571	2447	3.001	1.366	2217	1.238	0.754	14010	1838	1.622	0.775	400
401	78.5	0.379	1022	534.3	13.02	40.29	1510.1	1.340	214.82	2.818	1.576	2462	3.095	1.389	2254	1.242	0.773	14699	1824	1.610	0.744	401
402	77.8	0.347	1590	532.8	12.74	38.65	1494.6	1.341	207.66	2.824	1.574	2447	3.033	1.374	2224	1.240	0.759	14009	1831	1.618	0.768	402
410	72.5	0.508	967	534.6	13.04	38.38	1396.9	1.348	221.40	2.937	1.511	2298	2.943	1.351	2123	1.191	0.806	14294	1548	1.366	0.676	410
411	74.4	0.480	927	527.5	13.06	40.50	1427.0	1.346	228.99	2.909	1.548	2364	3.101	1.389	2191	1.219	0.804	15255	1651	1.466	0.685	411
420	67.2	0.599	1507	519.9	12.78	37.06	1324.0	1.353	221.27	2.959	1.486	2210	2.899	1.339	2053	1.173	0.821	13826	1384	1.238	0.644	420
421	69.1	0.618	1322	520.3	12.87	38.54	1333.6	1.352	231.30	2.987	1.486	2218	2.994	1.363	2088	1.172	0.849	14716	1397	1.249	0.592	421
422	69.3	0.611	1528	519.1	12.77	38.38	1333.0	1.352	229.97	2.981	1.486	2217	3.005	1.365	2090	1.172	0.852	14650	1408	1.261	0.586	422
430	60.9	0.765	1925	519.5	12.59	36.40	1280.0	1.356	225.48	3.020	1.485	2172	2.892	1.337	2016	1.171	0.819	13830	1161	1.039	0.647	430
431	62.3	0.773	1914	520.3	12.59	37.13	1297.3	1.355	228.40	3.019	1.484	2185	2.949	1.351	2046	1.171	0.837	14231	1181	1.057	0.613	431
432	62.1	0.770	1424	523.5	12.82	37.20	1291.3	1.355	229.97	3.028	1.485	2182	2.901	1.339	2028	1.171	0.822	14190	1164	1.038	0.641	432
450	78.6	0.335	1578	533.6	12.75	38.89	1507.7	1.340	207.29	2.814	1.705	2597	3.050	1.378	2239	1.361	0.627	13909	1859	1.642	1.004	450
451	76.8	0.346	1253	530.3	12.90	38.70	1475.5	1.342	209.81	2.832	1.704	2567	2.999	1.366	2200	1.359	0.617	13812	1809	1.603	1.018	451
460	72.6	0.512	1098	534.6	12.98	38.42	1400.8	1.347	220.77	2.930	1.707	2503	2.960	1.355	2131	1.361	0.604	14052	1551	1.368	1.038	460
461	72.5	0.443	1166	524.1	12.95	38.51	1402.2	1.347	220.28	2.919	1.707	2505	2.975	1.359	2137	1.361	0.607	14062	1639	1.460	1.033	461

Table 1. Concluded

Run	PLA, deg	M_f	Alt, ft AGL	T_a, deg R	p_a, psi	p_8, psi	T_8, deg R	γ	w_8, lb/sec	A_8, sq ft	M_e	V_e, ft/sec	NPR	M_j	V_j, ft/sec	A_e/A_8	p_e/p_a	F_g, lb	V_{rel}, ft/sec	M_{rel}	β'	Run
470	69.7	0.613	1364	519.3	12.85	38.89	1337.3	1.352	233.28	2.989	1.708	2446	3.026	1.370	2099	1.360	0.616	14651	1414	1.266	1.020	470
471	69.4	0.622	1290	519.8	12.89	38.89	1337.4	1.352	232.34	2.977	1.708	2445	3.018	1.368	2097	1.360	0.615	14575	1402	1.254	1.022	471
480	62.2	0.763	1316	524.2	12.87	37.43	1296.2	1.355	229.82	3.012	1.708	2407	2.907	1.341	2033	1.359	0.591	13929	1178	1.049	1.058	480
481	61.8	0.753	1178	525.9	12.94	37.18	1299.3	1.355	228.25	3.015	1.707	2409	2.874	1.333	2026	1.358	0.586	13772	1180	1.049	1.066	481
500	83.0	0.327	1377	534.3	12.85	40.40	1569.3	1.336	210.03	2.802	1.608	2547	3.145	1.401	2313	1.270	0.749	14727	1942	1.714	0.790	500
501	83.0	0.334	1409	525.8	12.83	40.72	1543.3	1.338	212.36	2.786	1.607	2524	3.174	1.407	2300	1.269	0.757	14821	1925	1.712	0.777	501
510	82.7	0.453	1131	536.0	12.96	43.90	1572.4	1.336	229.40	2.820	1.609	2550	3.387	1.452	2378	1.271	0.806	16600	1863	1.642	0.692	510
511	82.9	0.467	1237	526.9	12.91	45.17	1568.1	1.336	234.11	2.792	1.608	2546	3.498	1.474	2401	1.270	0.833	17130	1875	1.666	0.642	511
512	82.9	0.458	1475	525.8	12.80	44.64	1573.0	1.336	231.08	2.793	1.607	2549	3.488	1.473	2402	1.270	0.832	16918	1888	1.680	0.644	512
520	78.1	0.616	1337	526.2	12.86	45.54	1478.0	1.342	249.40	2.863	1.608	2471	3.540	1.481	2338	1.269	0.841	17778	1645	1.463	0.627	520
530	75.1	0.766	1450	526.5	12.81	45.33	1430.2	1.346	258.24	2.932	1.610	2431	3.538	1.480	2298	1.269	0.838	18093	1437	1.278	0.632	530
550	83.0	0.335	1222	535.2	12.92	40.60	1570.9	1.336	211.55	2.811	1.706	2654	3.142	1.400	2313	1.363	0.645	14698	1933	1.704	0.975	550
552	83.0	0.346	1424	526.8	12.82	41.27	1553.4	1.337	214.44	2.786	1.708	2640	3.218	1.417	2320	1.365	0.659	14969	1931	1.717	0.954	552
560	83.0	0.459	1278	536.3	12.89	43.69	1569.1	1.336	228.71	2.822	1.725	2671	3.389	1.453	2376	1.383	0.676	16383	1855	1.634	0.930	560
561	82.9	0.455	1508	525.8	12.78	44.46	1568.5	1.336	230.42	2.792	1.730	2676	3.478	1.470	2396	1.388	0.689	16673	1884	1.676	0.911	561
570	77.7	0.611	1056	526.7	13.00	44.63	1456.8	1.344	249.26	2.901	1.732	2579	3.433	1.460	2297	1.388	0.675	17263	1609	1.430	0.933	570
580	74.3	0.767	1348	527.0	12.86	45.02	1427.7	1.346	256.73	2.932	1.747	2567	3.501	1.473	2288	1.403	0.673	17715	1425	1.266	0.940	580
600	83.0	0.331	5414	513.9	11.04	35.84	1545.9	1.338	184.44	2.750	1.607	2526	3.248	1.423	2322	1.269	0.775	13010	1954	1.758	0.747	600
610	80.5	0.468	5241	516.5	11.11	38.25	1504.8	1.340	202.07	2.785	1.608	2493	3.443	1.463	2338	1.269	0.819	14387	1817	1.631	0.668	610
611	80.9	0.467	5143	518.1	11.15	38.55	1533.2	1.339	202.25	2.793	1.608	2517	3.458	1.466	2364	1.269	0.823	14564	1842	1.651	0.660	611
620	75.8	0.622	4794	515.0	11.30	39.07	1421.7	1.346	223.58	2.937	1.608	2422	3.458	1.465	2274	1.268	0.821	15484	1582	1.422	0.664	620
621	76.3	0.624	4924	515.2	11.24	39.16	1427.5	1.346	223.24	2.932	1.609	2428	3.483	1.470	2284	1.269	0.825	15534	1590	1.429	0.655	621
630	71.1	0.783	3838	522.9	11.72	38.94	1375.4	1.349	230.71	2.993	1.604	2378	3.324	1.437	2205	1.264	0.792	15467	1327	1.184	0.714	630
631	71.8	0.783	4693	517.0	11.34	38.62	1374.6	1.349	229.64	3.003	1.602	2375	3.405	1.453	2223	1.262	0.814	15541	1351	1.212	0.674	631
632	83.0	0.805	4663	519.2	11.36	46.96	1524.4	1.340	259.43	2.936	1.609	2511	4.135	1.586	2493	1.270	0.982	19805	1594	1.427	0.269	632
650	83.0	0.330	5121	515.5	11.16	35.98	1540.5	1.338	185.98	2.758	1.707	2628	3.224	1.418	2312	1.363	0.661	12939	1944	1.747	0.950	650
660	80.9	0.466	5171	517.1	11.14	38.47	1519.9	1.339	202.50	2.789	1.728	2631	3.454	1.465	2352	1.385	0.685	14377	1833	1.644	0.917	660
670	76.6	0.626	4943	515.4	11.24	39.83	1444.9	1.344	223.38	2.901	1.743	2579	3.545	1.482	2312	1.399	0.686	15593	1616	1.452	0.918	670
671	76.2	0.622	5111	514.8	11.16	39.17	1432.8	1.345	221.55	2.913	1.741	2566	3.509	1.475	2294	1.397	0.681	15338	1602	1.441	0.926	671
680	71.9	0.779	4547	518.3	11.41	38.95	1381.3	1.349	229.99	2.989	1.745	2522	3.415	1.455	2231	1.400	0.657	15444	1361	1.220	0.963	680
700	39.3	0.366	5766	515.8	10.89	19.57	1091.0	1.370	124.83	2.876			1.798	0.961	1425	1.162	0.515	5221	1018	0.914		700
701	38.6	0.334	5137	515.7	11.15	19.46	1080.9	1.370	124.48	2.879			1.745	0.934	1385	1.161	0.500	5043	1014	0.910		701
710	38.5	0.342	5445	515.0	11.02	19.32	1081.5	1.370	123.72	2.881			1.753	0.938	1390	1.162	0.502	5035	1011	0.908		710
720	38.5	0.336	5341	515.0	11.07	19.35	1081.2	1.370	123.70	2.877			1.748	0.936	1387	1.161	0.501	5022	1014	0.912		720
730	38.5	0.334	5029	516.3	11.20	19.64	1086.9	1.370	124.45	2.858			1.754	0.939	1395	1.162	0.503	5081	1023	0.919		730
740	73.1	0.820	6123	515.4	10.74	39.15	1409.1	1.347	226.04	2.950	1.761	2563	3.646	1.500	2304	1.418	0.685	15726	1391	1.250	0.923	740
741	72.9	0.802	4987	517.4	11.22	40.15	1406.6	1.347	232.13	2.952	1.755	2555	3.579	1.488	2288	1.411	0.679	16026	1393	1.249	0.931	741
750	73.6	0.790	4803	517.7	11.30	40.13	1405.1	1.347	233.16	2.965	1.753	2551	3.553	1.483	2281	1.409	0.676	16043	1399	1.255	0.935	750
760	73.1	0.798	5291	517.9	11.09	39.67	1411.6	1.347	229.33	2.957	1.754	2558	3.578	1.488	2292	1.410	0.680	15862	1401	1.256	0.929	760
770	73.9	0.809	5999	516.7	10.79	39.28	1417.2	1.347	226.57	2.956	1.761	2570	3.640	1.500	2309	1.417	0.685	15801	1407	1.263	0.923	770
800	83.0	0.885	3845	517.9	11.71	50.87	1515.3	1.340	284.35	2.962	1.600	2494	4.343	1.619	2520	1.263	1.045	21956	1533	1.374	0.242	800
801	83.0	0.890	4839	513.2	11.28	50.02	1520.5	1.340	278.09	2.951	1.610	2508	4.434	1.632	2539	1.271	1.052	21637	1551	1.397	0.270	801
802	83.0	0.895	3976	516.4	11.65	51.06	1510.4	1.341	285.47	2.958	1.598	2487	4.381	1.624	2522	1.261	1.058	22060	1525	1.369	0.292	802
810	83.0	0.890	4322	515.1	11.50	50.48	1506.5	1.341	281.76	2.948	1.574	2458	4.388	1.617	2511	1.241	1.098	21753	1521	1.367	0.369	810
820	83.0	0.889	4432	516.4	11.46	50.27	1510.1	1.341	280.48	2.951	1.837	2728	4.388	1.626	2523	1.509	0.735	21485	1533	1.376	0.855	820

Table 2. Nominal (Nom) and Actual (Act) Conditions for the 400 Through 600 Series of Runs

[Actual conditions represent averages over number of runs for each run type]

Run series	No. of runs	M_f		M_e		M_j		β'		M_{rel}
		Nom	Act	Nom	Act	Nom	Act	Nom	Act	Act
400	3	0.34	0.35	1.51	1.57	1.36	1.38	0.67	0.76	1.64
410	2	0.47	0.49	1.51	1.53	1.36	1.37	0.67	0.69	1.44
420	3	0.61	0.61	1.51	1.49	1.36	1.36	0.67	0.61	1.25
430	3	0.76	0.77	1.51	1.49	1.36	1.32	0.67	0.63	1.05
450	2	0.34	0.34	1.71	1.71	1.36	1.37	1.04	1.01	1.65
460	2	0.47	0.48	1.71	1.71	1.36	1.36	1.04	1.04	1.43
470	2	0.61	0.62	1.71	1.71	1.36	1.37	1.04	1.02	1.26
480	2	0.76	0.76	1.71	1.71	1.36	1.34	1.04	1.07	1.06
500	2	0.34	0.33	1.61	1.61	1.46	1.40	0.67	0.79	1.73
510	3	0.47	0.46	1.61	1.61	1.46	1.47	0.67	0.66	1.68
520	1	0.61	0.62	1.61	1.61	1.46	1.48	0.67	0.63	1.47
530	1	0.76	0.77	1.61	1.61	1.46	1.48	0.67	0.63	1.29
550	2	0.34	0.34	1.71	1.71	1.46	1.41	0.89	0.96	1.73
560	2	0.47	0.46	1.71	1.73	1.46	1.46	0.89	0.93	1.67
570	1	0.61	0.61	1.71	1.73	1.46	1.46	0.89	0.93	1.44
580	1	0.76	0.77	1.71	1.75	1.46	1.47	0.89	0.94	1.28
600	1	0.34	0.33	1.61	1.61	1.46	1.42	0.67	0.75	1.76
610	2	0.47	0.47	1.61	1.61	1.46	1.46	0.67	0.66	1.64
620	2	0.61	0.62	1.61	1.61	1.46	1.47	0.67	0.66	1.43
630	2	0.76	0.78	1.61	1.61	1.46	1.45	0.67	0.69	1.20
650	1	0.34	0.33	1.71	1.71	1.46	1.42	0.89	0.95	1.75
660	1	0.47	0.47	1.71	1.73	1.46	1.47	0.89	0.92	1.64
670	2	0.61	0.62	1.71	1.74	1.46	1.48	0.89	0.92	1.45
680	1	0.76	0.78	1.71	1.75	1.46	1.48	0.89	0.96	1.22

Figure 1. F-15 ACTIVE Aircraft in flight.

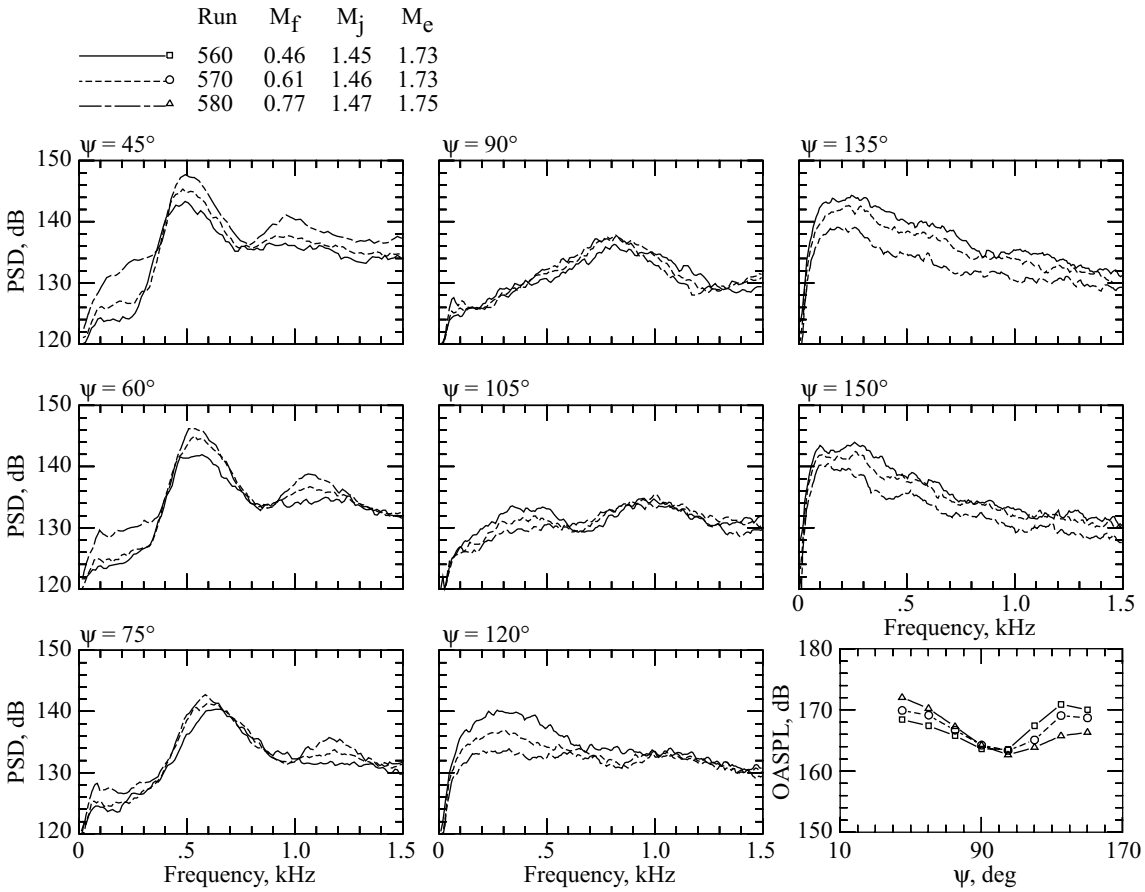

Figure 2. Power spectral densities of jet source noise at varying flight speed showing opposite effects in upstream and downstream directions.

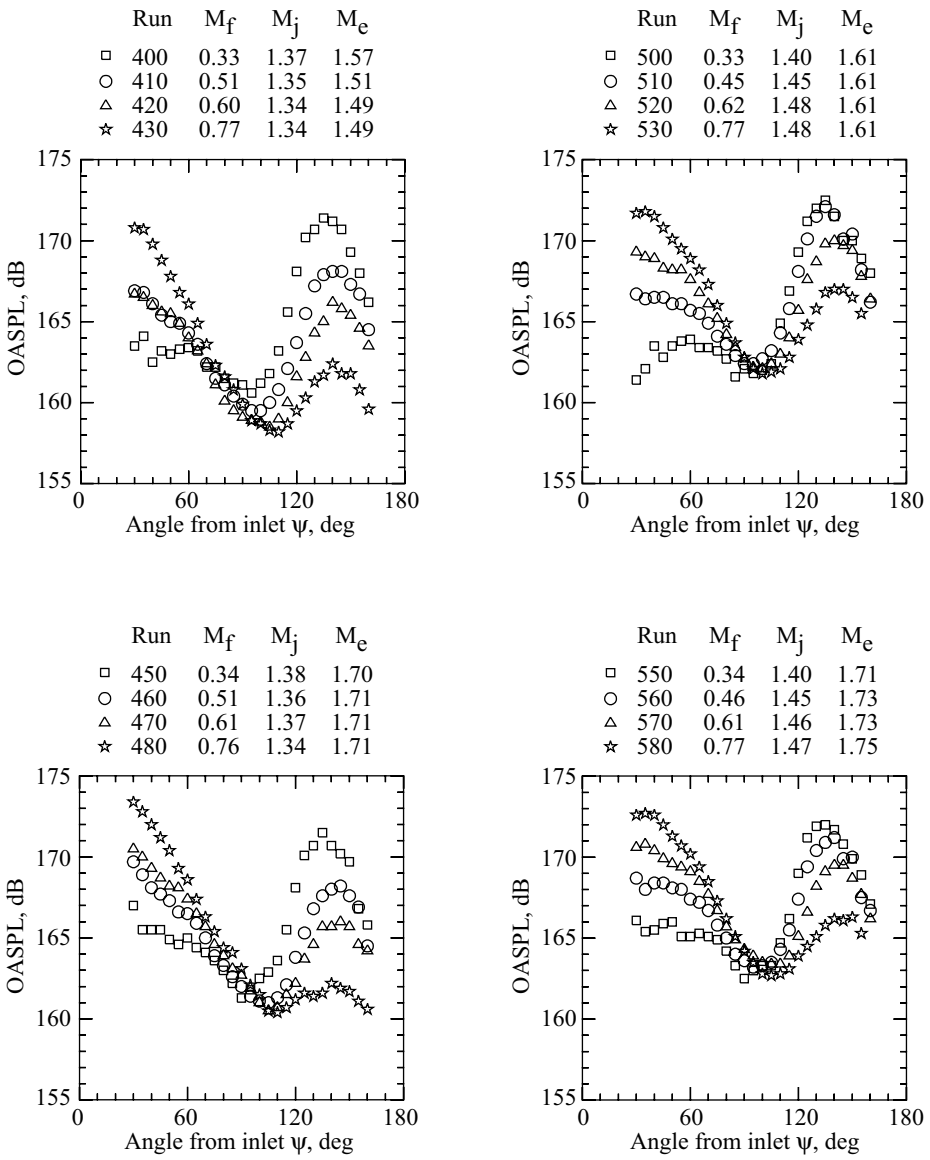

Figure 3. Effect of flight speed on directivity of supersonic jet noise for each of four low altitude series.

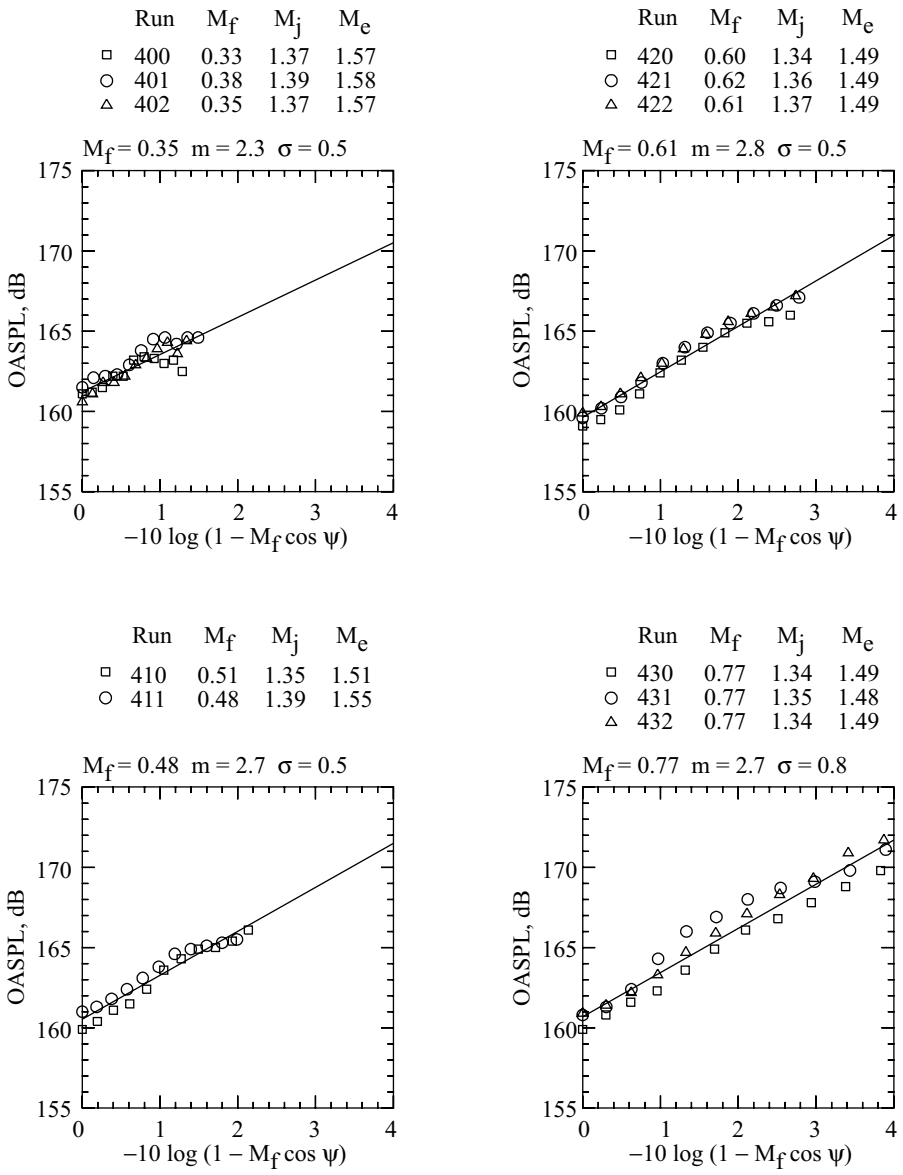

Figure 4. Determination of broadband shock noise Doppler factor exponent m for $\psi = 40°$ to $90°$ at four flight Mach numbers with nominal jet conditions $M_j = 1.36$ and $M_e = 1.51$.

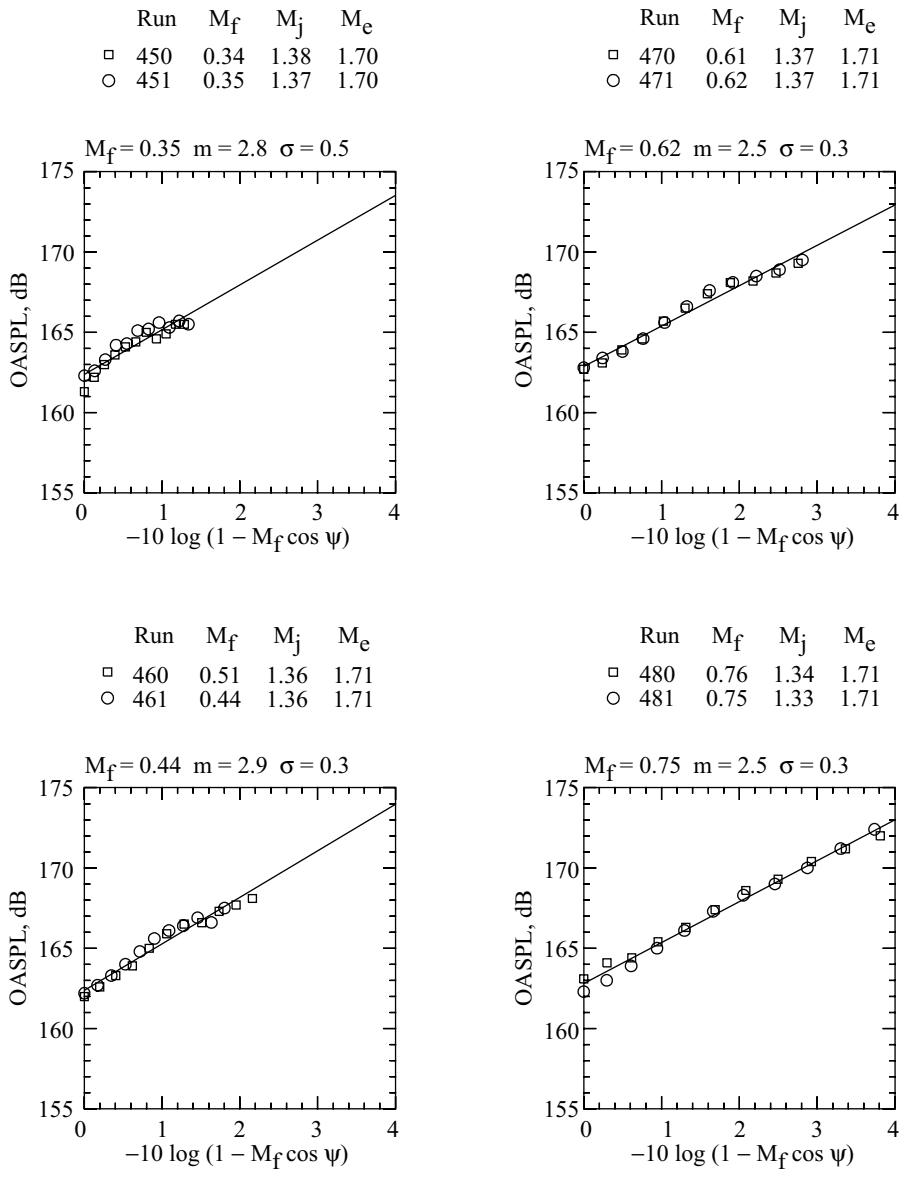

Figure 5. Determination of broadband shock noise Doppler factor exponent m for $\psi = 40°$ to $90°$ at four flight Mach numbers with nominal jet conditions $M_j = 1.36$ and $M_e = 1.71$.

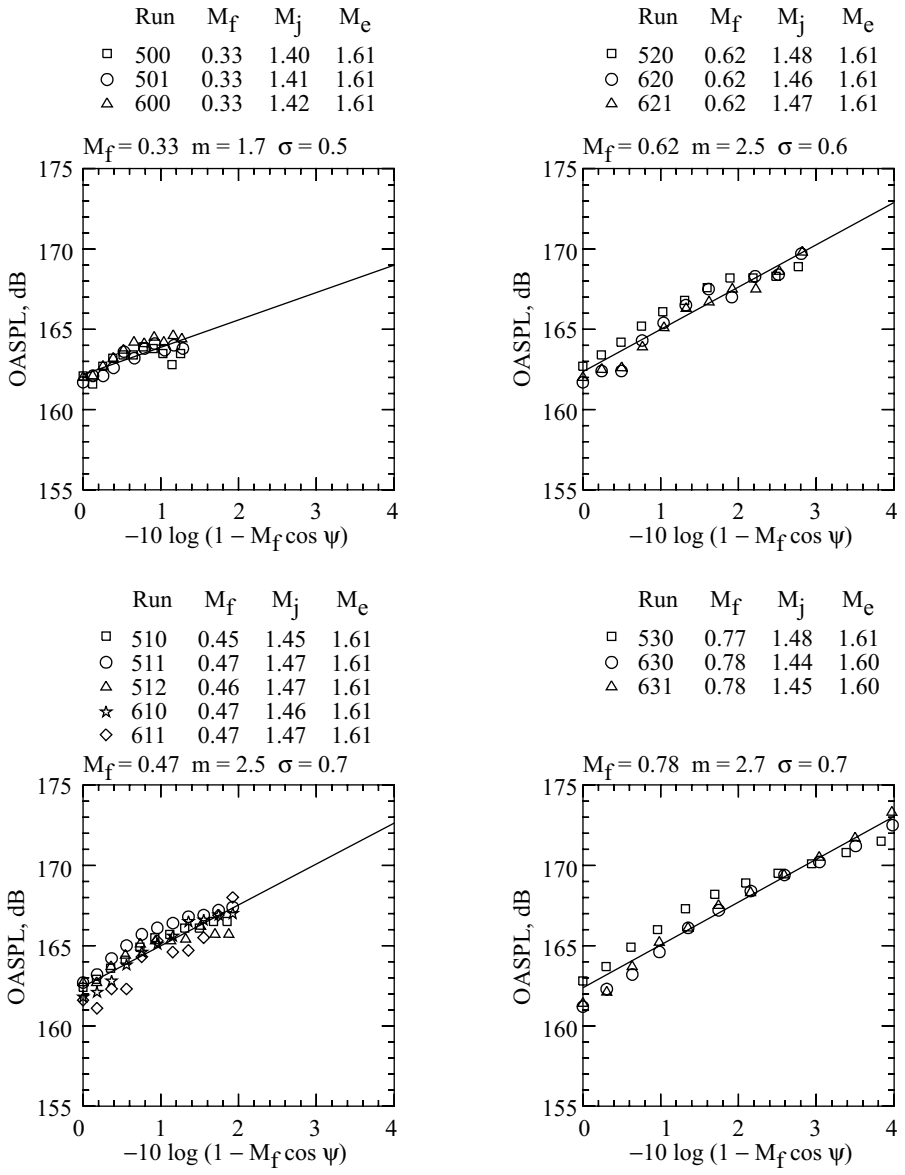

Figure 6. Determination of broadband shock noise Doppler factor exponent m for ψ = 40° to 90° at four flight Mach numbers with nominal jet conditions M_j = 1.46 and M_e = 1.61.

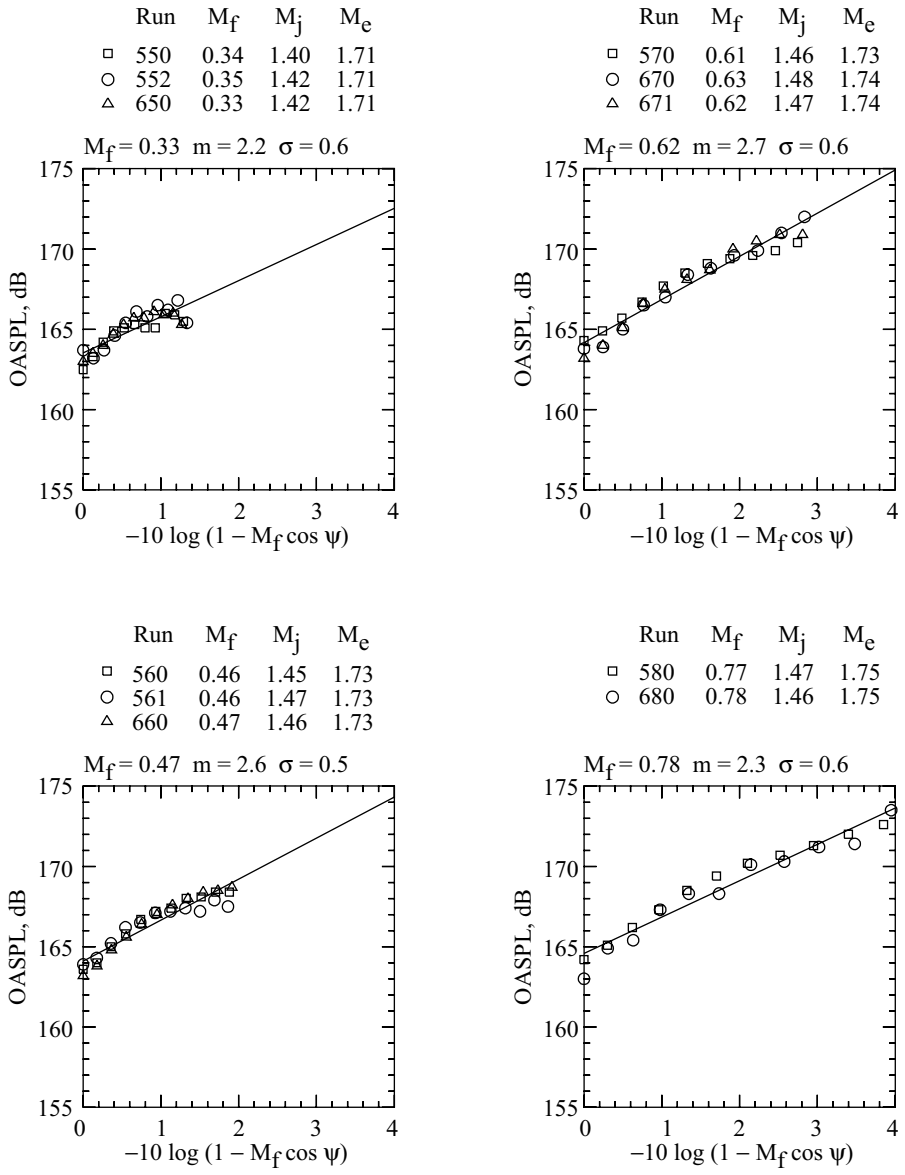

Figure 7. Determination of broadband shock noise Doppler factor exponent m for $\psi = 40°$ to $90°$ at four flight Mach numbers with nominal jet conditions $M_j = 1.46$ and $M_e = 1.71$.

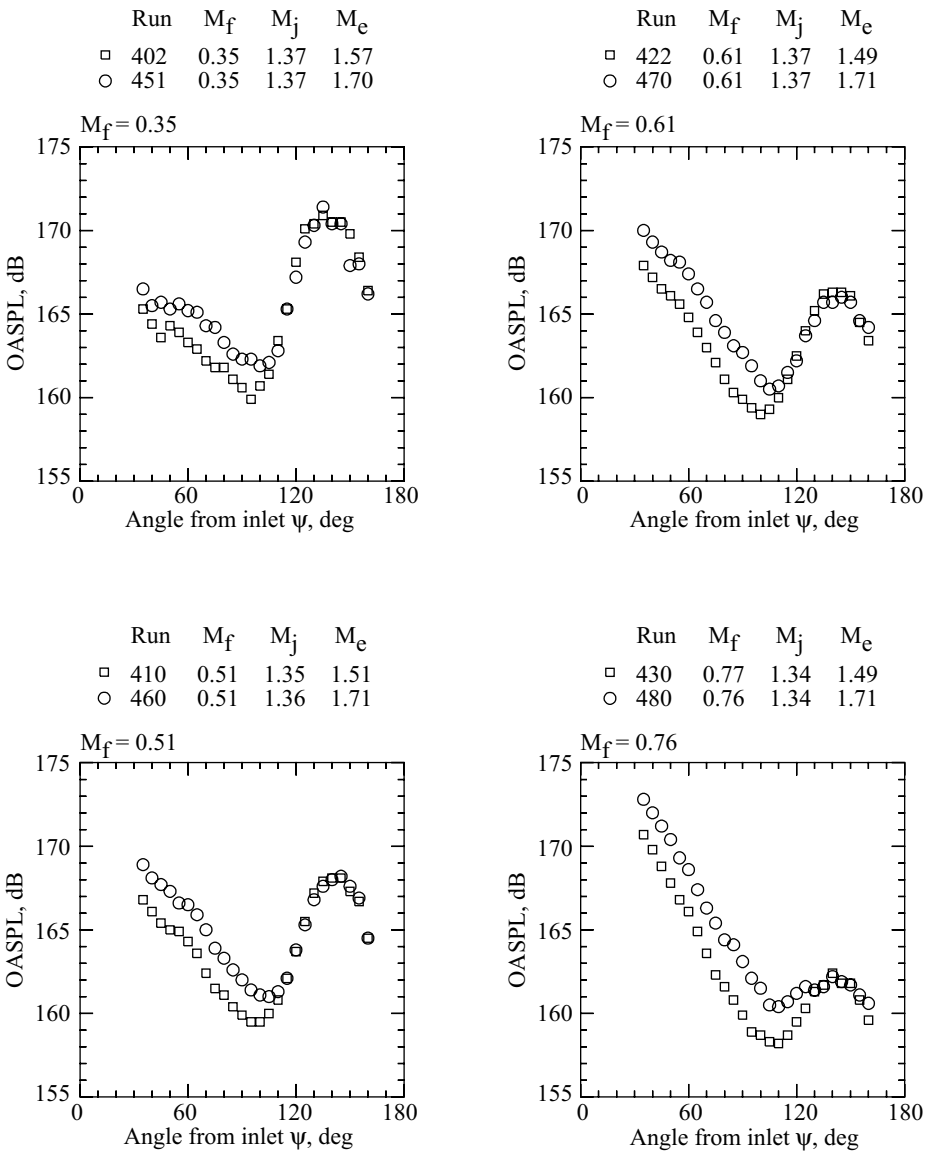

Figure 8. Effect on jet noise directivity of varying nozzle exit Mach number at constant nozzle fully expanded Mach number at four flight Mach numbers for 400 series.

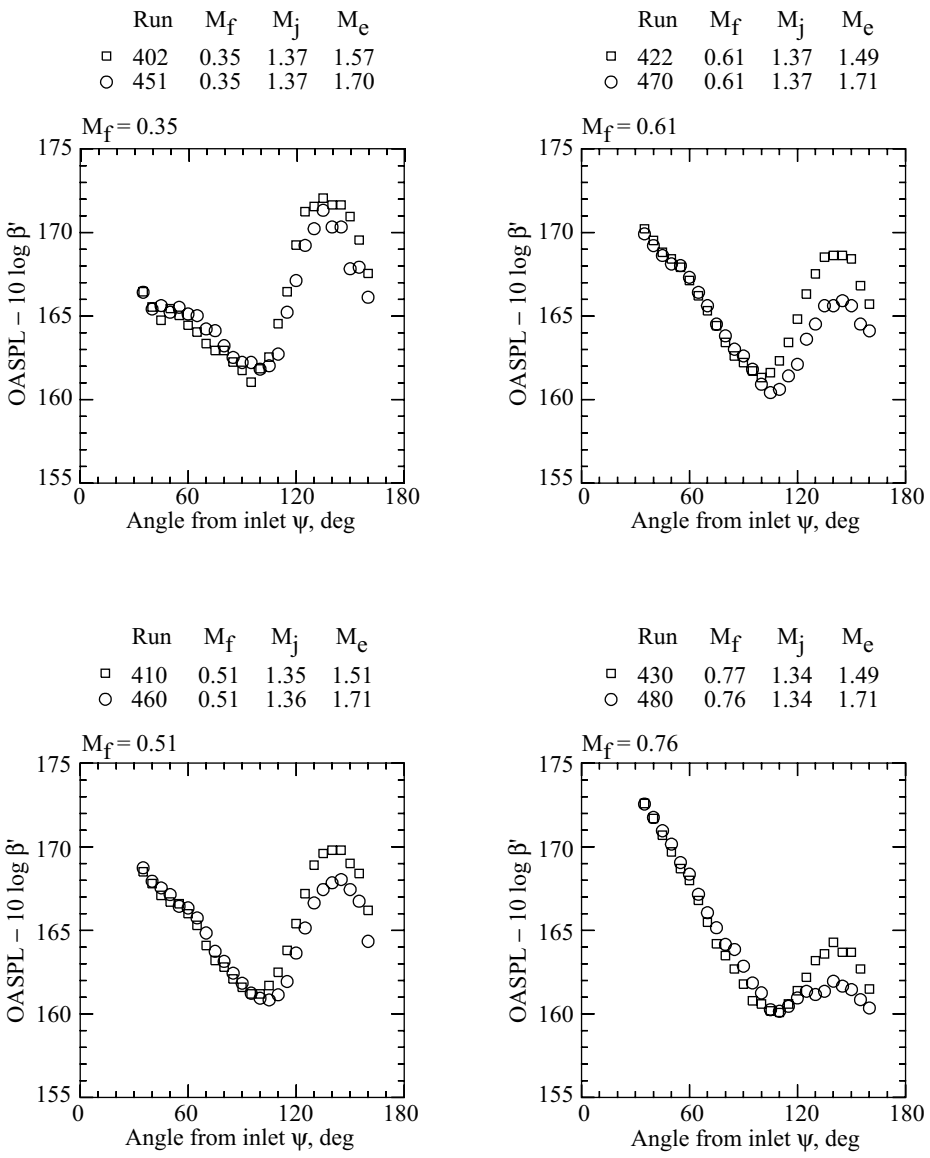

Figure 9. Collapse of broadband shock noise levels of figure 8 by first power of β'.

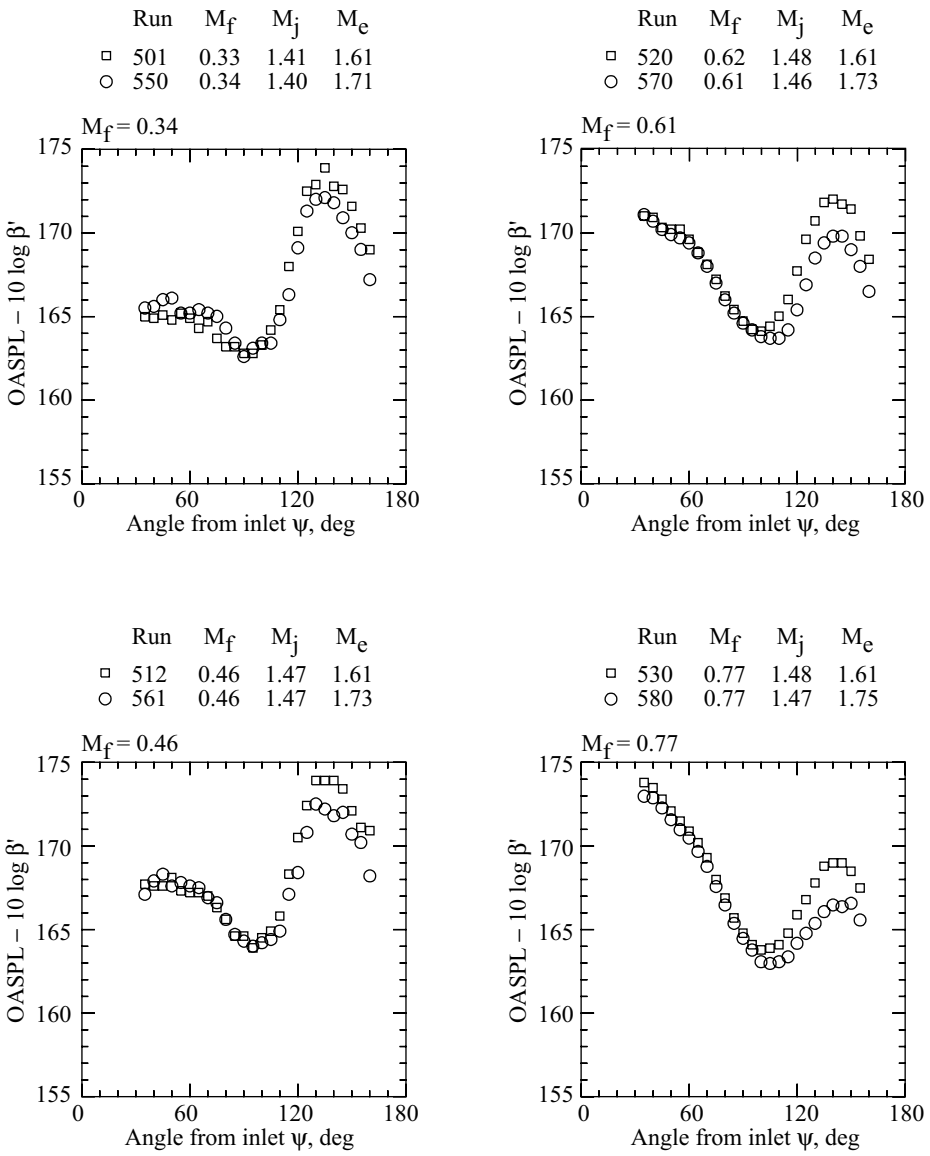

Figure 10. Collapse of broadband shock noise levels by first power of β' for 500 series.

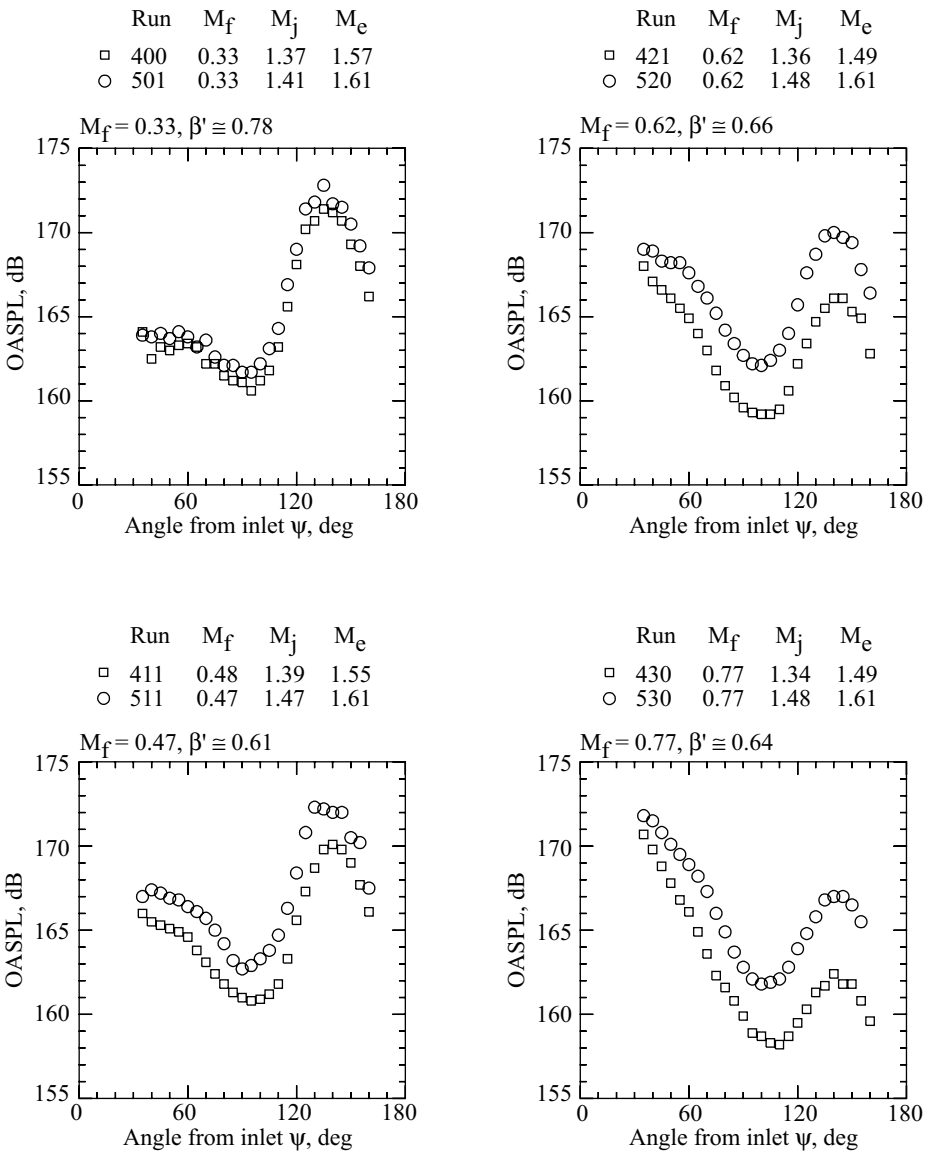

Figure 11. Effect of increased fully expanded Mach number on OASPL. For each plot, M_j and M_e are varied while keeping M_f and β' constant.

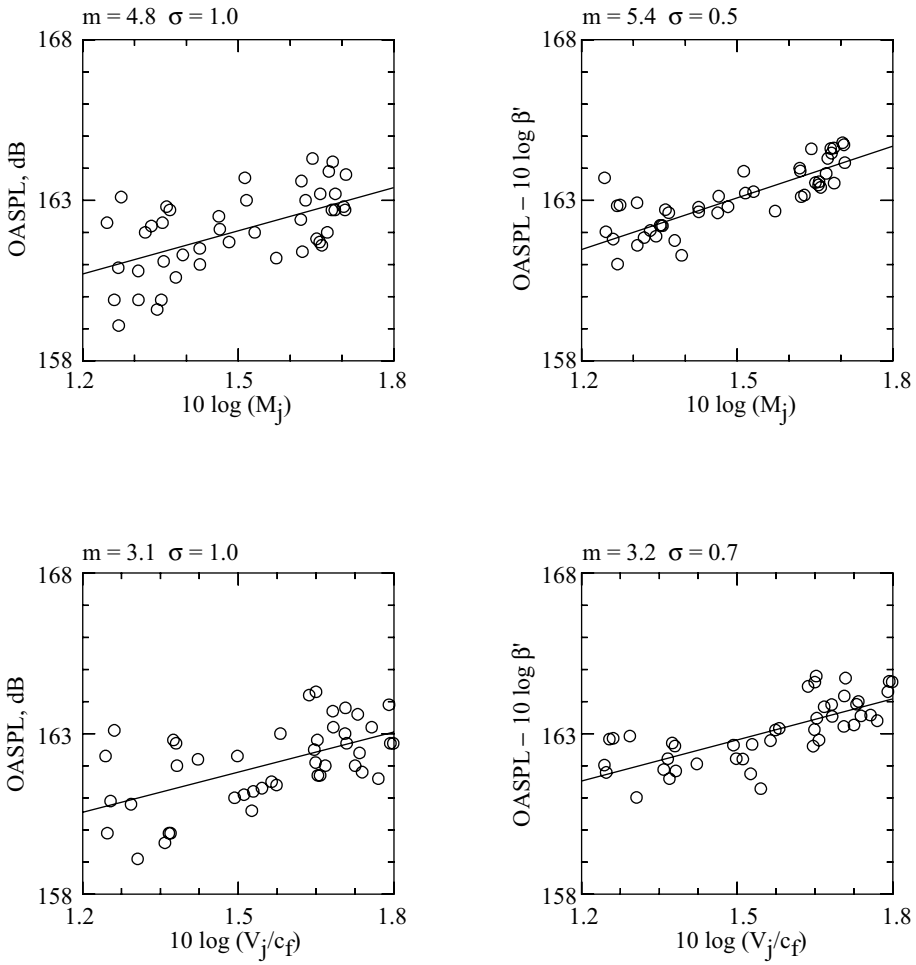

Figure 12. Determination of appropriate jet velocity parameter and its exponent for normalization of broadband shock noise OASPL (400/500/600 series at $\psi = 90°$).

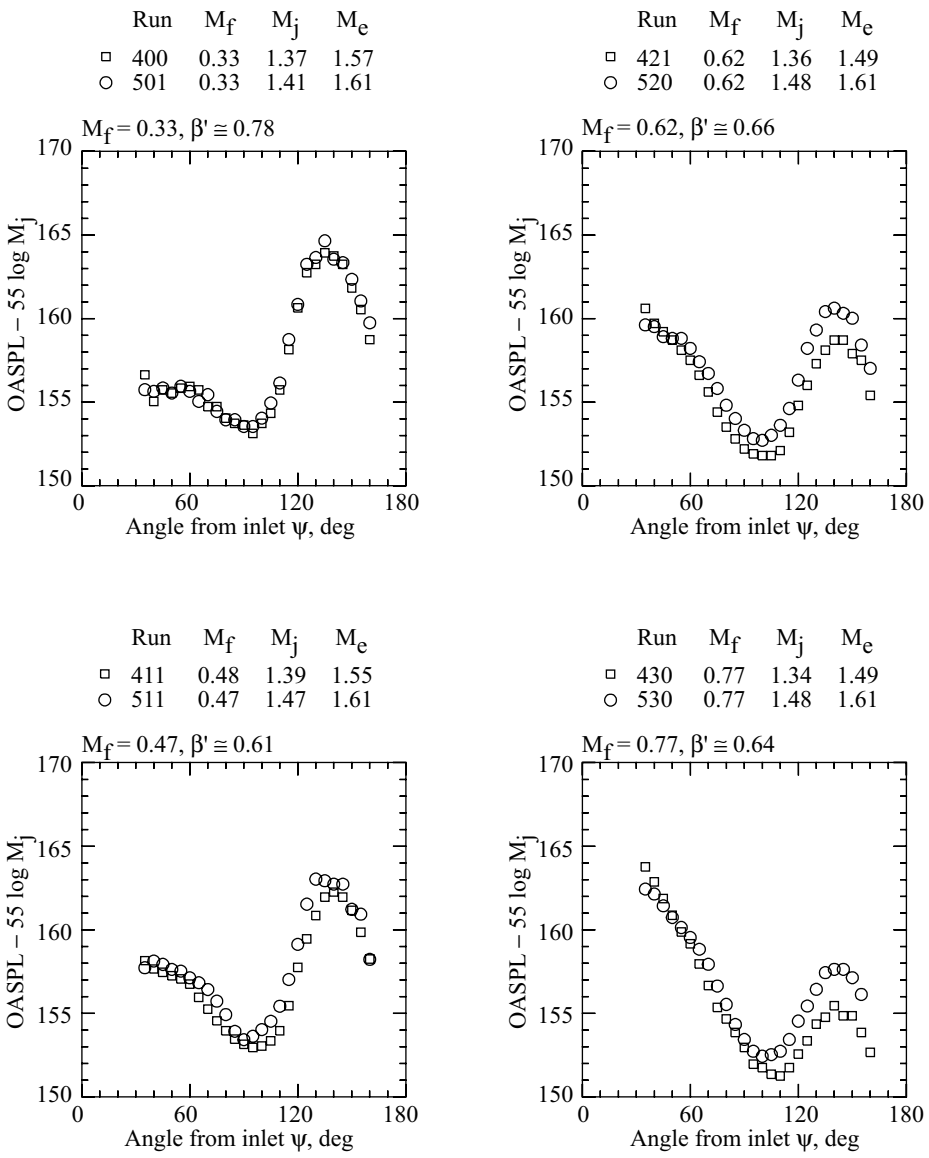

Figure 13. Collapse of upstream broadband shock noise at constant β' by 5.5 power of M_j.

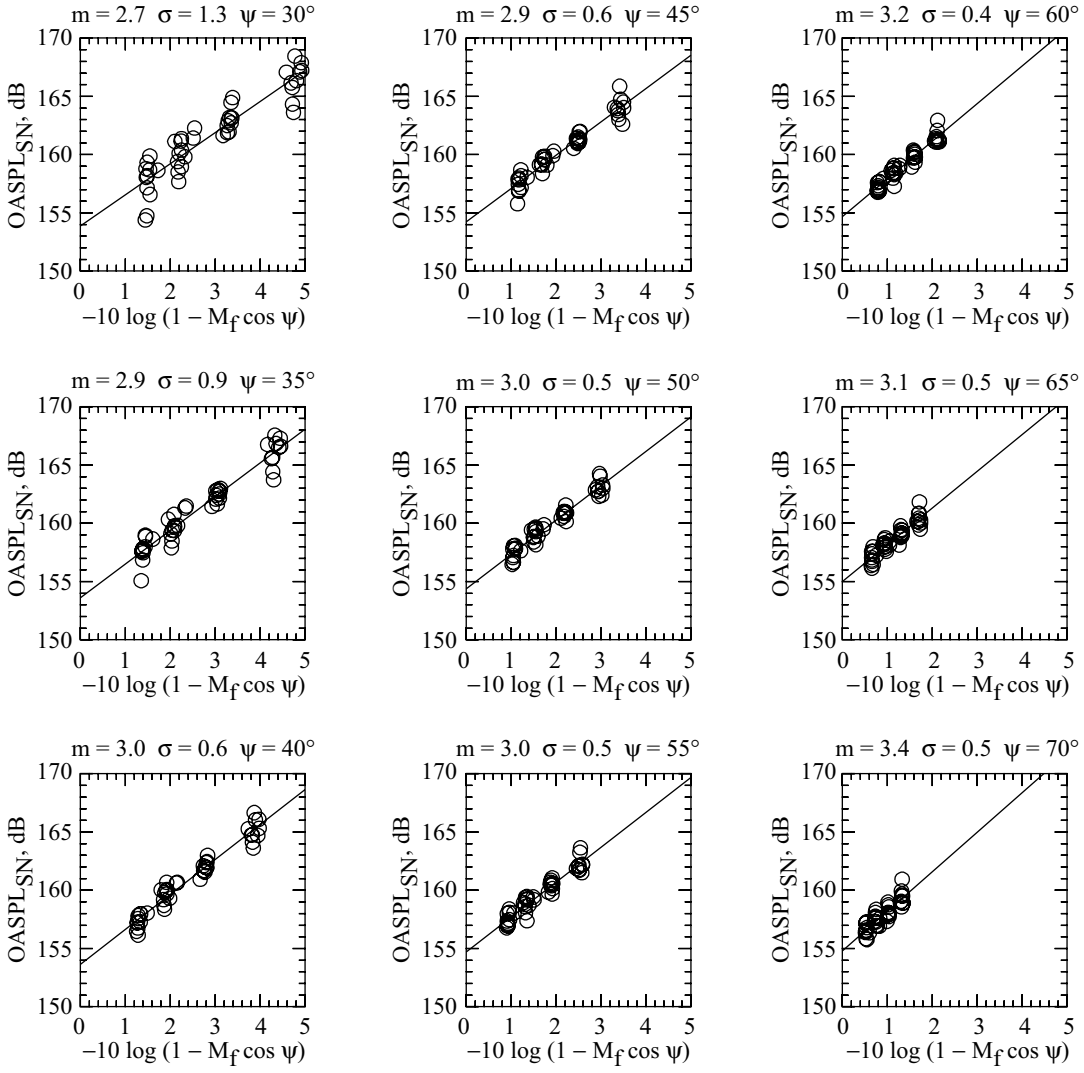

Figure 14. Correlation of normalized broadband shock noise with Doppler factor variations due to changes in flight Mach number at emission angles from 30° to 70° (400/500/600 series data).

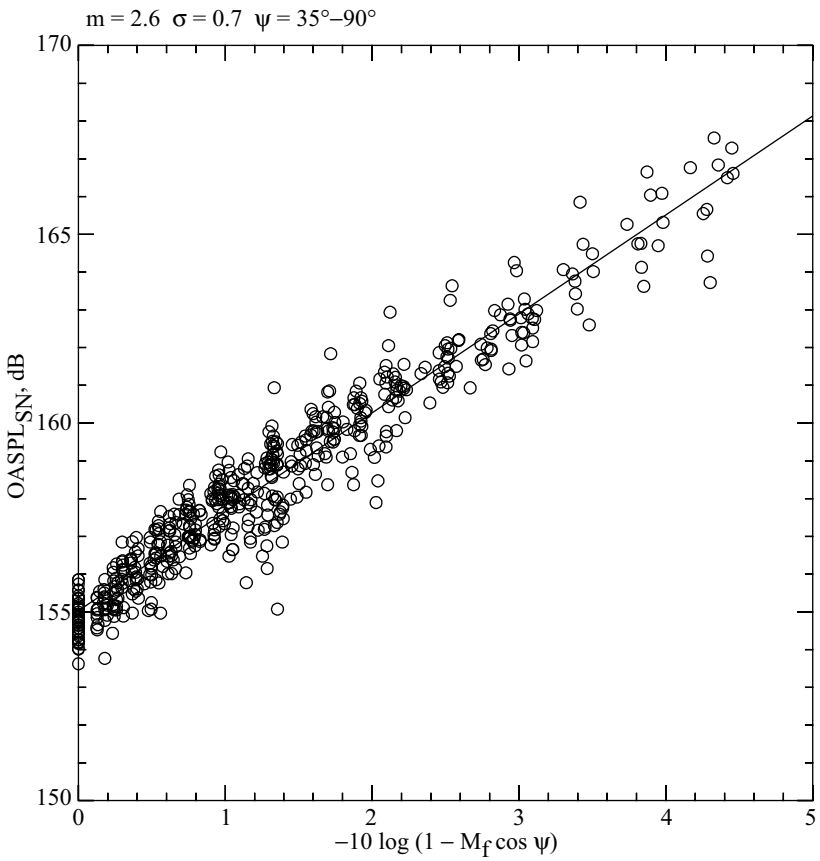

Figure 15. Correlation of normalized OASPL of broadband shock noise with Doppler factor at all angles between 35° and 90° for the 400/500/600 series, yielding Doppler factor exponent $m = 2.6$.

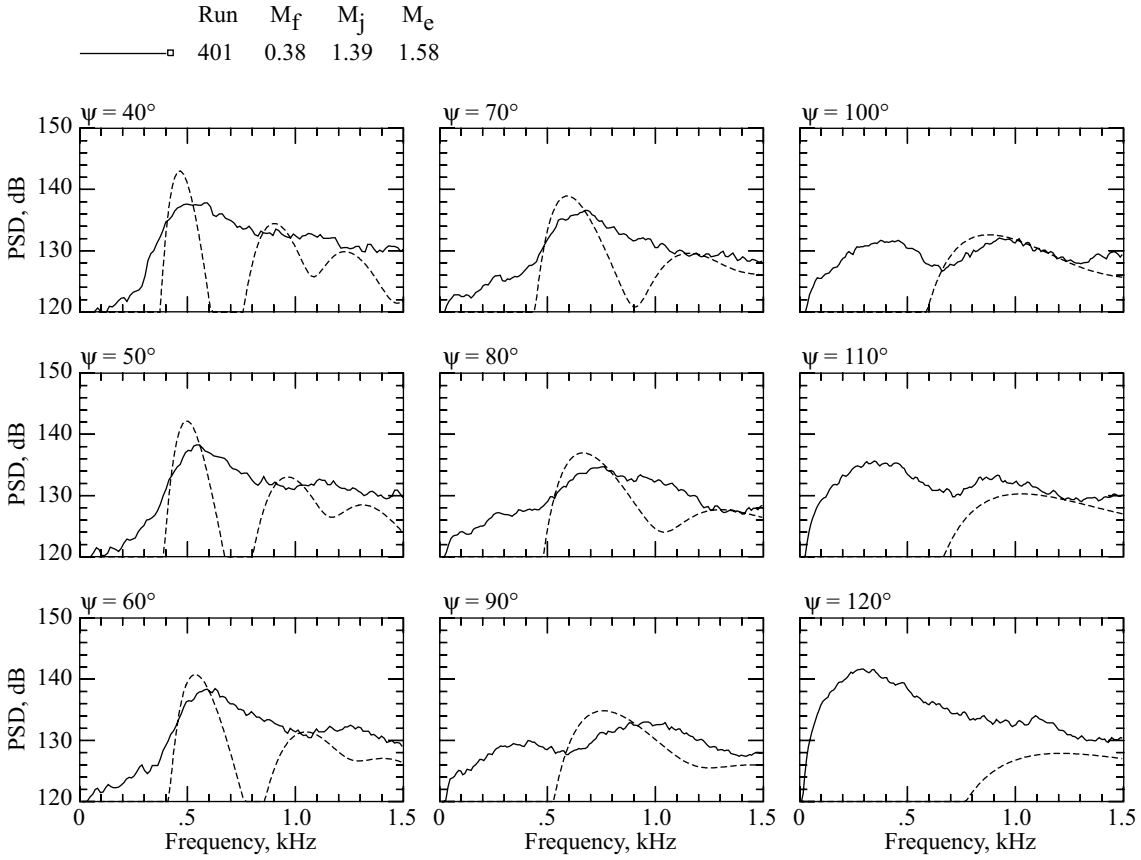

Figure 16. Comparison of measured (solid line) power spectral densities from highly overexpanded F-15 exhaust jet with Tam's predicted (dashed line) broadband shock noise at flight Mach number of 0.38.

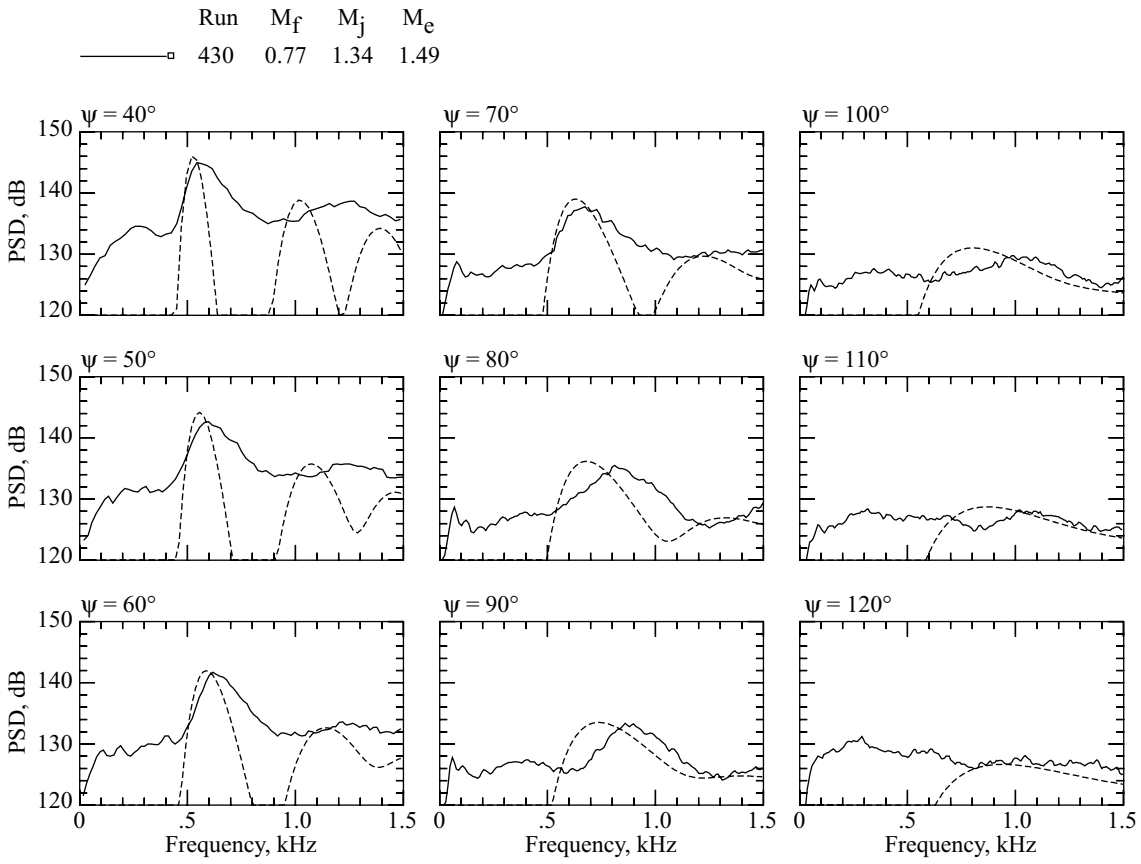

Figure 17. Comparison of measured spectra from highly overexpanded F-15 exhaust jet with Tam's predicted broadband shock noise spectra at flight Mach number of 0.77.

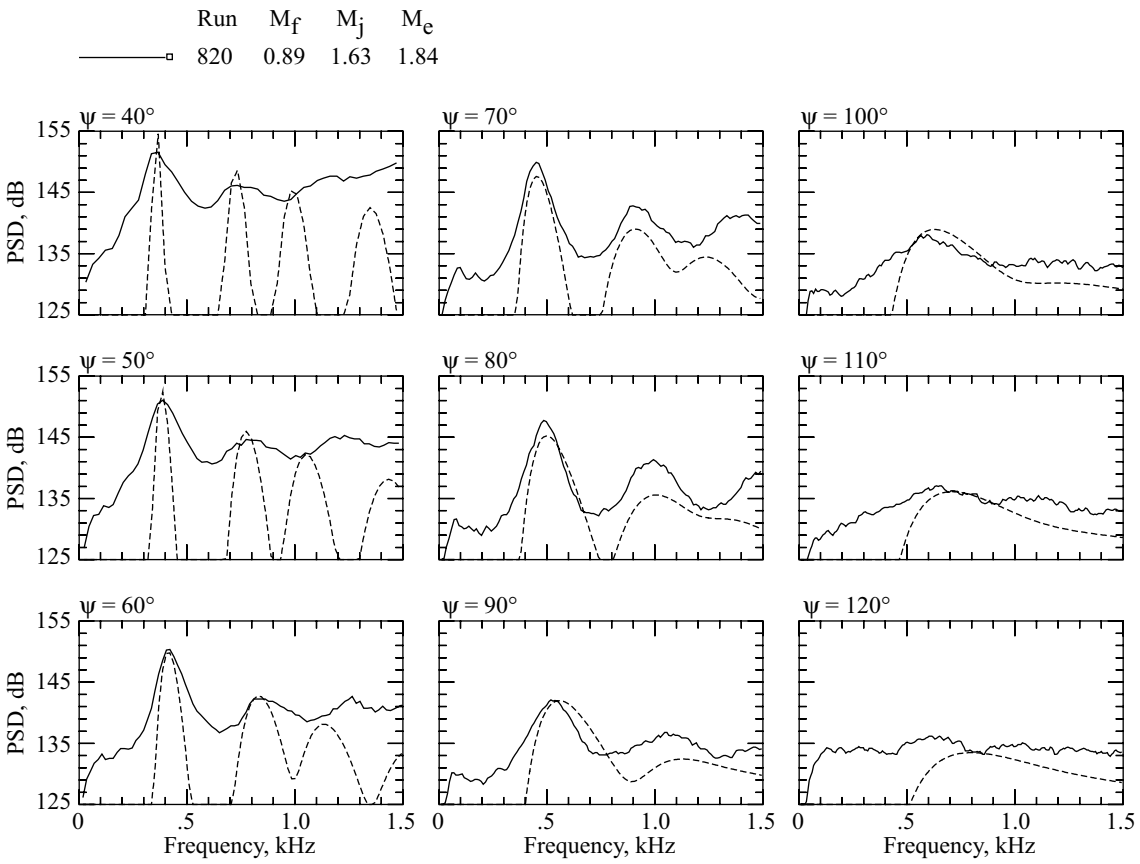

Figure 18. Comparison of measured spectra from highly overexpanded F-15 exhaust jet ($\beta' = 0.86$), with Tam's predicted broadband shock noise spectra at flight Mach number of 0.89.

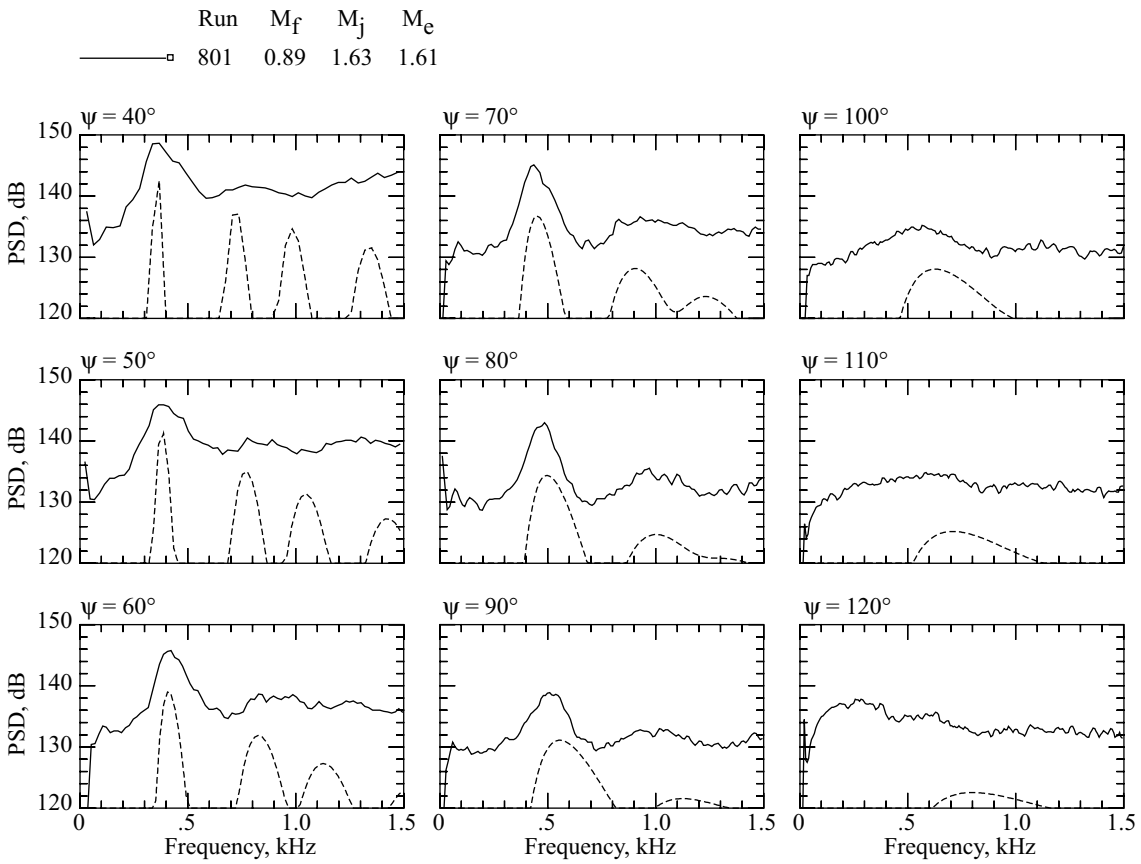

Figure 19. Comparison of measured spectra from slightly underexpanded F-15 exhaust jet ($\beta' = 0.27$), with Tam's predicted broadband shock noise spectra at flight Mach number of 0.89.

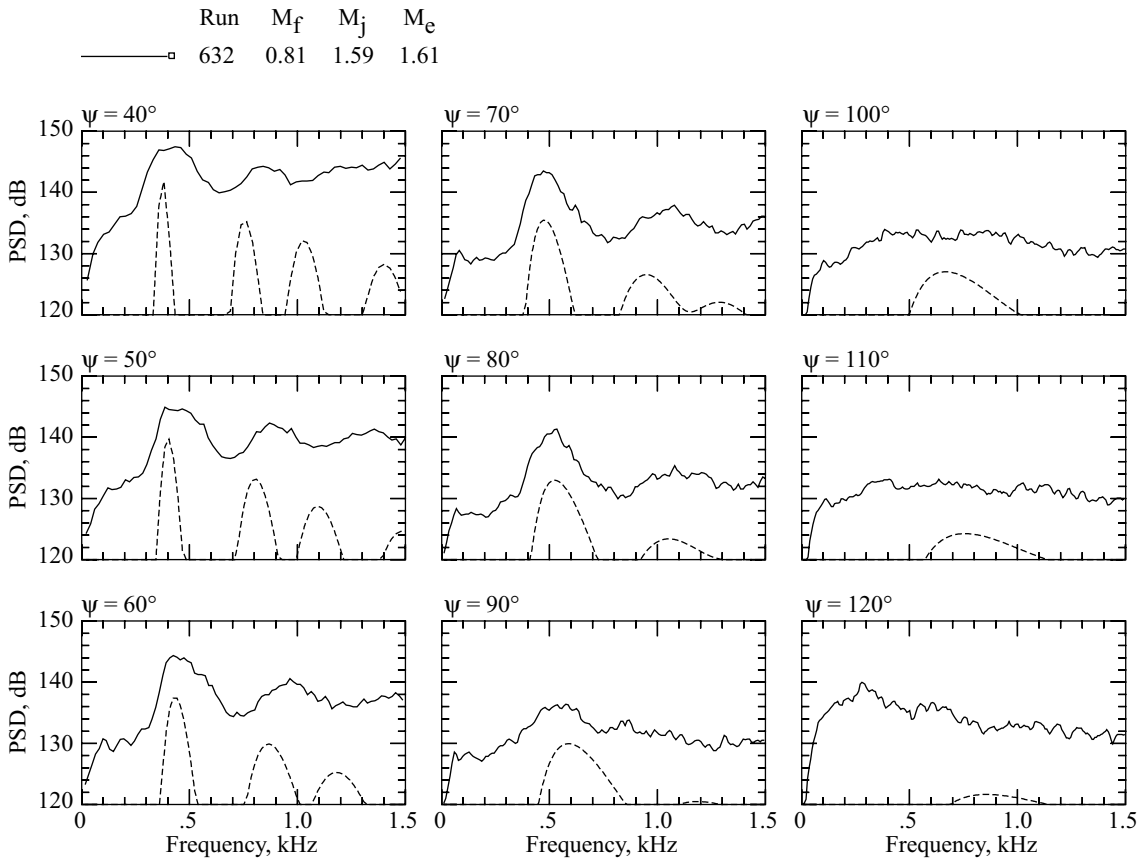

Figure 20. Comparison of Tam's predicted broadband shock noise spectra with measured spectra from slightly overexpanded F-15 exhaust jet for mildly accelerated flight at overhead flight Mach number of 0.81.

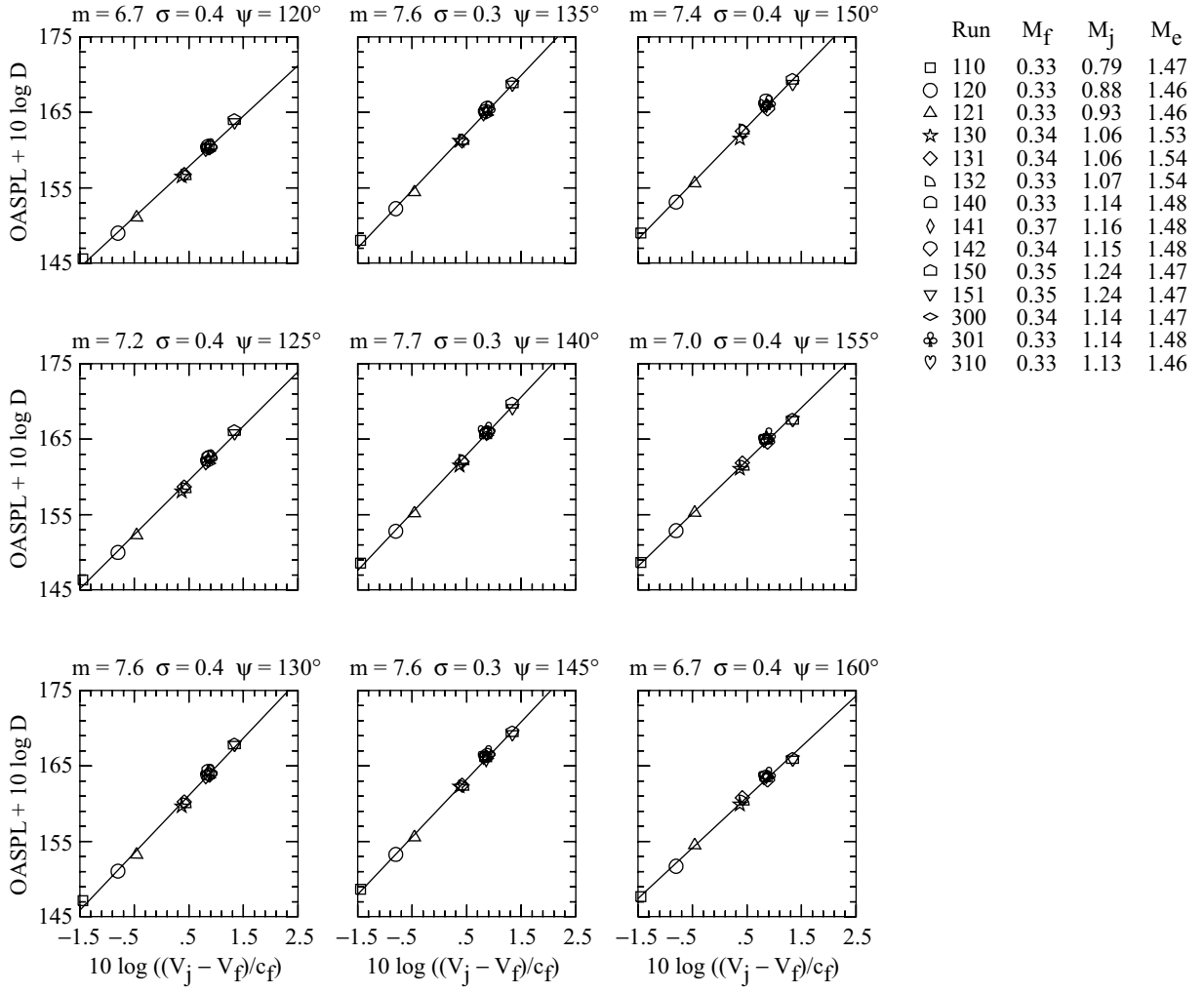

Figure 21. Correlation of jet mixing noise (normalized by Doppler factor) at lowest nominal flight Mach number for lower jet relative velocities.

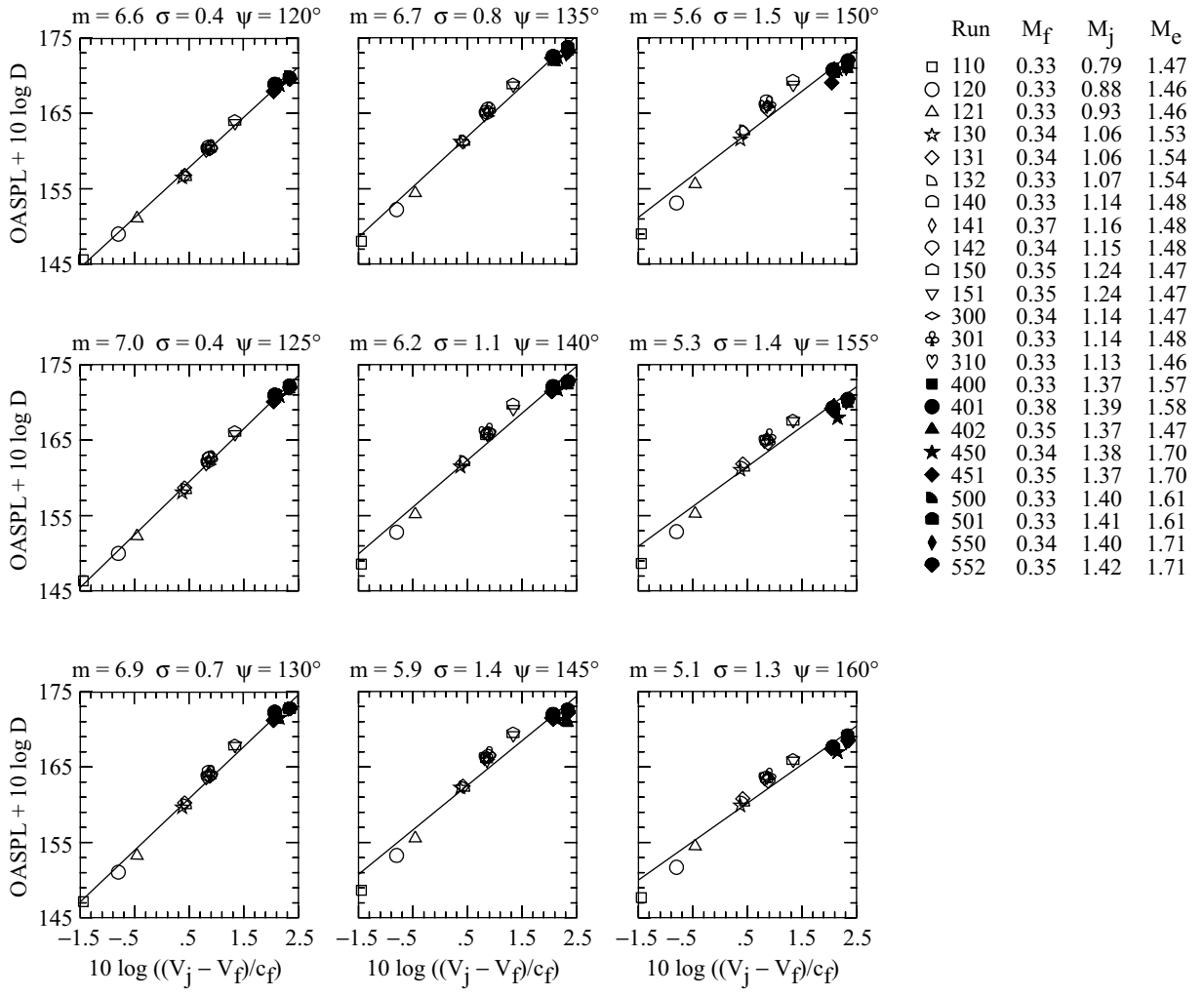

Figure 22. Attempted correlation of jet mixing noise (normalized by Doppler factor) at lowest nominal flight Mach number for all jet relative velocities.

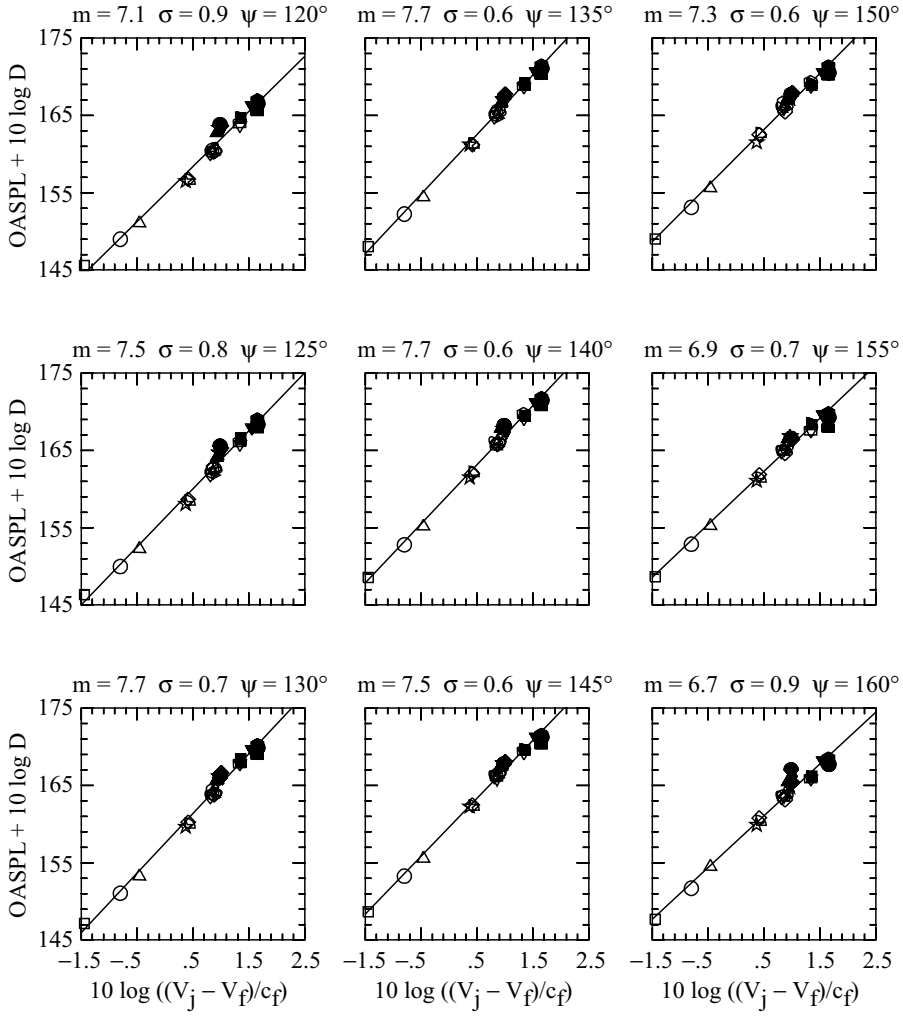

Figure 23. Correlation of jet mixing noise (normalized by Doppler factor) at flight Mach numbers below 0.7 and jet relative Mach numbers below 1.5.

Appendix A

Ray Tracing

The choice of propagation model was driven by the characteristics of the atmosphere and aircraft as well as the desire to make temporal comparisons between measured and predicted ground noise levels. Ray acoustics explicitly account for convection of sound by winds, nonisotropic source directivity, and propagation time by tracing a curved line associated with a particular starting point on a wave front. The method of using a wave-slowness vector, as delineated by Pierce (ref. 11), to describe the effect of wind on a ray path also proved useful in calculating a fluid frequency for absorption calculations. The slowness vector $\vec{s}$ is defined as the gradient of the wave front at the location of a ray and can be written as

$$\vec{s} = \frac{\hat{n}}{c + \vec{w} \cdot \hat{n}} \tag{A1}$$

where $\hat{n}$ is the wave front unit normal, c is the sound speed, and $\vec{w}$ is the wind velocity vector.

Atmosphere

The atmosphere was assumed to be horizontally stratified with no vertical component of wind and with both wind velocity and sound speed as functions of altitude only. This assumption greatly simplified integration of the ray tracing equations. All measured atmospheric parameters as well as the calculated density were assumed to vary linearly between the altitudes at which they were measured. The square of the sound speed was determined from both temperature and humidity. Because temperature is the dominant factor in the speed of sound calculation, the square of the sound speed was assumed to vary linearly between the altitudes at which the temperature was measured.

Absorption

Derivation of the linear acoustic wave equation neglects viscous dissipative forces, which leads to a conservative equation that ignores frequency dependent losses inherent in a real atmosphere. The loss model adopted for this propagation model is based on the ANSI standard (ref. 12) but is different in some respects. The new equations proposed by Bass, Sutherland, and Zuckerwar (ref. 13) for the relaxation frequencies of oxygen and nitrogen were used in place of those appearing in the standard. The equation of Goff and Gratch was used to determine the the saturation vapor pressure ratio.

The work of Roy (ref. 14) was used to define a frequency invariant

$$f_I = \frac{f_e}{1 - \vec{v} \cdot \vec{s}} \tag{A2}$$

that remains constant along a ray where f_e is a frequency emitted by the aircraft, f_I is the invariant frequency associated with that emitted frequency, $\vec{v}$ is the velocity of the aircraft, and $\vec{s}$ is the wave slowness vector. The frequency observed by a moving particle of air is given by

$$f_a = f_I (1 - \vec{w} \cdot \vec{s}) \tag{A3}$$

where $\vec{w}$ is the wind velocity vector associated with that air particle. It is this observed frequency f_a that is used to calculate absorption. The frequency observed by a microphone at a fixed point on the ground is just the invariant f_I. Absorption calculations require integration along the ray tube to determine the cumulative effect, but the propagation distance used for absorption was different from the ray length. The propagation distance for absorption was determined from the ray path by subtracting convection by winds.

Integration and Convergence

The assumption of a stratified atmosphere greatly simplified integration of the ray tracing equations by reducing them to three independent first order differential equations, two for mutually perpendicular horizontal directions and one for time. The equations within each layer were nonlinear in the independent variable (altitude) so a Gauss-Legendre numerical method was used to integrate each layer in sequence from the beginning of a ray. For each combination of source and receiver, three closely spaced rays were launched from the source at an initial estimate of the desired emission angles. Only the equations for the two horizontal directions were integrated. The varying amounts by which the rays missed the intended target were used to correct the initial launch angles via a two-dimensional secant method. The procedure was repeated until a ray landed within less than 0.5 ft of the receiver, more than 100 iterations occurred without convergence, or a ray vertexed (turned back upward) before reaching the ground. If a ray converged on the receiver, three final rays were launched. One of the rays was integrated to determine absorption and propagation time and the other two were used to calculate ray tube area and wave front curvature at the receiver.

Blokhintsev Invariant

According to Pierce (ref. 11), conservation of wave action requires that the Blokhintsev invariant

$$\frac{p^2|\vec{w}+c\hat{n}|A}{(1-\vec{w}\cdot\vec{s})\rho c^2} \tag{A4}$$

remain constant along an infinitesimal ray tube where p is the acoustic pressure amplitude, $\vec{w}$ is the wind velocity vector, c is the sound speed, $\hat{n}$ is the wave front unit normal, A is the ray tube area, $\vec{s}$ is the wave slowness vector, and ρ is the air density. In the absence of absorption from viscous effects, the acoustic pressure at the end of an infinitesimal ray tube p_1 can be written in terms of the acoustic pressure at the beginning p_0 and the atmospheric conditions at either end of the tube as

$$p_1^2 = p_0^2\left[\frac{A_0}{A_1}\right]\left[\frac{\rho_1 c_1}{\rho_0 c_0}\right]\left[\frac{|\vec{w}_0+c_0\hat{n}_0|(1-\vec{w}_1\cdot\vec{s}_1)c_1}{|\vec{w}_1+c_1\hat{n}_1|(1-\vec{w}_0\cdot\vec{s}_0)c_0}\right] \tag{A5}$$

The first term in brackets on the right represents spreading loss (if the ray tube area increases). The second term represents the familiar characteristic impedance correction. The third term is the Blokhintsev correction that is necessary to account for variations in the dynamic interaction of propagating waves with a moving medium. All three of these terms are included in received sound pressure level calculations. All three require only a knowledge of conditions at either end of a ray tube and involve no integration along the tube beyond what is needed to define the ray tube itself.

Ground Effects

The ground is modeled as a flat surface with complex impedance. The method of Chien and Soroka (ref. 15) was used for determining the sound level above an impedance plane for an incident spherical wave. The correction for partial signal coherence suggested by Pao, Wenzel, and Oncley (ref. 16) was included and the empirical relations of Delany and Bazley (ref. 17) were used to calculate the ground impedance from an estimate of the ground flow resistance. A ground flow resistance of 1000 slug/ft^3/s (515 000 kg/m^3/s) was assumed to be representative of the hard packed lake bed surface on which the microphones were placed. The model of Chien and Soroka assumes straight line propagation from source to receiver on both direct and reflected paths, and their equations are written in terms of path length and incident angle. Ray tracing yields curved propagation paths and wave front curvature that is not a function only of propagation distance, so the equations were recast in terms of wave front curvature and incident angle at the location of the receiver. In that the microphones were in direct contact with the ground boards, this ground effects correction equaled 6 ± 0.05 dB for all frequencies of interest.

Appendix B

Source Noise Power Spectral Densities

The power spectral density plots (figs. B1–B42) presented herein have been computed from ensemble averages over the 20 measuring microphones projected back to the aircraft by correcting for ground board, spherical spreading, and atmospheric absorption.

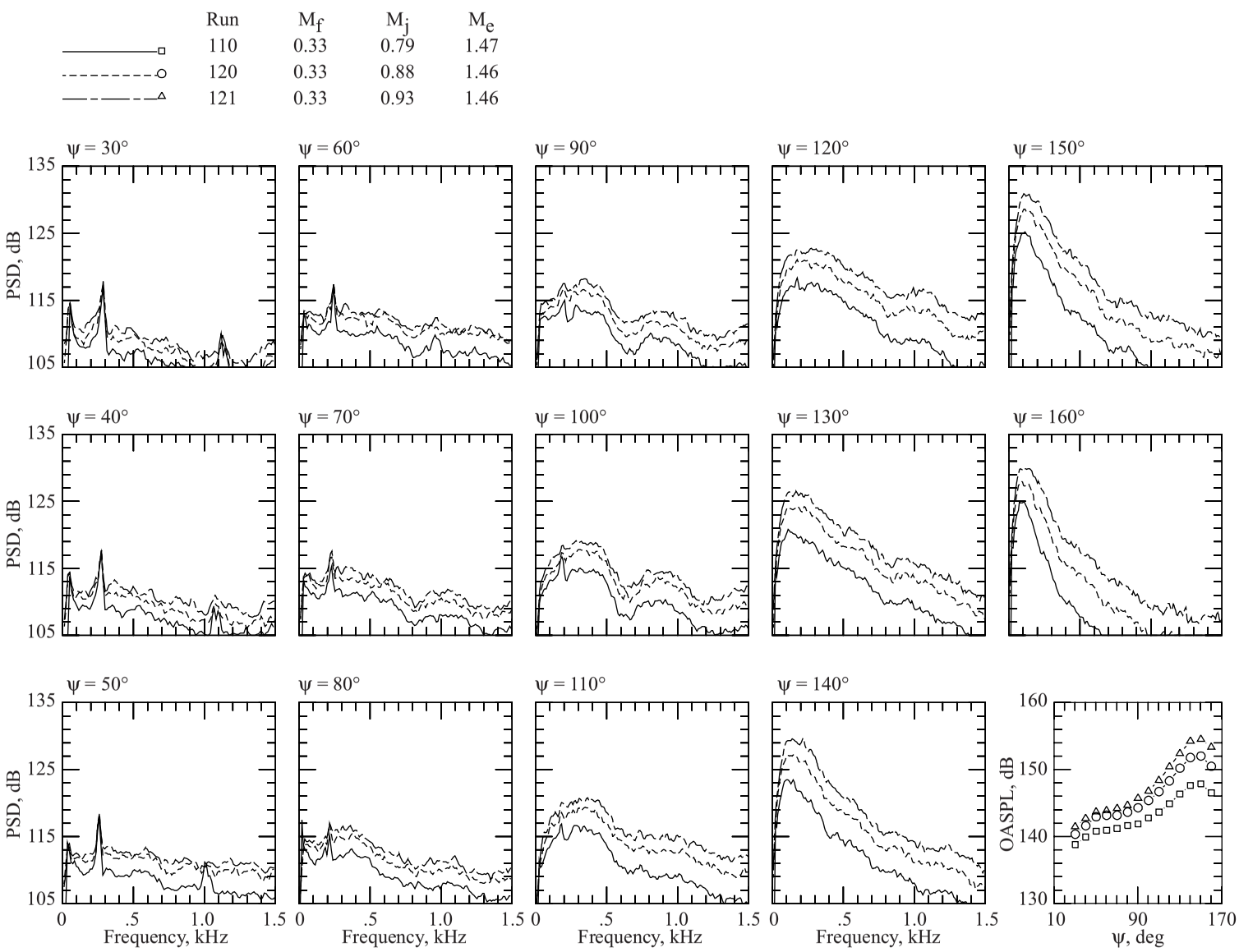
Run
M_f
M_j
M_e
110 0.33 0.79 1.47
120 0.33 0.88 1.46
121 0.33 0.93 1.46
ψ = 30°
ψ = 60°
ψ = 90°
ψ = 120°
ψ = 150°
ψ = 40°
ψ = 70°
ψ = 100°
ψ = 130°
ψ = 160°
ψ = 50°
ψ = 80°
ψ = 110°
ψ = 140°
PSD, dB
135
125
115
105
0
.5
1.0
1.5
Frequency, kHz
OASPL, dB
160
150
140
130
10
90
170
ψ, deg

Figure B1

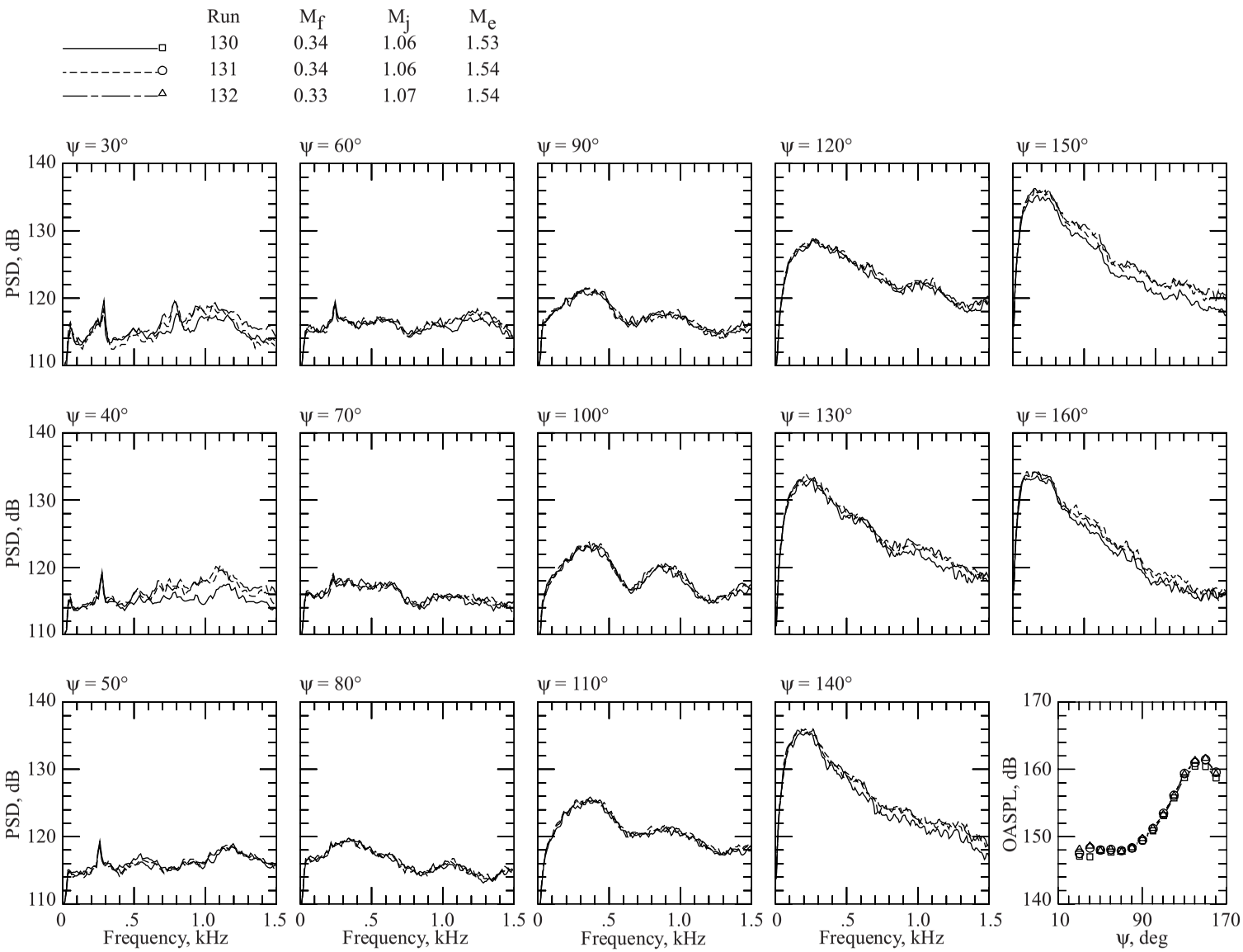
Run
M_f
M_j
M_e
130 0.34 1.06 1.53
131 0.34 1.06 1.54
132 0.33 1.07 1.54
ψ = 30°
ψ = 60°
ψ = 90°
ψ = 120°
ψ = 150°
ψ = 40°
ψ = 70°
ψ = 100°
ψ = 130°
ψ = 160°
ψ = 50°
ψ = 80°
ψ = 110°
ψ = 140°
PSD, dB
140
130
120
110
0
.5
1.0
1.5
Frequency, kHz
OASPL, dB
170
160
150
140
10
90
170
ψ, deg

Figure B2

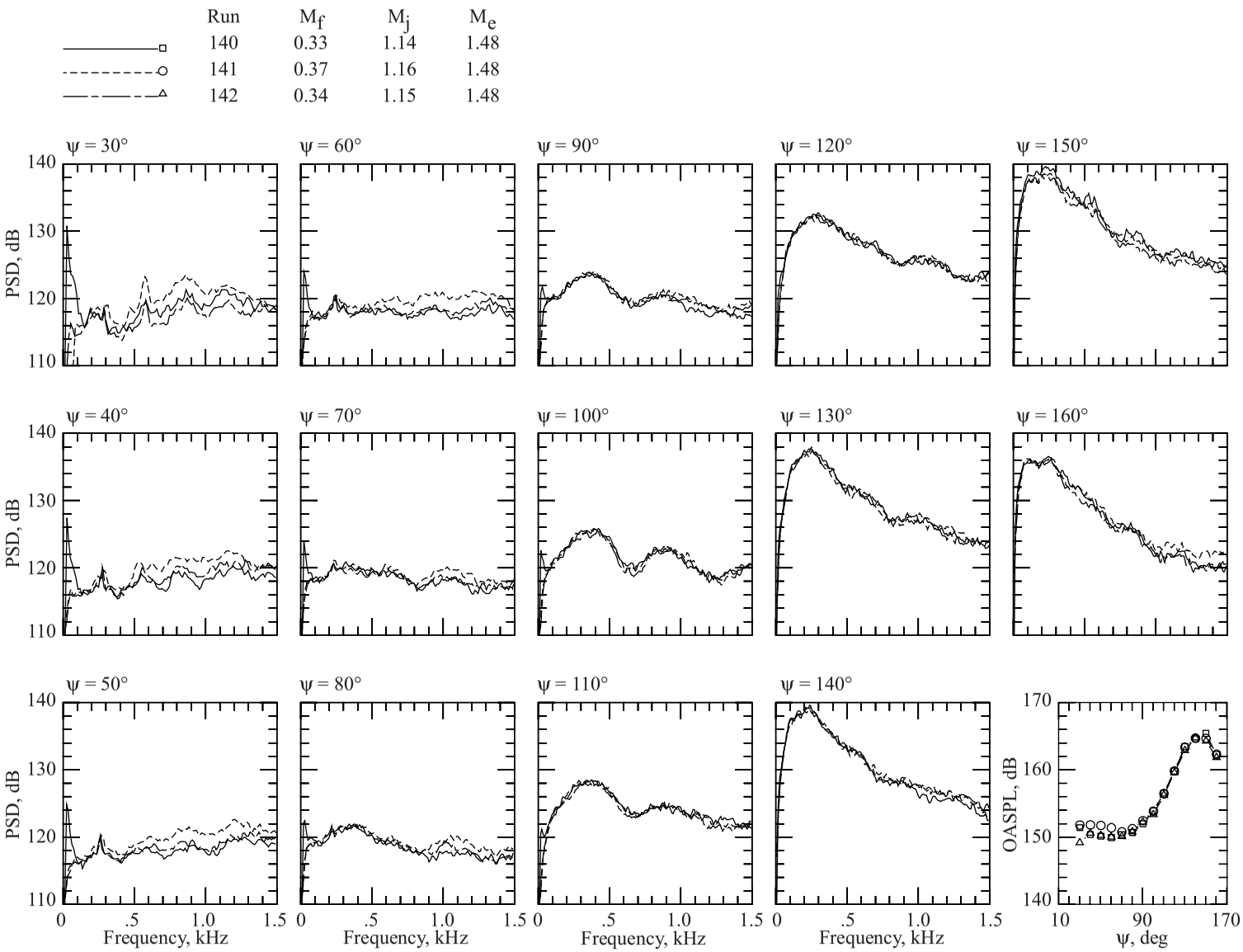
Run
M_f
M_j
M_e
140 0.33 1.14 1.48
141 0.37 1.16 1.48
142 0.34 1.15 1.48
ψ = 30°
ψ = 60°
ψ = 90°
ψ = 120°
ψ = 150°
ψ = 40°
ψ = 70°
ψ = 100°
ψ = 130°
ψ = 160°
ψ = 50°
ψ = 80°
ψ = 110°
ψ = 140°
PSD, dB
140
130
120
110
0
.5
1.0
1.5
Frequency, kHz
OASPL, dB
170
160
150
140
10
90
170
ψ, deg

Figure B3

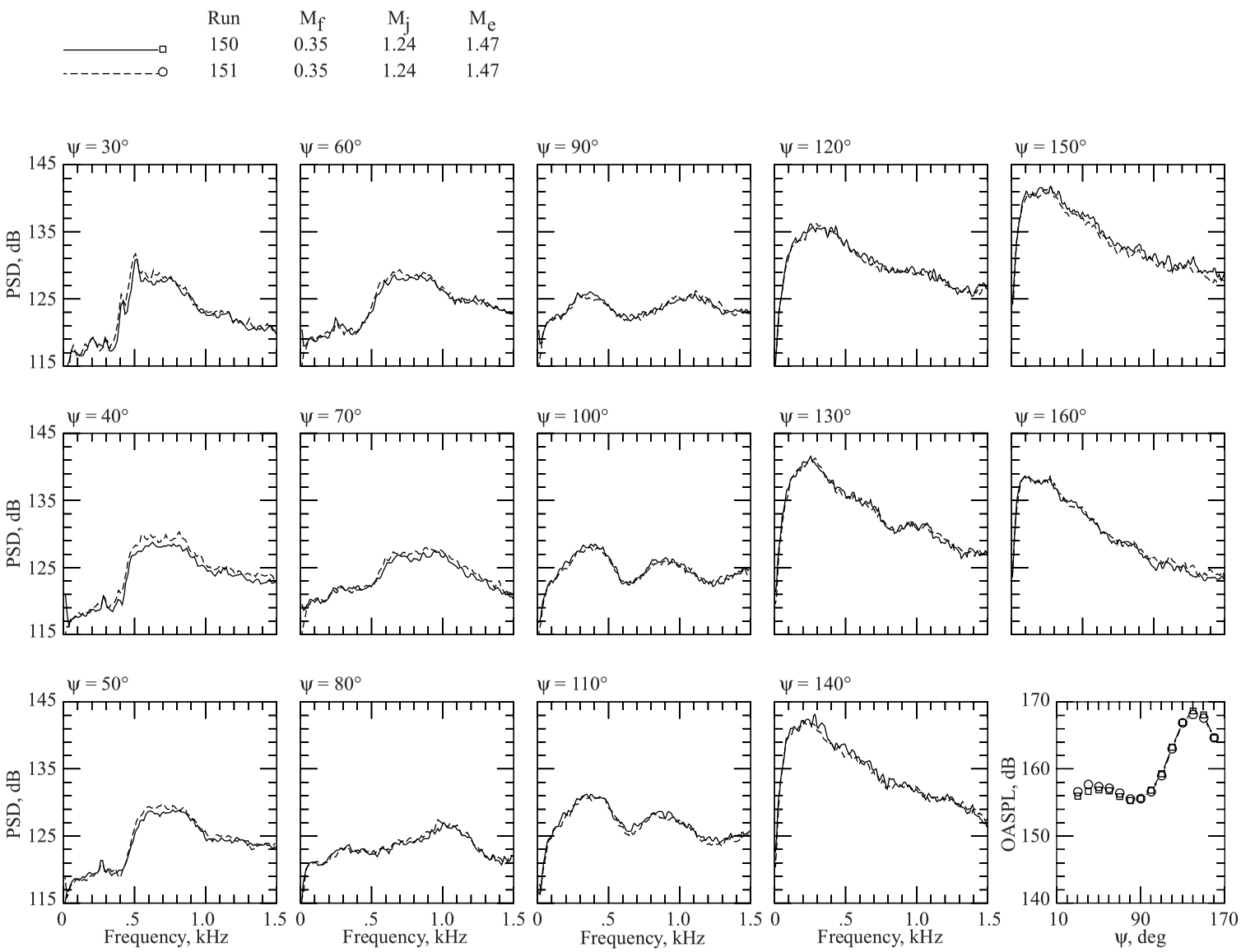
Run
M_f
M_j
M_e
150 0.35 1.24 1.47
151 0.35 1.24 1.47
ψ = 30°
ψ = 60°
ψ = 90°
ψ = 120°
ψ = 150°
ψ = 40°
ψ = 70°
ψ = 100°
ψ = 130°
ψ = 160°
ψ = 50°
ψ = 80°
ψ = 110°
ψ = 140°
PSD, dB
145
135
125
115
0
.5
1.0
1.5
Frequency, kHz
OASPL, dB
170
160
150
140
10
90
170
ψ, deg

Figure B4

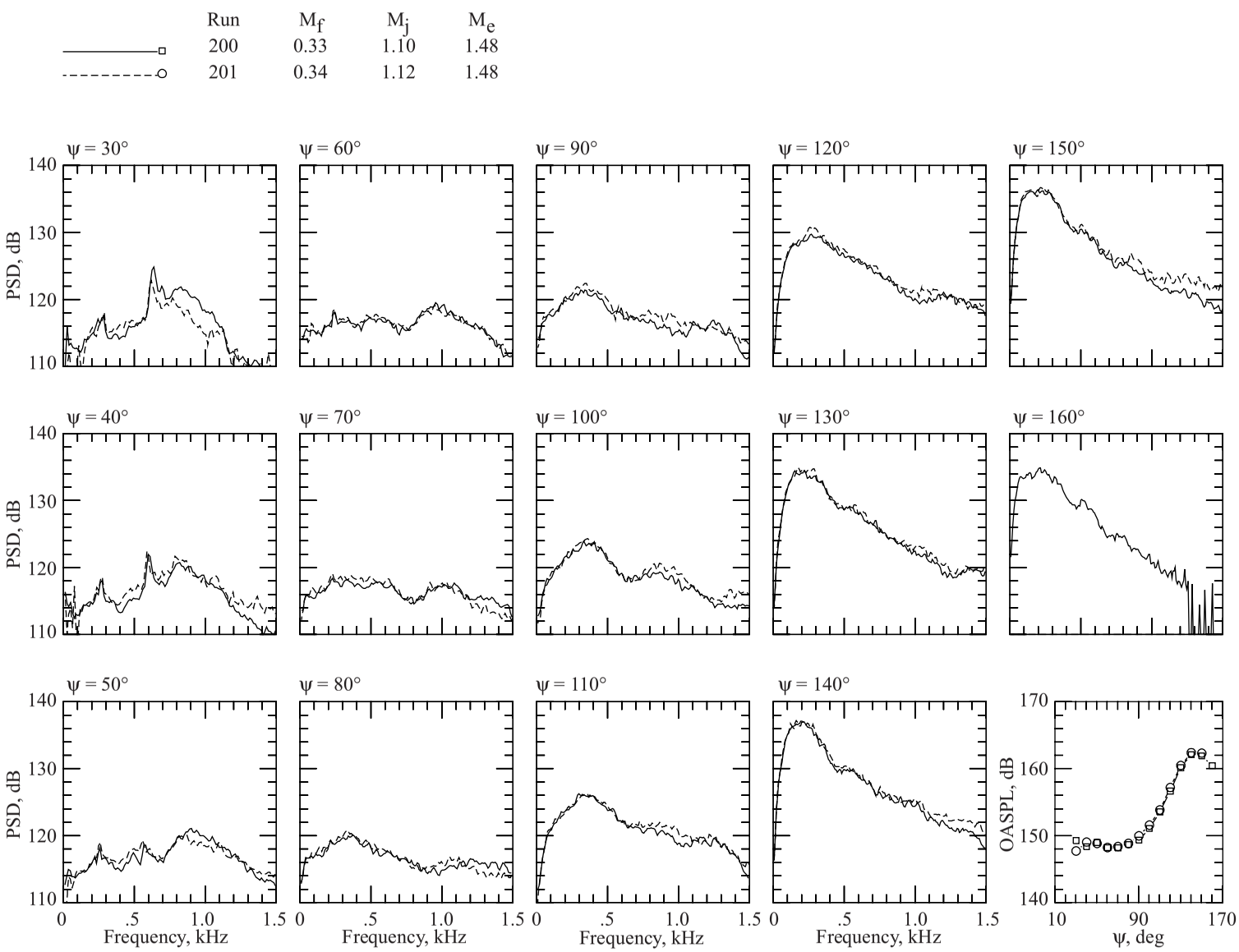
Run
M_f
M_j
M_e
200 0.33 1.10 1.48
201 0.34 1.12 1.48
ψ = 30°
ψ = 60°
ψ = 90°
ψ = 120°
ψ = 150°
ψ = 40°
ψ = 70°
ψ = 100°
ψ = 130°
ψ = 160°
ψ = 50°
ψ = 80°
ψ = 110°
ψ = 140°
PSD, dB
140
130
120
110
0
.5
1.0
1.5
Frequency, kHz
OASPL, dB
170
160
150
140
10
90
170
ψ, deg

Figure B5

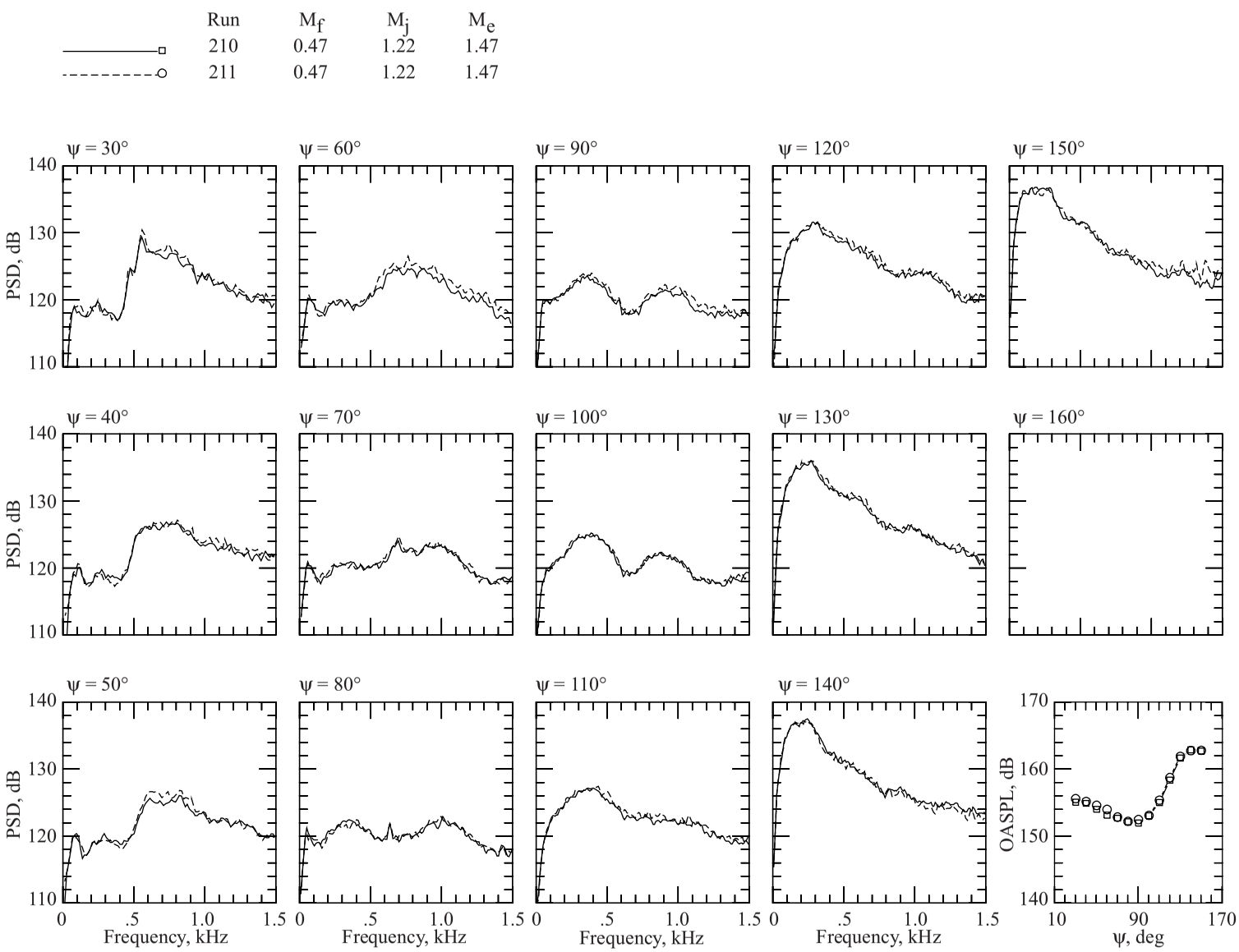
Run
M_f
M_j
M_e
210
0.47
1.22
1.47
211
0.47
1.22
1.47
ψ = 30°
ψ = 60°
ψ = 90°
ψ = 120°
ψ = 150°
ψ = 40°
ψ = 70°
ψ = 100°
ψ = 130°
ψ = 160°
ψ = 50°
ψ = 80°
ψ = 110°
ψ = 140°
PSD, dB
140
130
120
110
0
.5
1.0
1.5
Frequency, kHz
OASPL, dB
170
160
150
140
10
90
170
ψ, deg

Figure B6

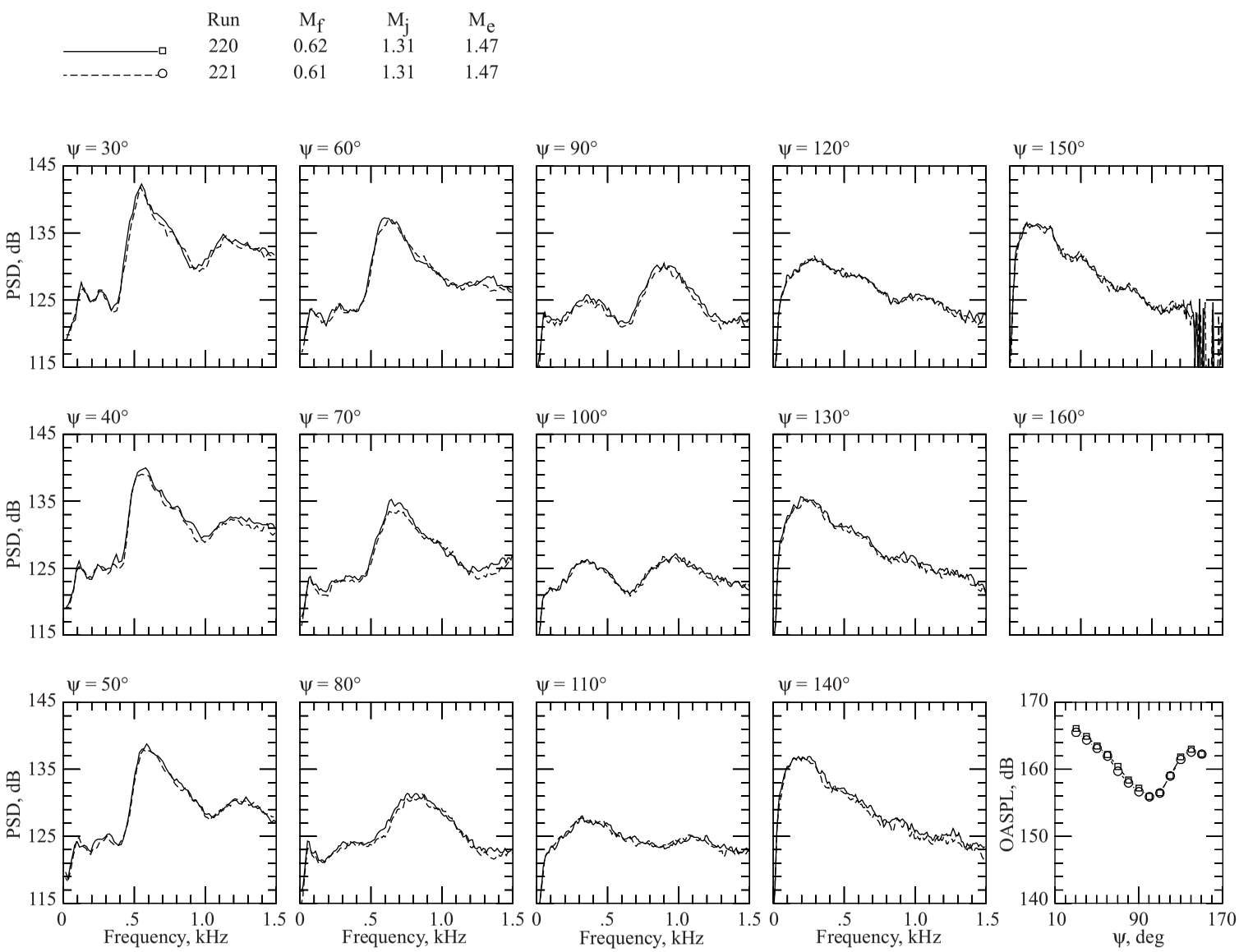
Run
M_f
M_j
M_e
220
0.62
1.31
1.47
221
0.61
1.31
1.47
ψ = 30°
ψ = 60°
ψ = 90°
ψ = 120°
ψ = 150°
ψ = 40°
ψ = 70°
ψ = 100°
ψ = 130°
ψ = 160°
ψ = 50°
ψ = 80°
ψ = 110°
ψ = 140°
PSD, dB
145
135
125
115
0
.5
1.0
1.5
Frequency, kHz
OASPL, dB
170
160
150
140
10
90
170
ψ, deg

Figure B7

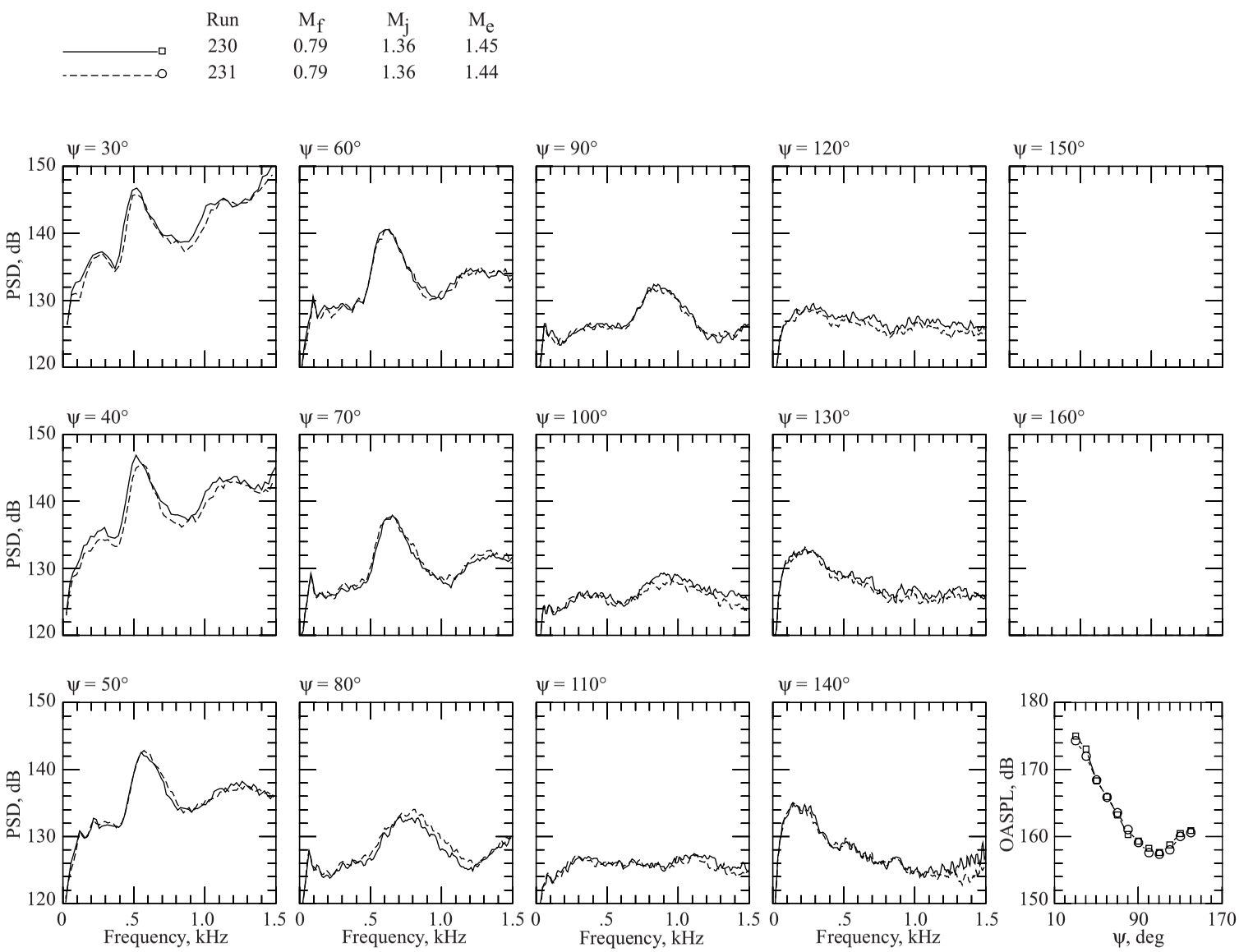
Run
M_f
M_j
M_e
230
0.79
1.36
1.45
231
0.79
1.36
1.44
ψ = 30°
ψ = 60°
ψ = 90°
ψ = 120°
ψ = 150°
ψ = 40°
ψ = 70°
ψ = 100°
ψ = 130°
ψ = 160°
ψ = 50°
ψ = 80°
ψ = 110°
ψ = 140°
PSD, dB
150
140
130
120
0
.5
1.0
1.5
Frequency, kHz
OASPL, dB
180
170
160
150
10
90
170
ψ, deg

Figure B8

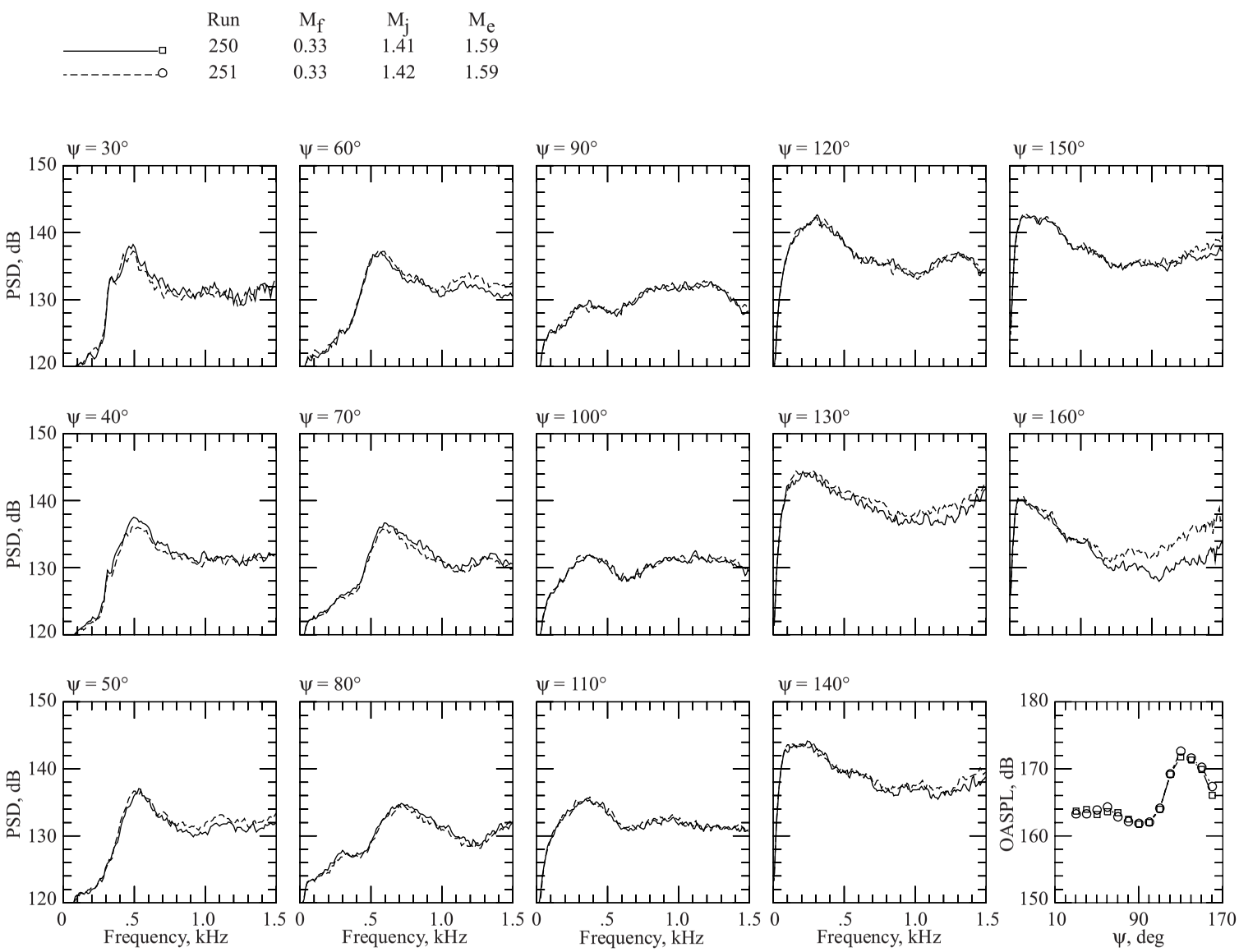
Run
M_f
M_j
M_e
250 0.33 1.41 1.59
251 0.33 1.42 1.59
ψ = 30°
ψ = 60°
ψ = 90°
ψ = 120°
ψ = 150°
ψ = 40°
ψ = 70°
ψ = 100°
ψ = 130°
ψ = 160°
ψ = 50°
ψ = 80°
ψ = 110°
ψ = 140°
PSD, dB
150
140
130
120
0
.5
1.0
1.5
Frequency, kHz
OASPL, dB
180
170
160
150
10
90
170
ψ, deg

Figure B9

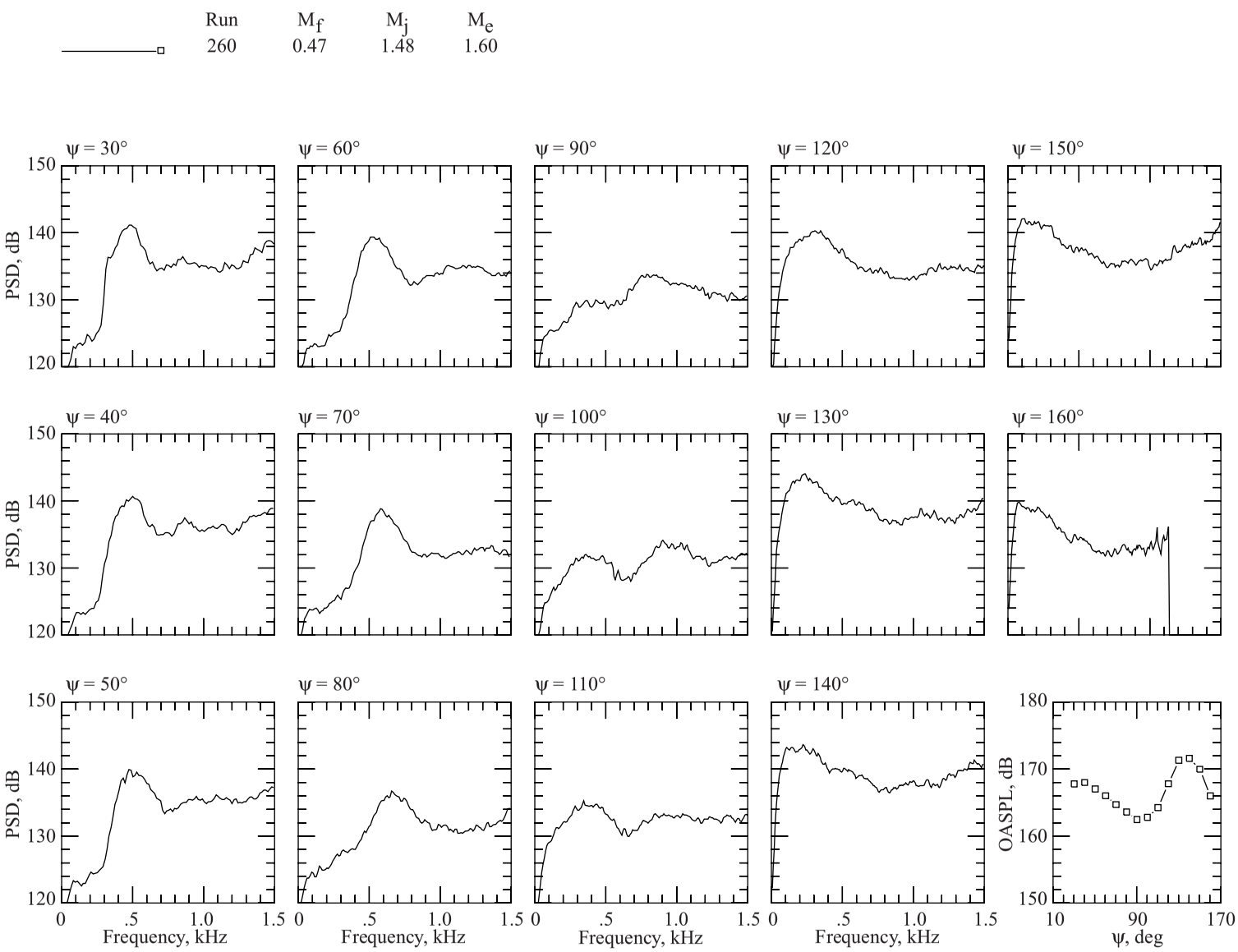
Run
260
M_f
0.47
M_j
1.48
M_e
1.60
ψ = 30°
ψ = 60°
ψ = 90°
ψ = 120°
ψ = 150°
ψ = 40°
ψ = 70°
ψ = 100°
ψ = 130°
ψ = 160°
ψ = 50°
ψ = 80°
ψ = 110°
ψ = 140°
PSD, dB
150
140
130
120
0
.5
1.0
1.5
Frequency, kHz
OASPL, dB
180
170
160
150
10
90
170
ψ, deg

Figure B10

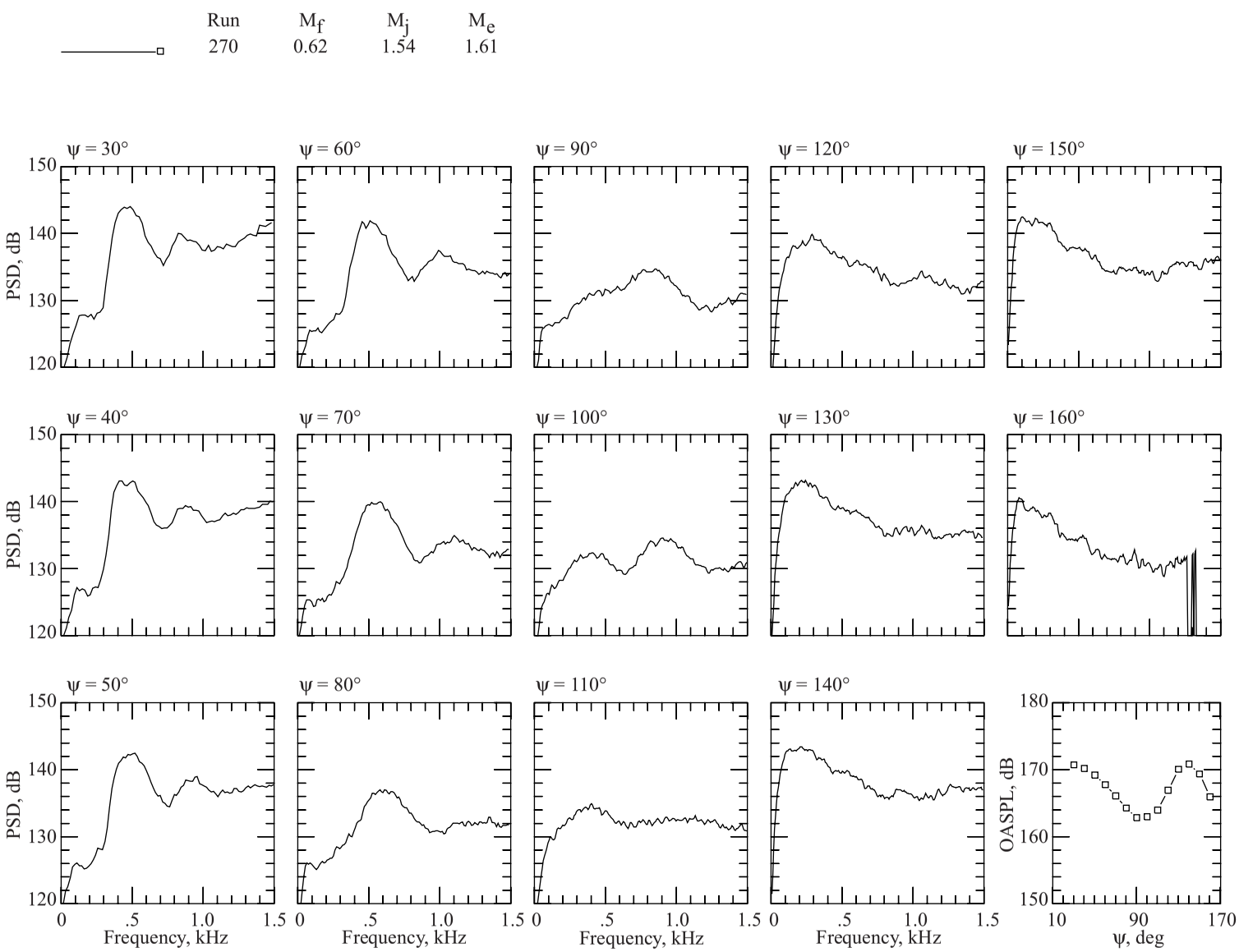
Run
270
M_f
0.62
M_j
1.54
M_e
1.61
ψ = 30°
ψ = 60°
ψ = 90°
ψ = 120°
ψ = 150°
ψ = 40°
ψ = 70°
ψ = 100°
ψ = 130°
ψ = 160°
ψ = 50°
ψ = 80°
ψ = 110°
ψ = 140°
PSD, dB
150
140
130
120
0
.5
1.0
1.5
Frequency, kHz
OASPL, dB
180
170
160
150
10
90
170
ψ, deg

Figure B11

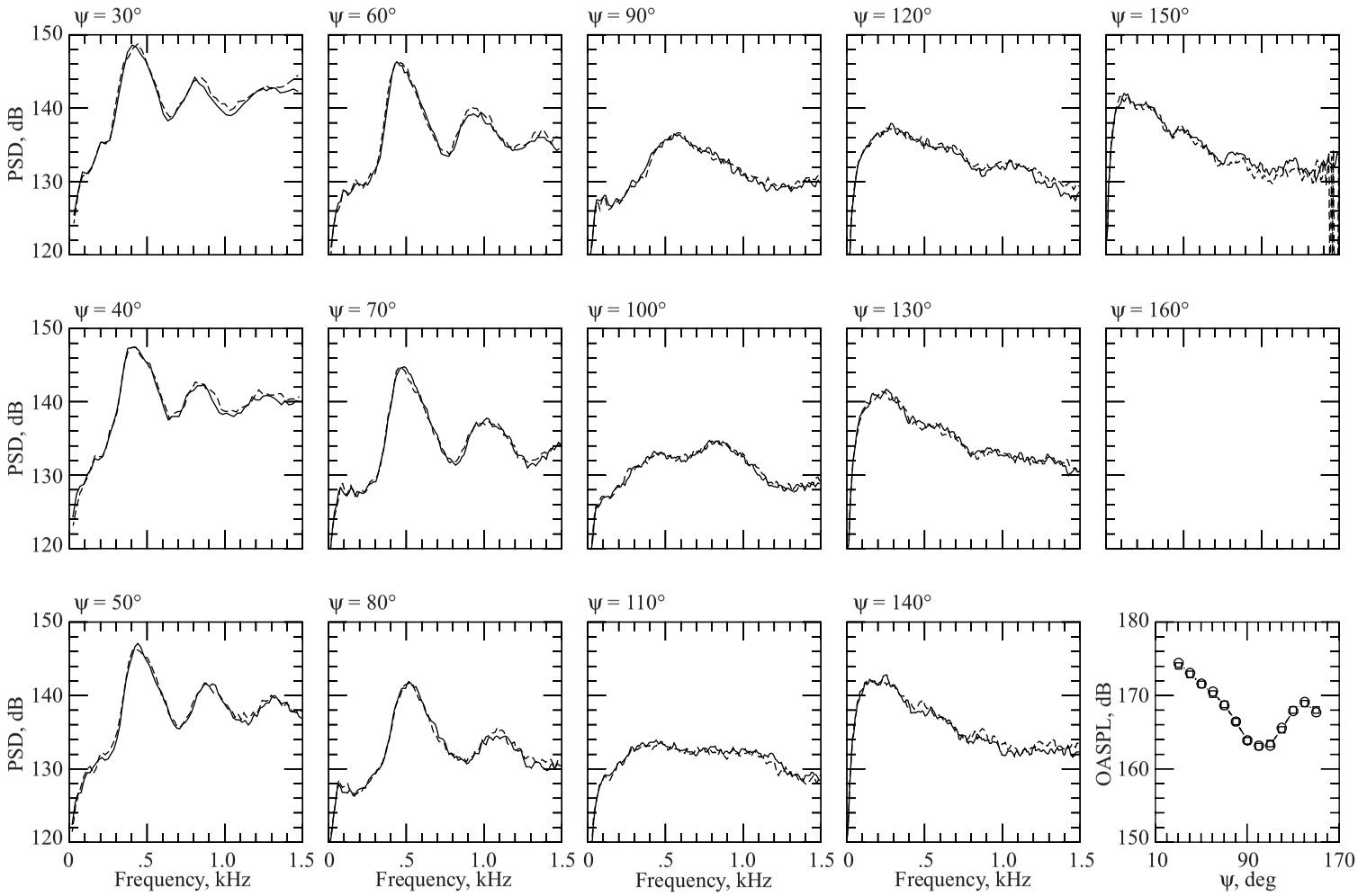
Run
280
281
M_f
0.76
0.77
M_j
1.58
1.59
M_e
1.69
1.69
ψ = 30°
ψ = 60°
ψ = 90°
ψ = 120°
ψ = 150°
ψ = 40°
ψ = 70°
ψ = 100°
ψ = 130°
ψ = 160°
ψ = 50°
ψ = 80°
ψ = 110°
ψ = 140°
PSD, dB
150
140
130
120
0
.5
1.0
1.5
Frequency, kHz
OASPL, dB
180
170
160
150
10
90
170
ψ, deg

Figure B12

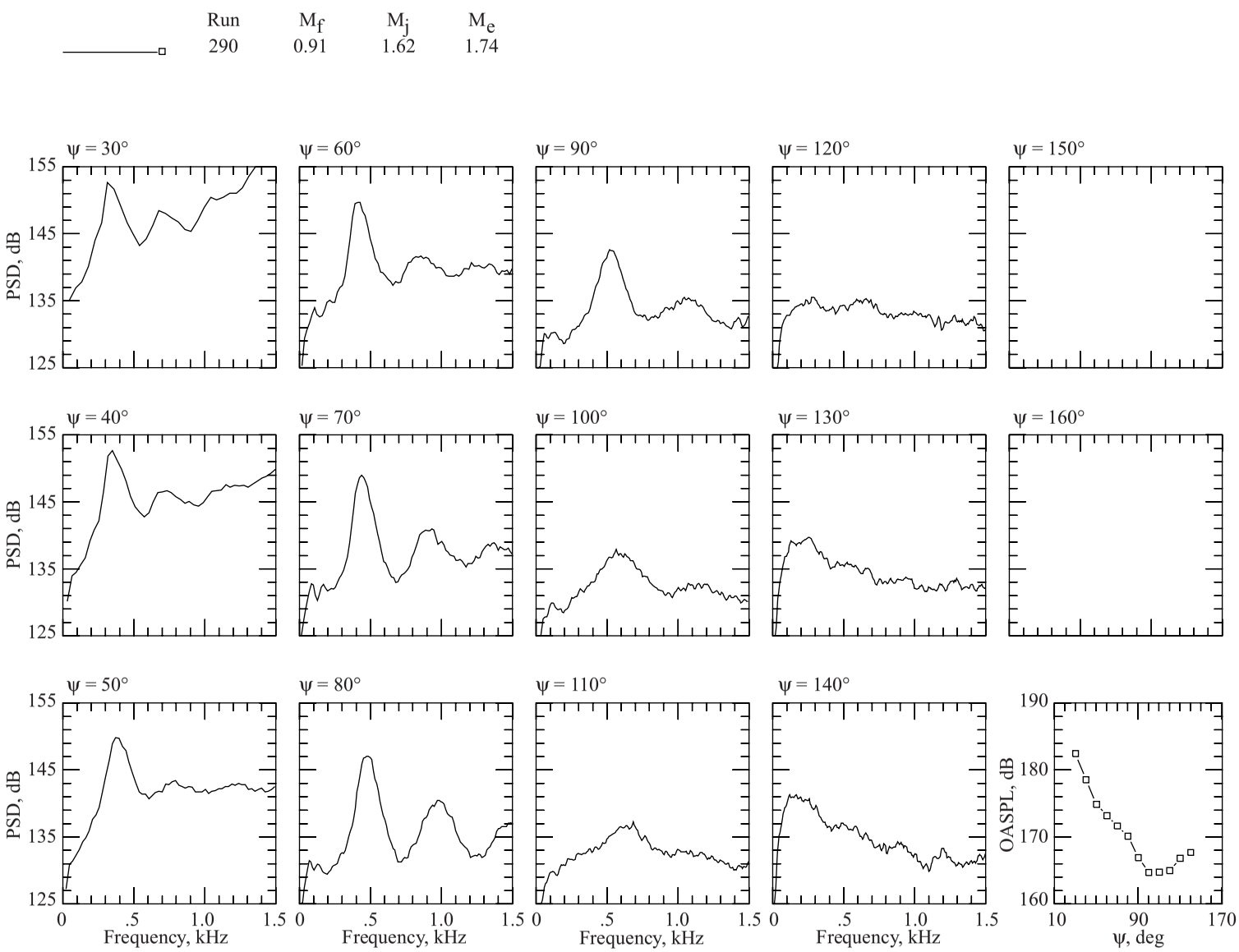
Run
290
M_f
0.91
M_j
1.62
M_e
1.74
ψ = 30°
ψ = 60°
ψ = 90°
ψ = 120°
ψ = 150°
ψ = 40°
ψ = 70°
ψ = 100°
ψ = 130°
ψ = 160°
ψ = 50°
ψ = 80°
ψ = 110°
ψ = 140°
PSD, dB
155
145
135
125
0
.5
1.0
1.5
Frequency, kHz
OASPL, dB
190
180
170
160
10
90
170
ψ, deg

Figure B13

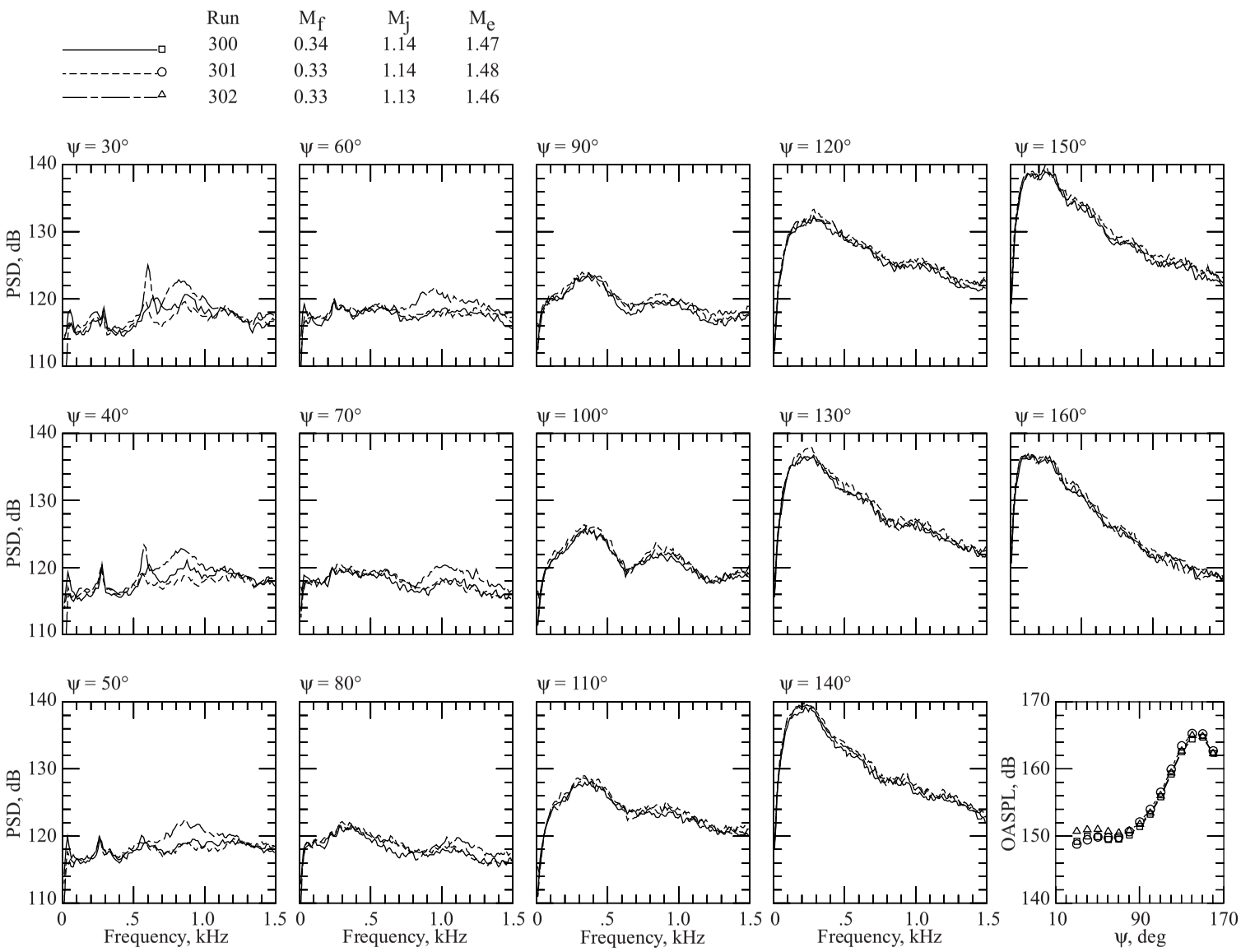
Run
M_f
M_j
M_e
300 0.34 1.14 1.47
301 0.33 1.14 1.48
302 0.33 1.13 1.46
ψ = 30°
ψ = 60°
ψ = 90°
ψ = 120°
ψ = 150°
ψ = 40°
ψ = 70°
ψ = 100°
ψ = 130°
ψ = 160°
ψ = 50°
ψ = 80°
ψ = 110°
ψ = 140°
PSD, dB
OASPL, dB
Frequency, kHz
ψ, deg

Figure B14

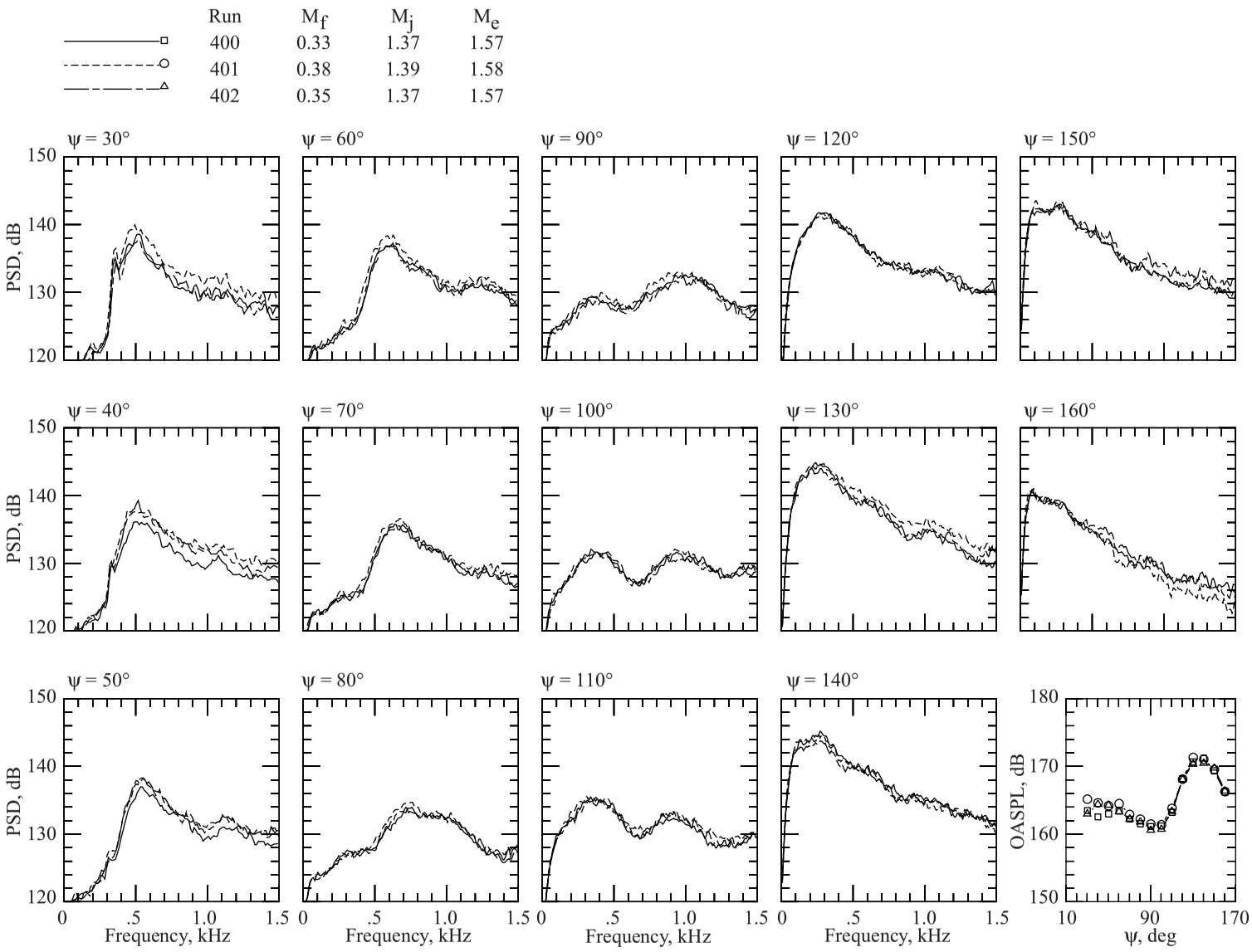
Run
M_f
M_j
M_e
400 0.33 1.37 1.57
401 0.38 1.39 1.58
402 0.35 1.37 1.57
ψ = 30°
ψ = 60°
ψ = 90°
ψ = 120°
ψ = 150°
ψ = 40°
ψ = 70°
ψ = 100°
ψ = 130°
ψ = 160°
ψ = 50°
ψ = 80°
ψ = 110°
ψ = 140°
PSD, dB
150
140
130
120
0
.5
1.0
1.5
Frequency, kHz
OASPL, dB
180
170
160
150
10
90
170
ψ, deg

Figure B15

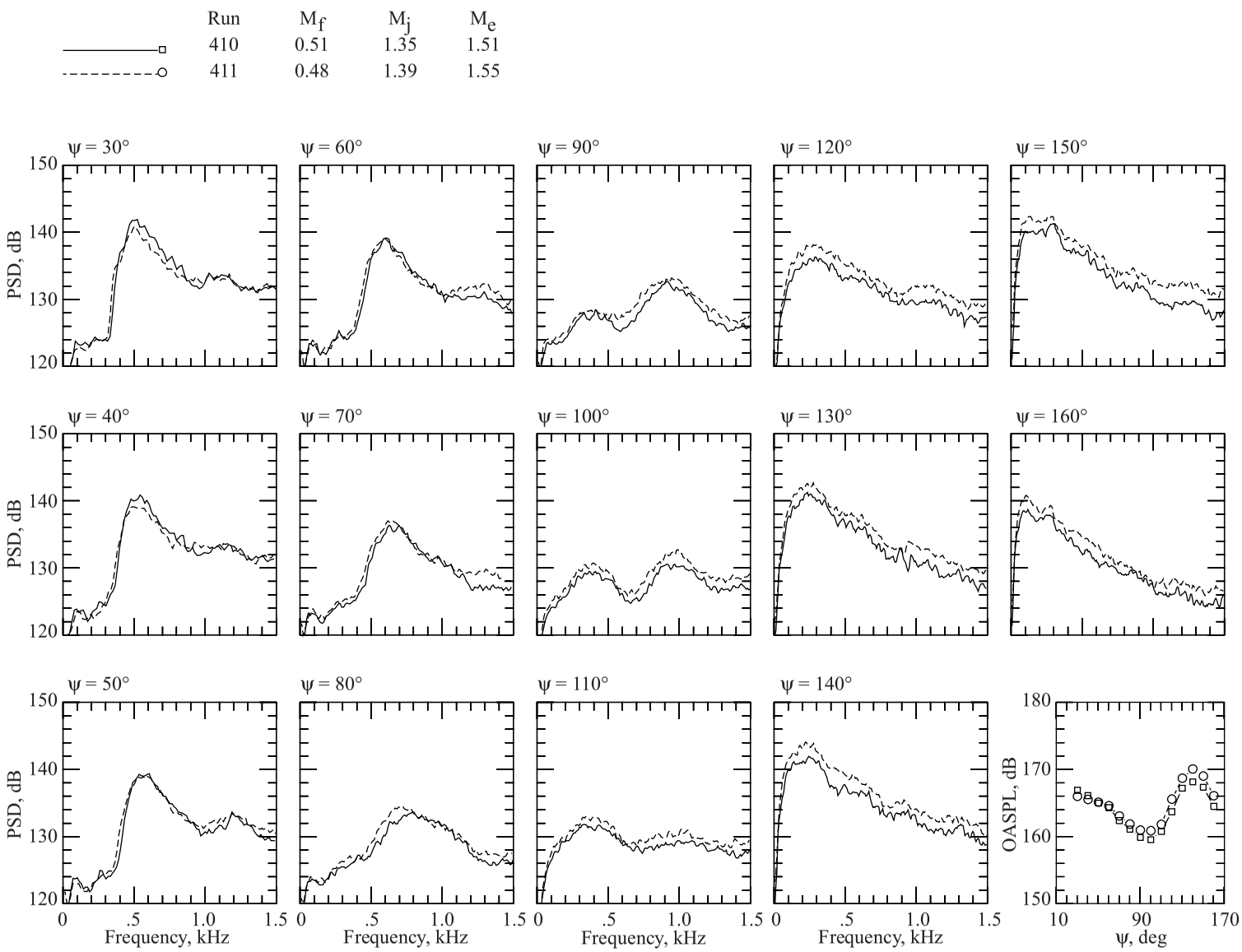
Run
M_f
M_j
M_e
410
0.51
1.35
1.51
411
0.48
1.39
1.55
ψ = 30°
ψ = 60°
ψ = 90°
ψ = 120°
ψ = 150°
ψ = 40°
ψ = 70°
ψ = 100°
ψ = 130°
ψ = 160°
ψ = 50°
ψ = 80°
ψ = 110°
ψ = 140°
PSD, dB
150
140
130
120
0
.5
1.0
1.5
Frequency, kHz
OASPL, dB
180
170
160
150
10
90
170
ψ, deg

Figure B16

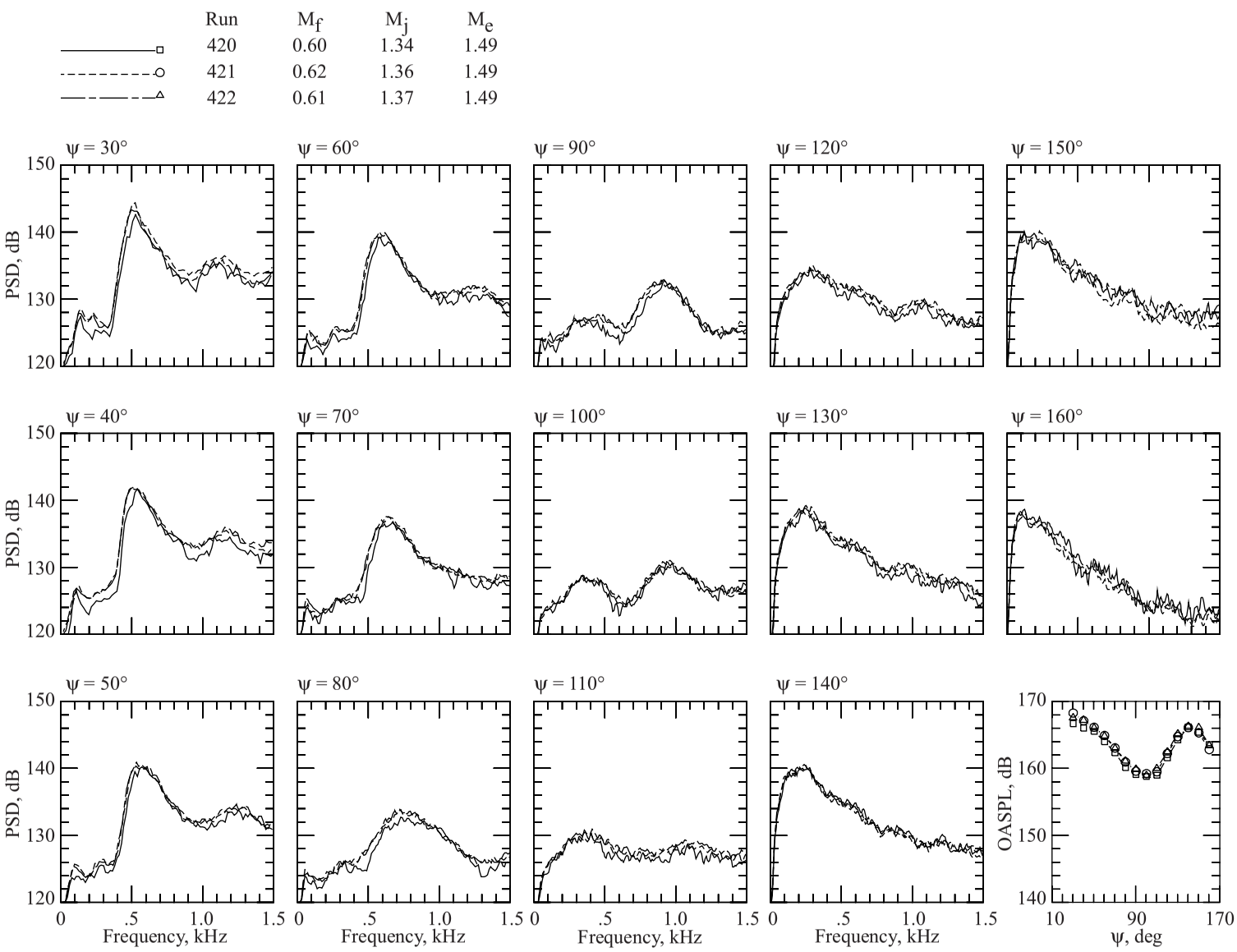
Run
M_f
M_j
M_e
420 0.60 1.34 1.49
421 0.62 1.36 1.49
422 0.61 1.37 1.49
ψ = 30°
ψ = 60°
ψ = 90°
ψ = 120°
ψ = 150°
ψ = 40°
ψ = 70°
ψ = 100°
ψ = 130°
ψ = 160°
ψ = 50°
ψ = 80°
ψ = 110°
ψ = 140°
PSD, dB
150
140
130
120
0
.5
1.0
1.5
Frequency, kHz
OASPL, dB
170
160
150
140
10
90
170
ψ, deg

Figure B17

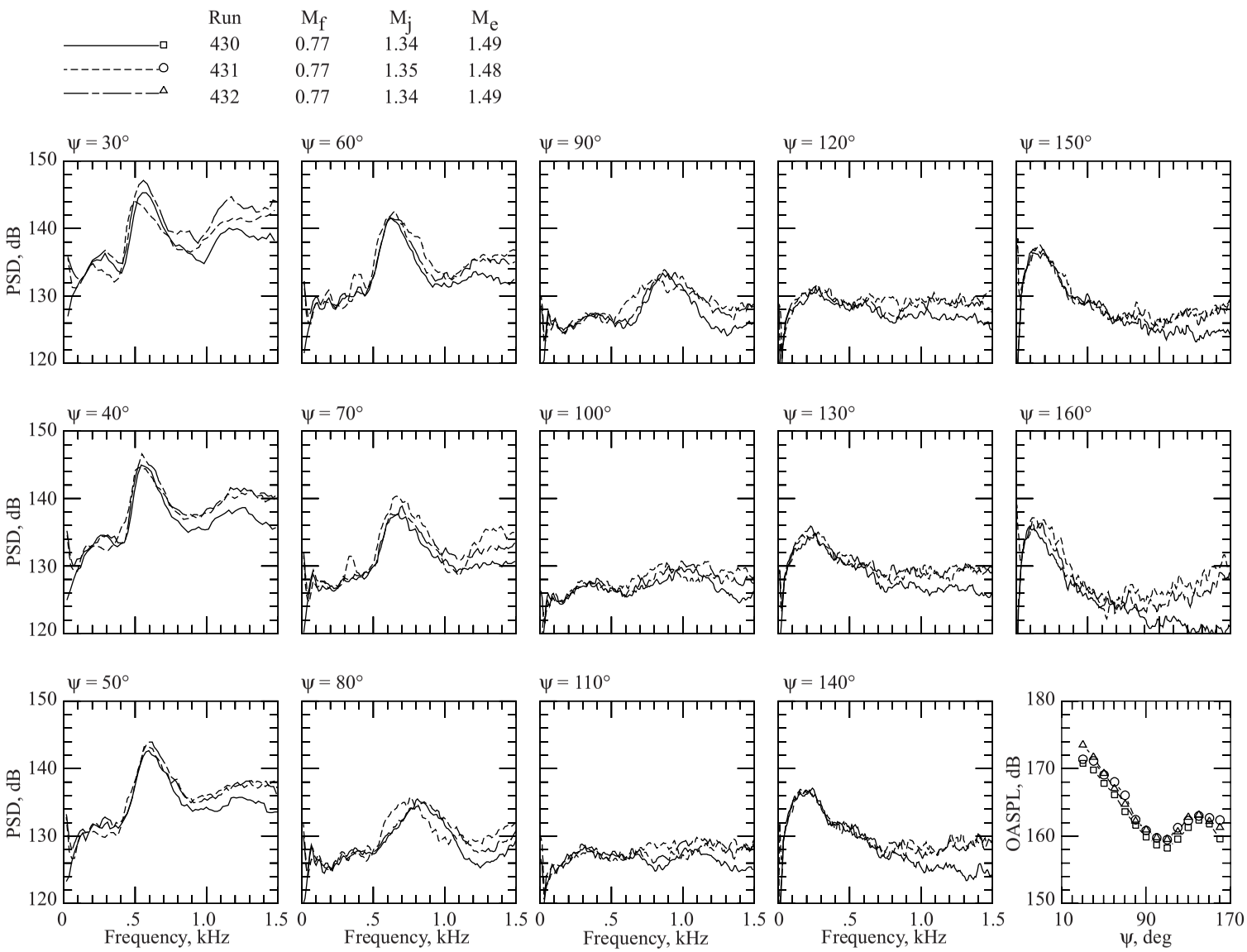
Run
M_f
M_j
M_e
430 0.77 1.34 1.49
431 0.77 1.35 1.48
432 0.77 1.34 1.49
ψ = 30°
ψ = 60°
ψ = 90°
ψ = 120°
ψ = 150°
ψ = 40°
ψ = 70°
ψ = 100°
ψ = 130°
ψ = 160°
ψ = 50°
ψ = 80°
ψ = 110°
ψ = 140°
PSD, dB
150
140
130
120
0
.5
1.0
1.5
Frequency, kHz
OASPL, dB
180
170
160
150
10
90
170
ψ, deg

Figure B18

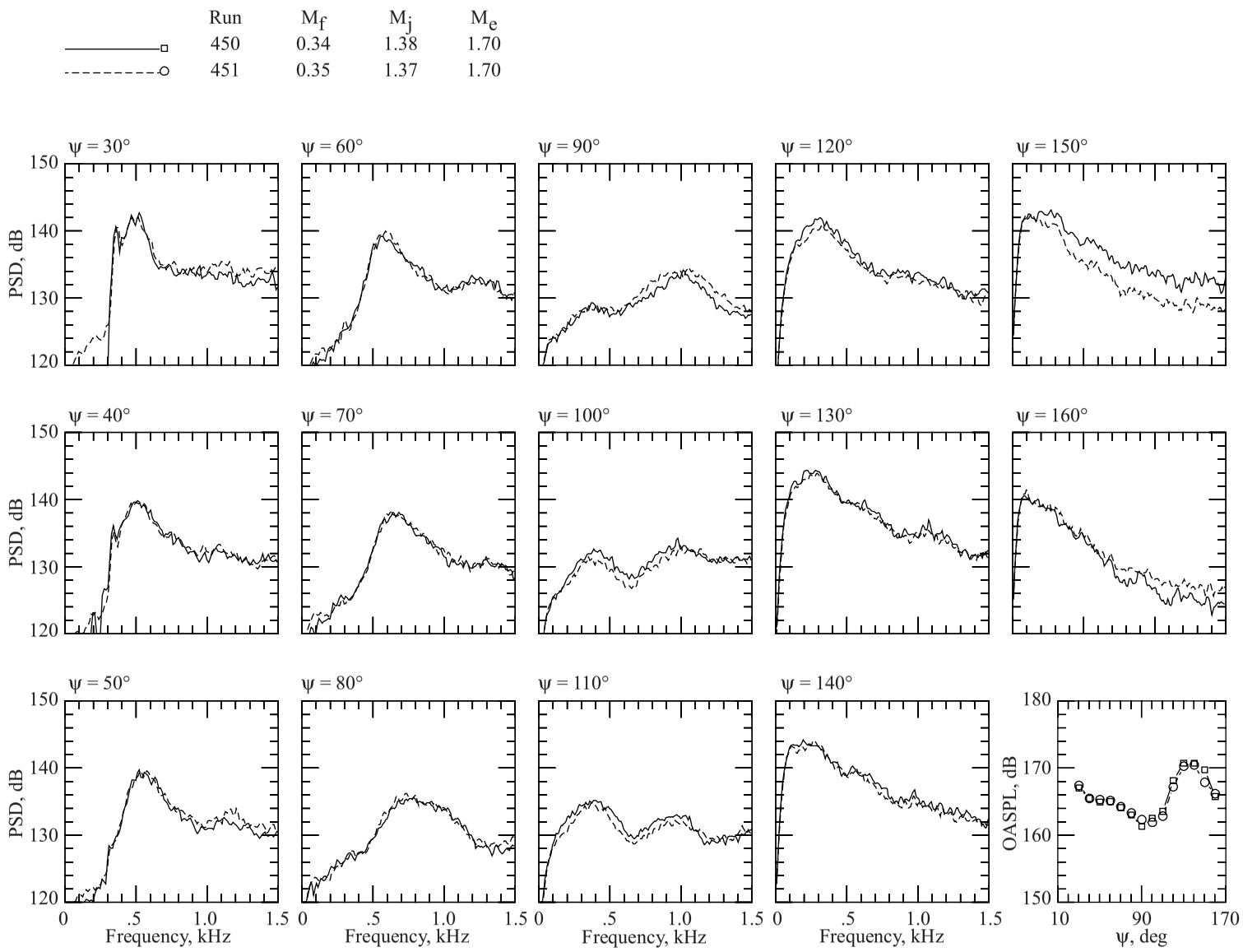
Run
M_f
M_j
M_e
450
0.34
1.38
1.70
451
0.35
1.37
1.70
ψ = 30°
ψ = 60°
ψ = 90°
ψ = 120°
ψ = 150°
ψ = 40°
ψ = 70°
ψ = 100°
ψ = 130°
ψ = 160°
ψ = 50°
ψ = 80°
ψ = 110°
ψ = 140°
PSD, dB
150
140
130
120
0
.5
1.0
1.5
Frequency, kHz
OASPL, dB
180
170
160
150
10
90
170
ψ, deg

Figure B19

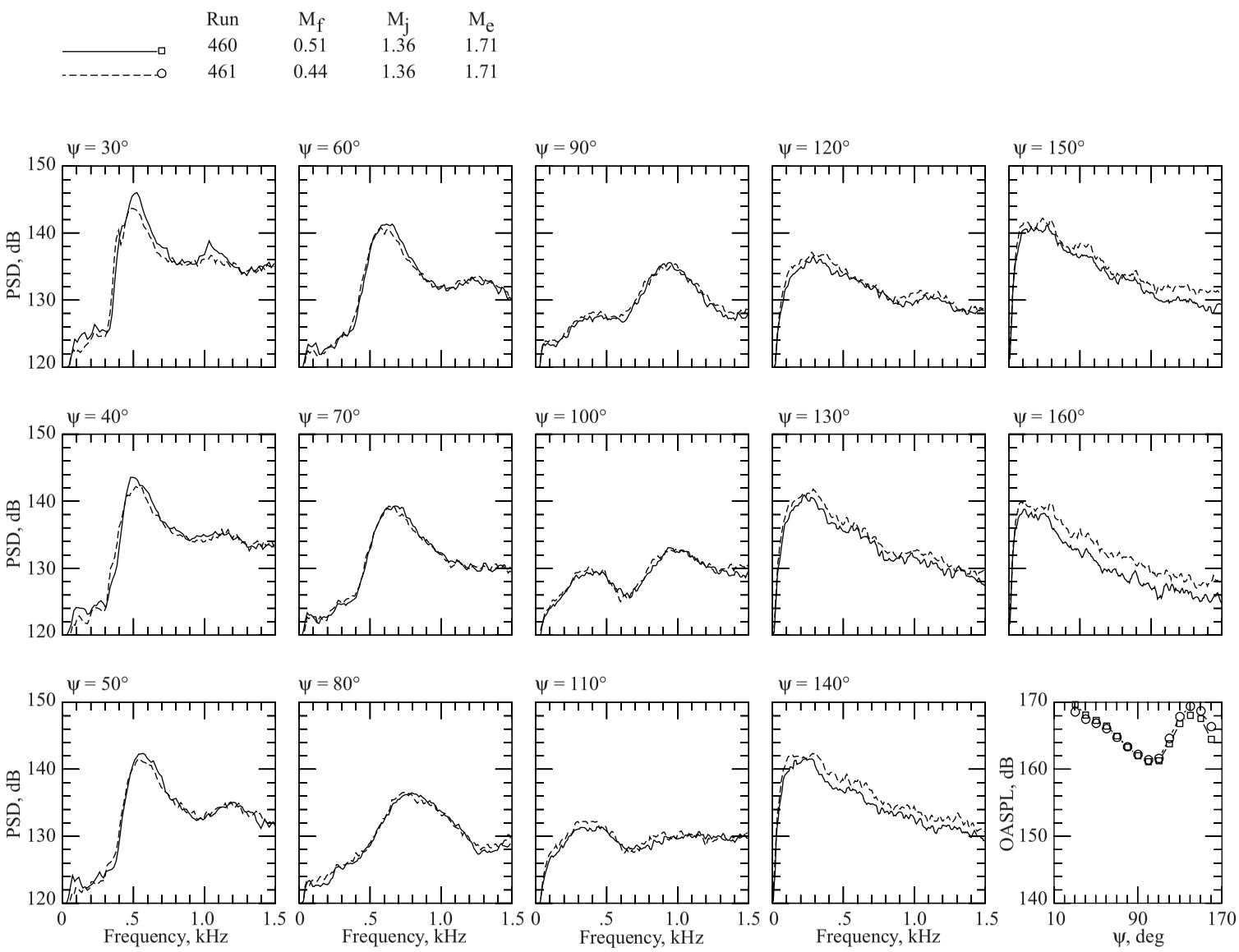
Run
M_f
M_j
M_e
460
0.51
1.36
1.71
461
0.44
1.36
1.71
ψ = 30°
ψ = 60°
ψ = 90°
ψ = 120°
ψ = 150°
ψ = 40°
ψ = 70°
ψ = 100°
ψ = 130°
ψ = 160°
ψ = 50°
ψ = 80°
ψ = 110°
ψ = 140°
PSD, dB
150
140
130
120
0
.5
1.0
1.5
Frequency, kHz
OASPL, dB
170
160
150
140
10
90
170
ψ, deg

Figure B20

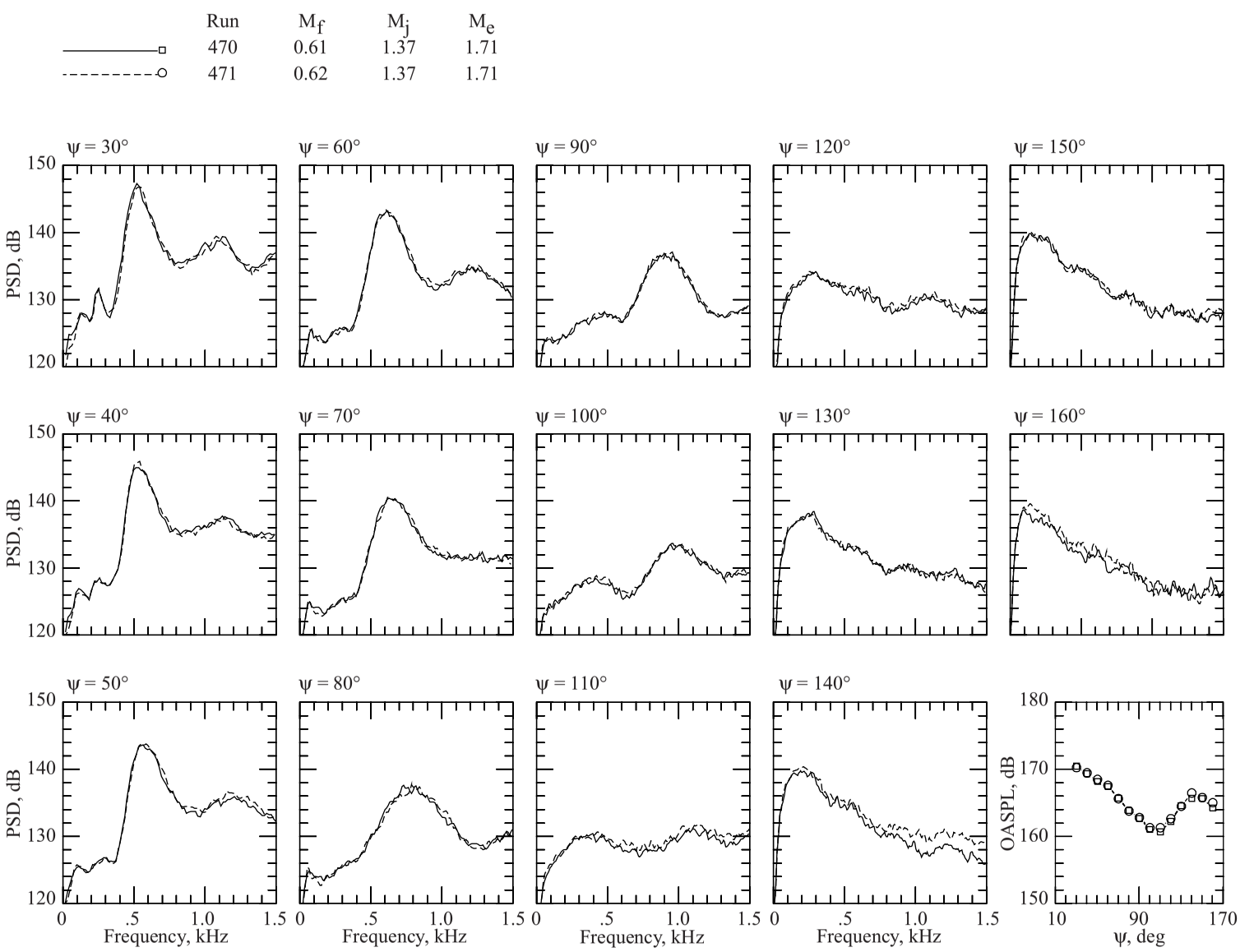
Run
M_f
M_j
M_e
470 0.61 1.37 1.71
471 0.62 1.37 1.71
ψ = 30°
ψ = 60°
ψ = 90°
ψ = 120°
ψ = 150°
ψ = 40°
ψ = 70°
ψ = 100°
ψ = 130°
ψ = 160°
ψ = 50°
ψ = 80°
ψ = 110°
ψ = 140°
PSD, dB
150
140
130
120
0
.5
1.0
1.5
Frequency, kHz
OASPL, dB
180
170
160
150
10
90
170
ψ, deg

Figure B21

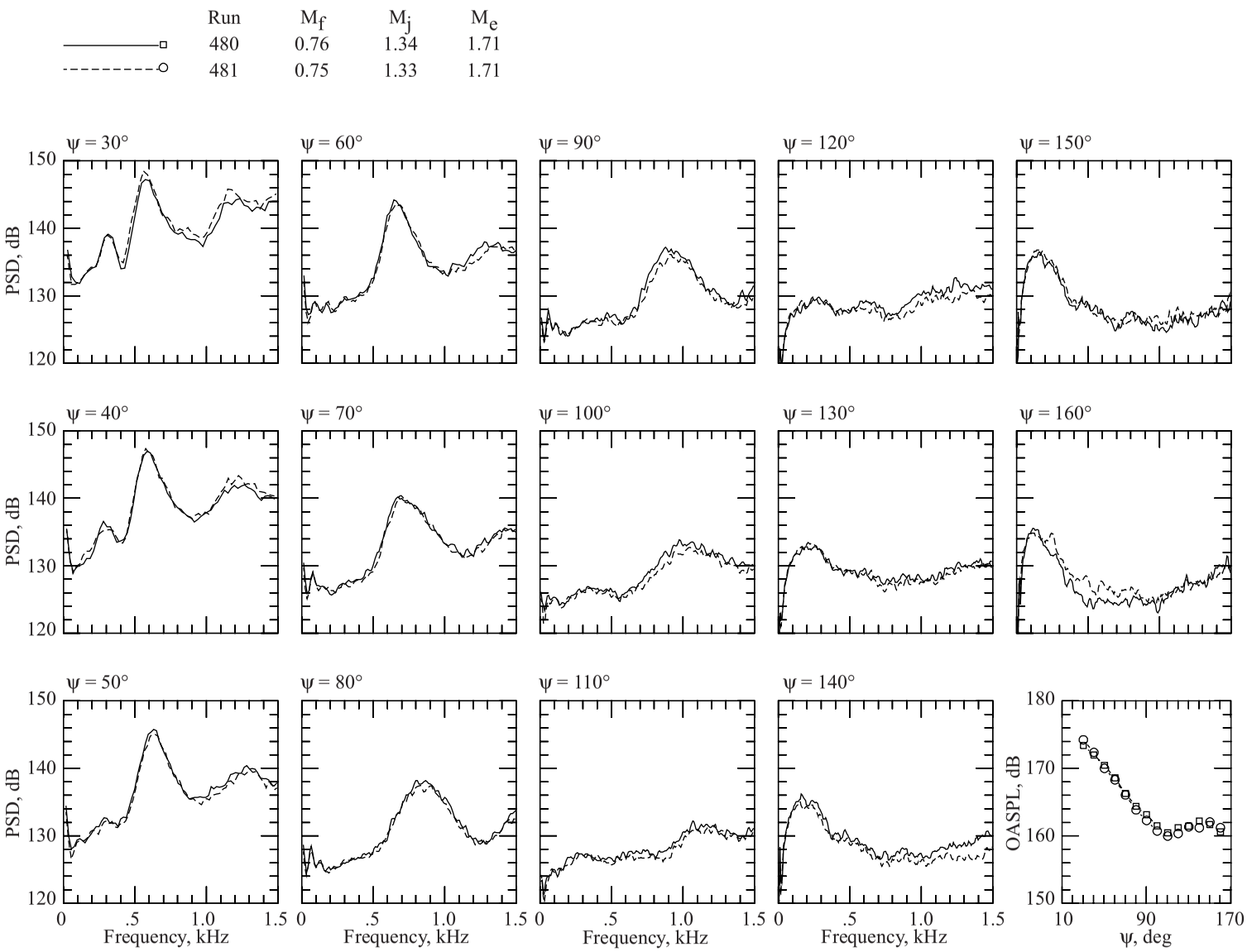
Run
480
481
M_f
0.76
0.75
M_j
1.34
1.33
M_e
1.71
1.71
ψ = 30°
ψ = 60°
ψ = 90°
ψ = 120°
ψ = 150°
ψ = 40°
ψ = 70°
ψ = 100°
ψ = 130°
ψ = 160°
ψ = 50°
ψ = 80°
ψ = 110°
ψ = 140°
PSD, dB
150
140
130
120
0
.5
1.0
1.5
Frequency, kHz
OASPL, dB
180
170
160
150
10
90
170
ψ, deg

Figure B22

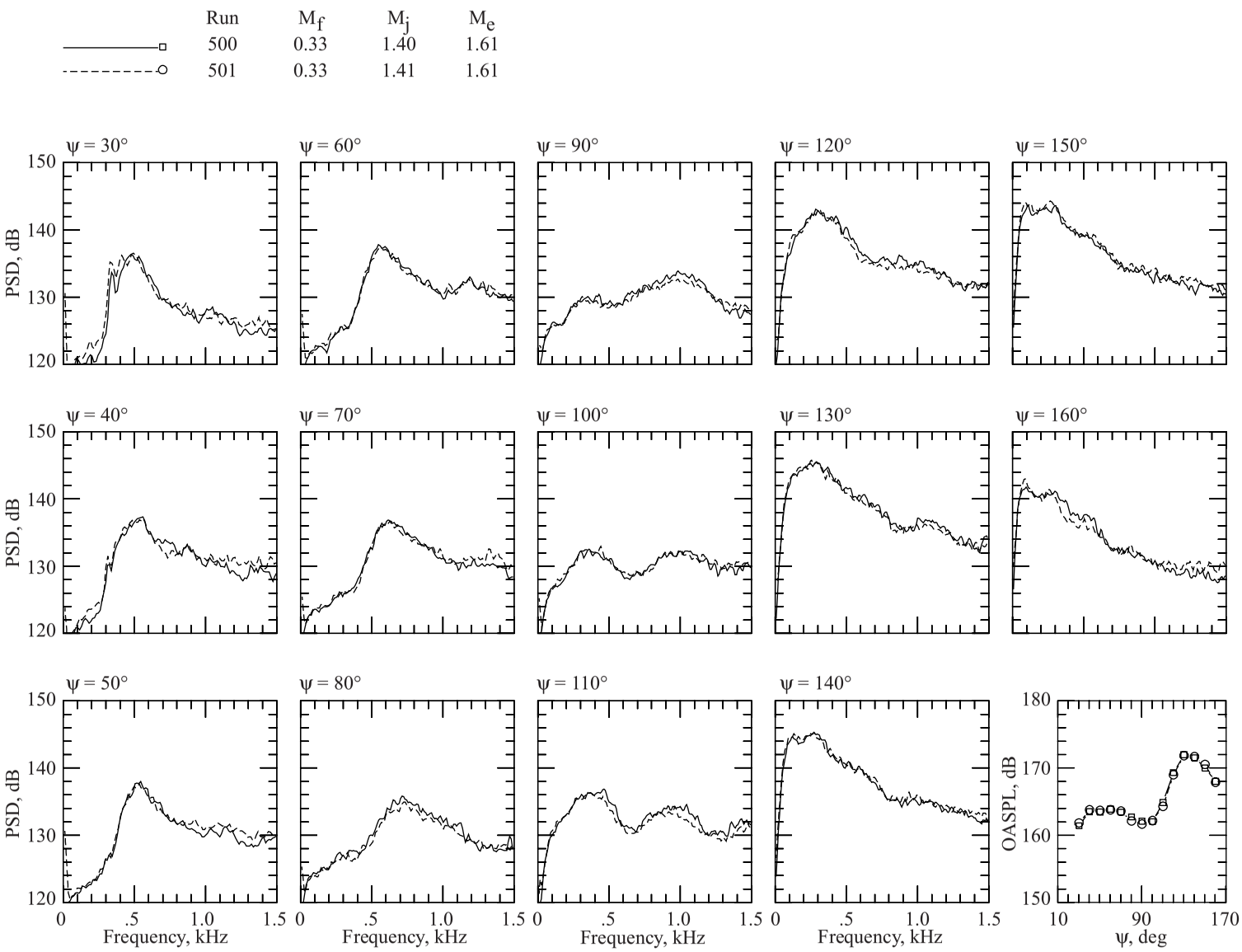
Run
M_f
M_j
M_e
500
0.33
1.40
1.61
501
0.33
1.41
1.61
ψ = 30°
ψ = 60°
ψ = 90°
ψ = 120°
ψ = 150°
ψ = 40°
ψ = 70°
ψ = 100°
ψ = 130°
ψ = 160°
ψ = 50°
ψ = 80°
ψ = 110°
ψ = 140°
PSD, dB
150
140
130
120
0
.5
1.0
1.5
Frequency, kHz
OASPL, dB
180
170
160
150
10
90
170
ψ, deg

Figure B23

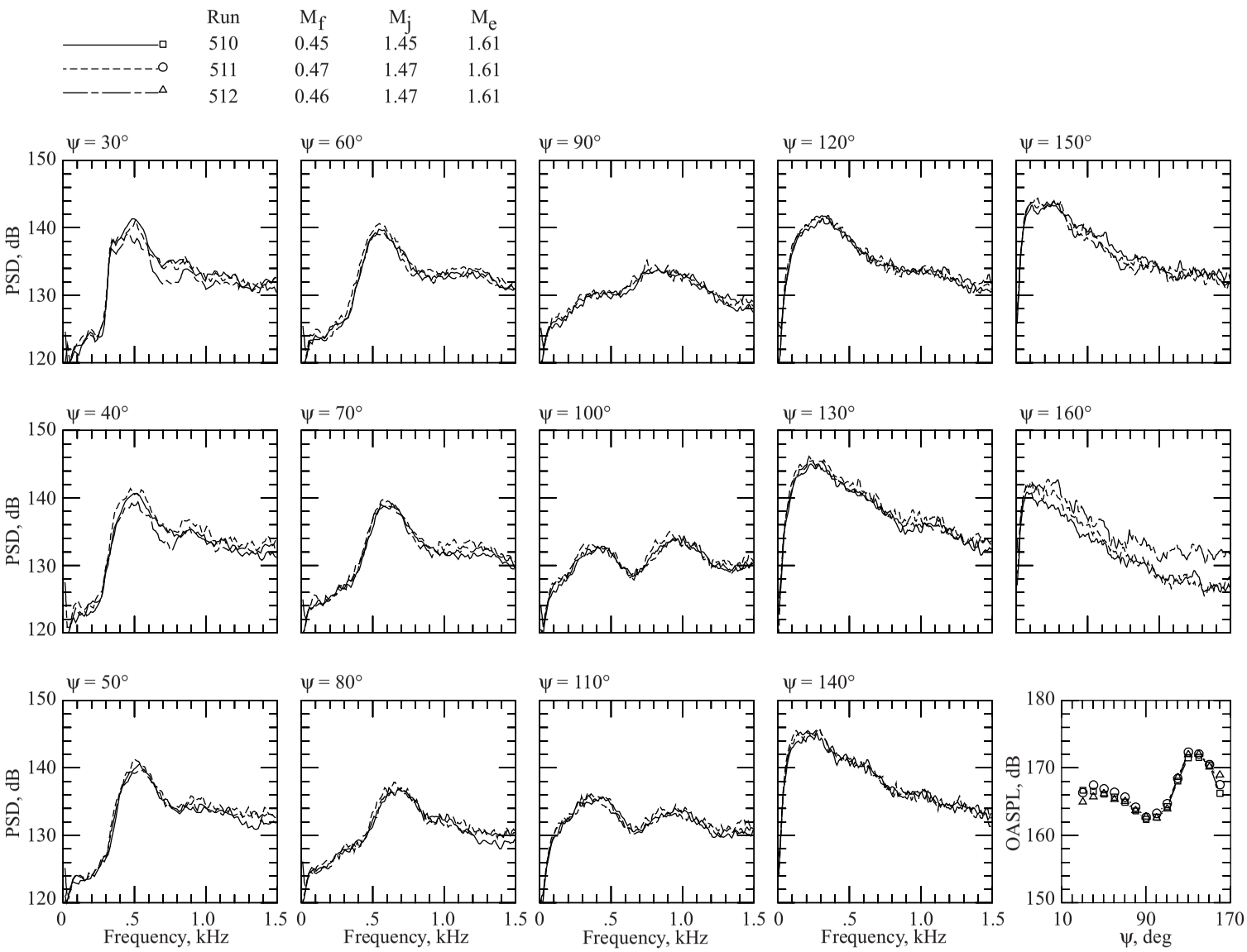
Run
M_f
M_j
M_e
510 0.45 1.45 1.61
511 0.47 1.47 1.61
512 0.46 1.47 1.61
ψ = 30°
ψ = 60°
ψ = 90°
ψ = 120°
ψ = 150°
ψ = 40°
ψ = 70°
ψ = 100°
ψ = 130°
ψ = 160°
ψ = 50°
ψ = 80°
ψ = 110°
ψ = 140°
PSD, dB
150
140
130
120
0
.5
1.0
1.5
Frequency, kHz
OASPL, dB
180
170
160
150
10
90
170
ψ, deg

Figure B24

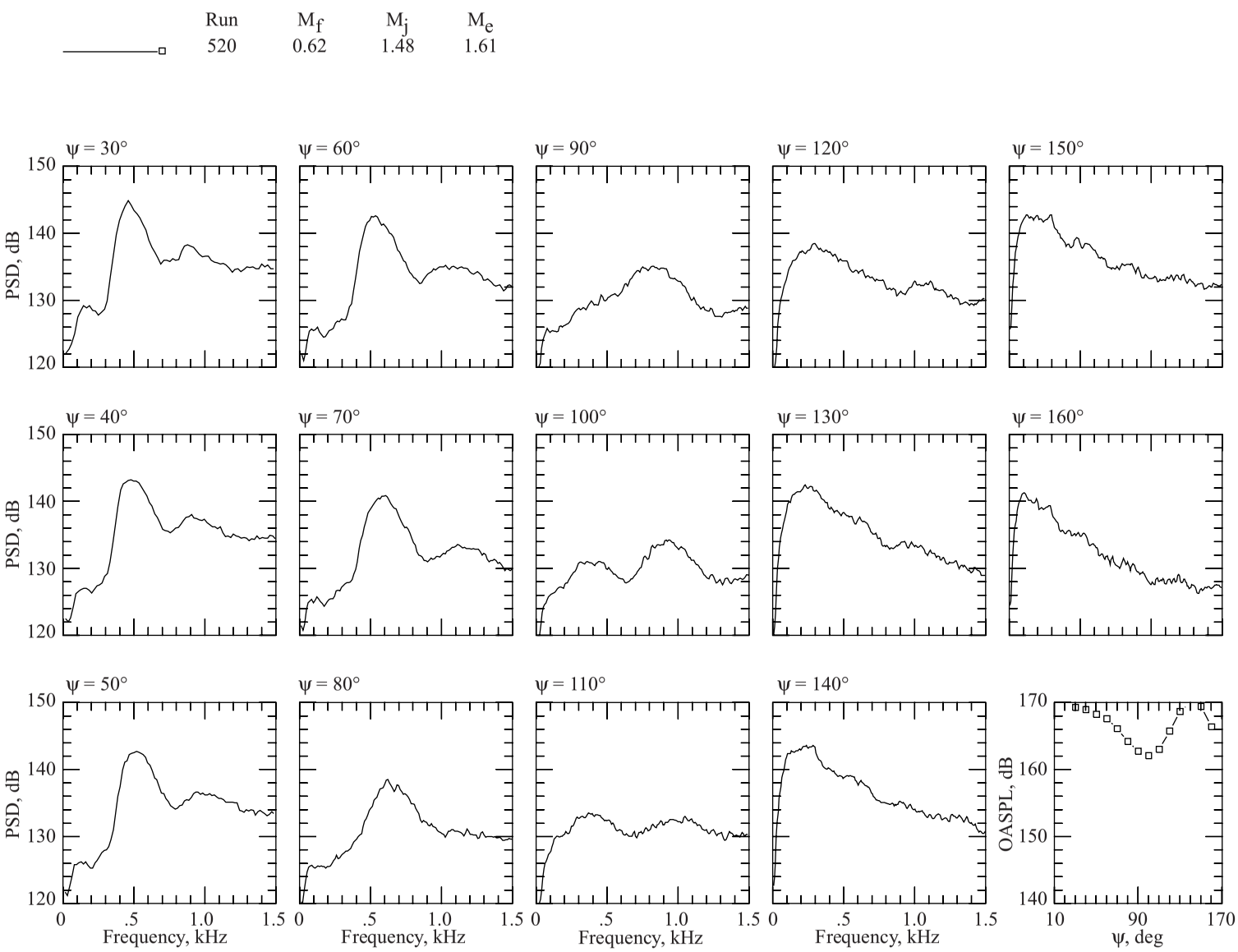
Run
M_f
M_j
M_e
520
0.62
1.48
1.61
ψ = 30°
ψ = 60°
ψ = 90°
ψ = 120°
ψ = 150°
ψ = 40°
ψ = 70°
ψ = 100°
ψ = 130°
ψ = 160°
ψ = 50°
ψ = 80°
ψ = 110°
ψ = 140°
PSD, dB
150
140
130
120
0
.5
1.0
1.5
Frequency, kHz
OASPL, dB
170
160
150
140
10
90
170
ψ, deg

Figure B25

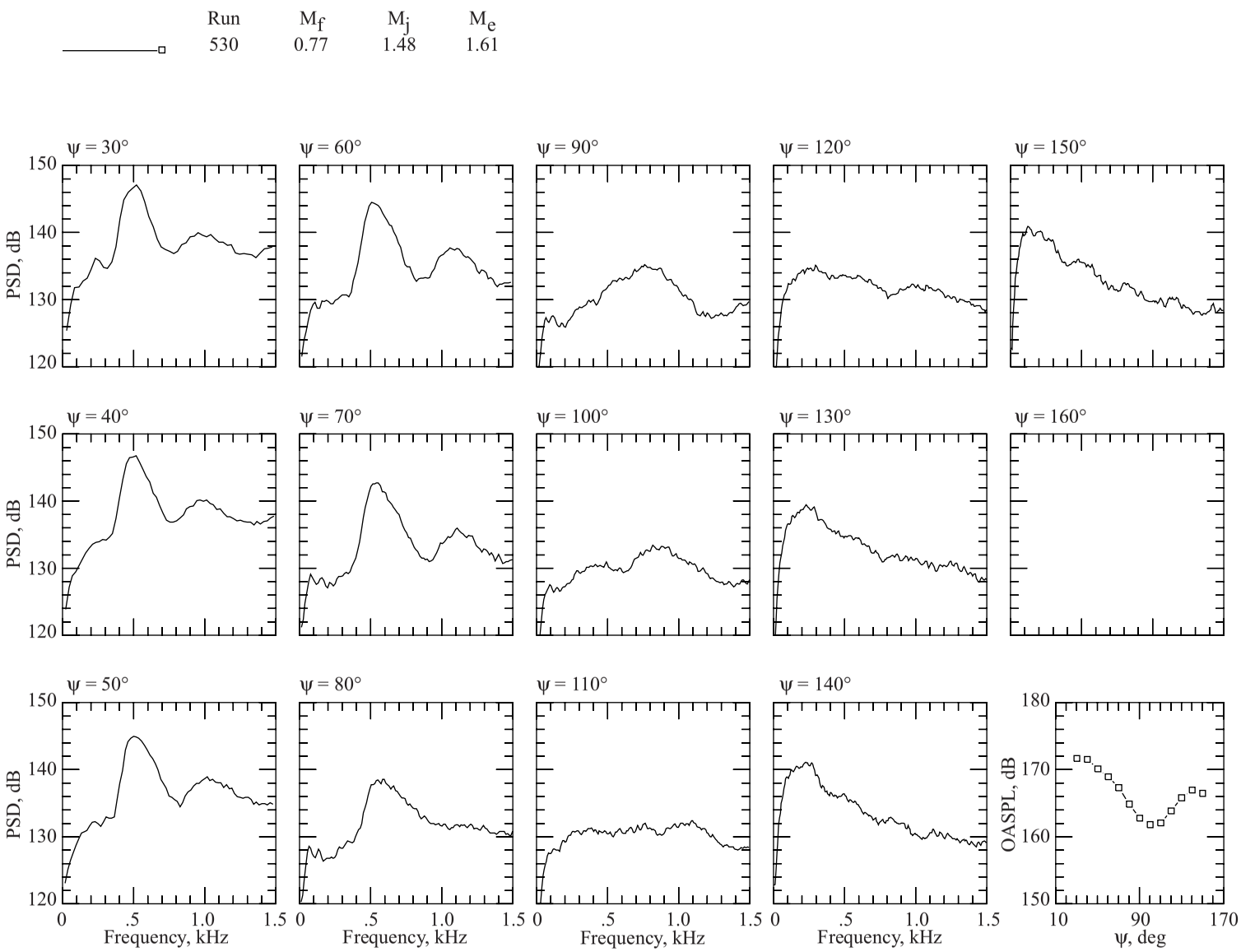
Run
M_f
M_j
M_e
530
0.77
1.48
1.61
ψ = 30°
ψ = 60°
ψ = 90°
ψ = 120°
ψ = 150°
ψ = 40°
ψ = 70°
ψ = 100°
ψ = 130°
ψ = 160°
ψ = 50°
ψ = 80°
ψ = 110°
ψ = 140°
PSD, dB
150
140
130
120
0
.5
1.0
1.5
Frequency, kHz
OASPL, dB
180
170
160
150
10
90
170
ψ, deg

Figure B26

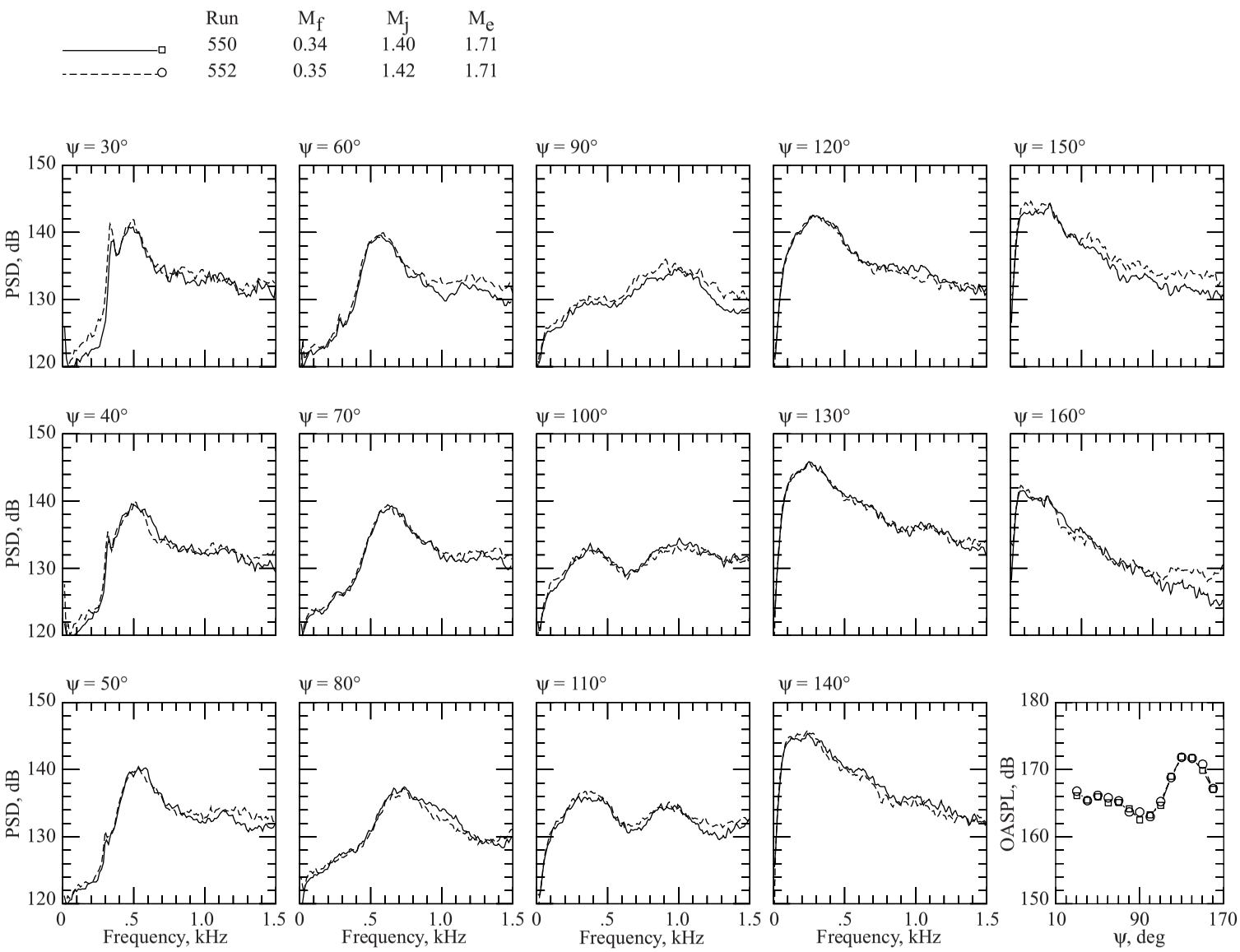
Run
M_f
M_j
M_e
550
0.34
1.40
1.71
552
0.35
1.42
1.71
ψ = 30°
ψ = 60°
ψ = 90°
ψ = 120°
ψ = 150°
ψ = 40°
ψ = 70°
ψ = 100°
ψ = 130°
ψ = 160°
ψ = 50°
ψ = 80°
ψ = 110°
ψ = 140°
PSD, dB
150
140
130
120
0
.5
1.0
1.5
Frequency, kHz
OASPL, dB
180
170
160
150
10
90
170
ψ, deg

Figure B27

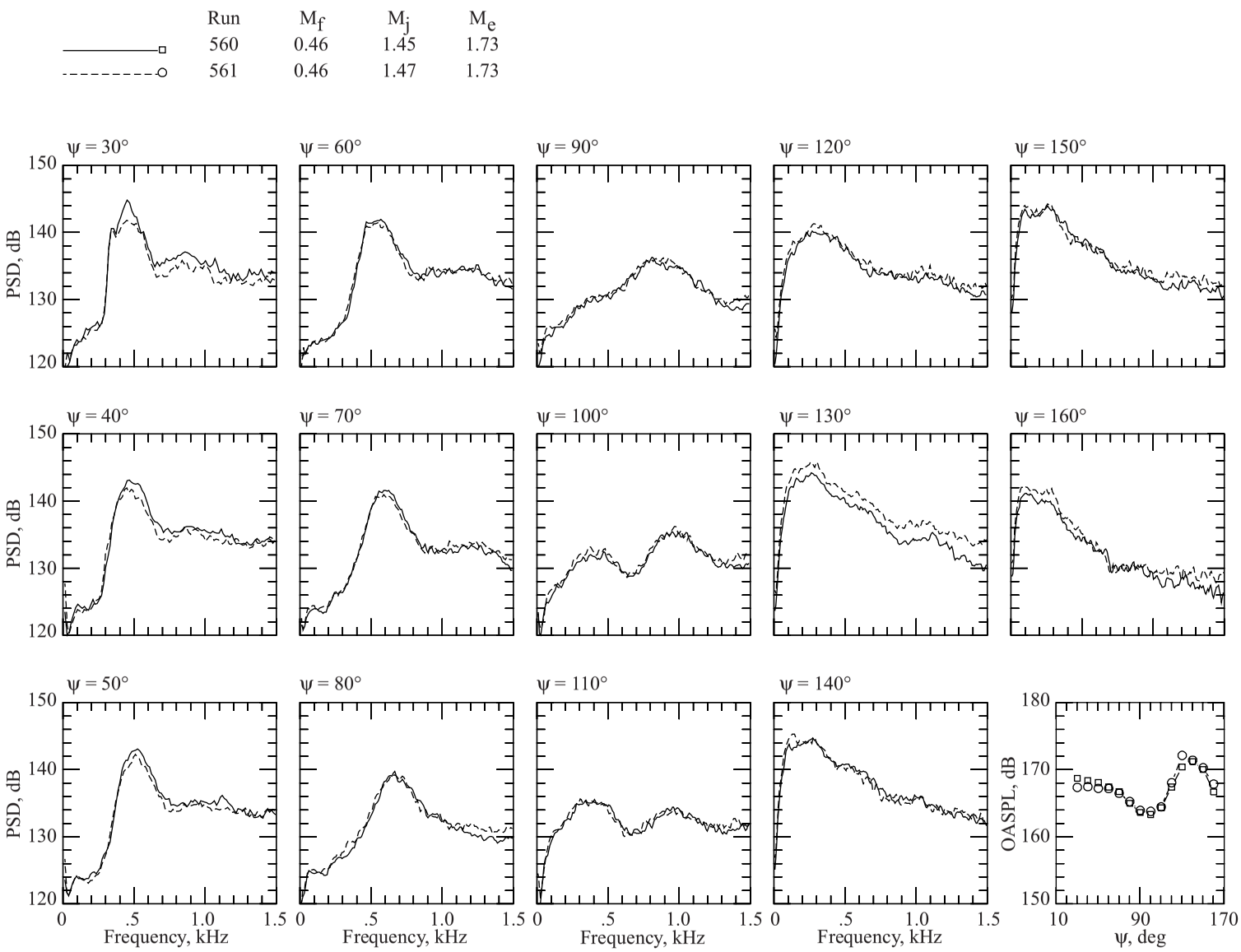
Run
M_f
M_j
M_e
560
0.46
1.45
1.73
561
0.46
1.47
1.73
ψ = 30°
ψ = 60°
ψ = 90°
ψ = 120°
ψ = 150°
ψ = 40°
ψ = 70°
ψ = 100°
ψ = 130°
ψ = 160°
ψ = 50°
ψ = 80°
ψ = 110°
ψ = 140°
PSD, dB
150
140
130
120
0
.5
1.0
1.5
Frequency, kHz
OASPL, dB
180
170
160
150
10
90
170
ψ, deg

Figure B28

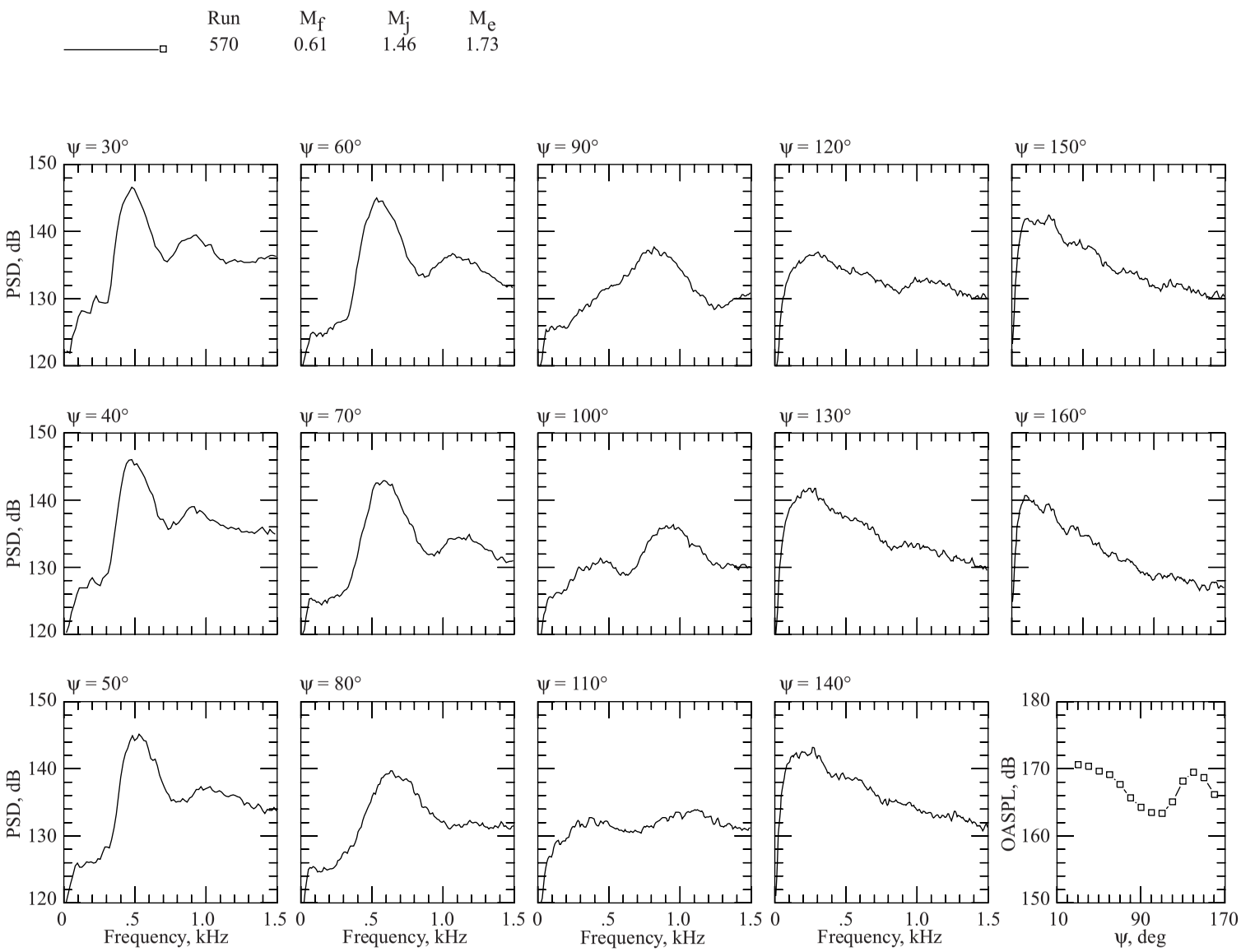
Run
M_f
M_j
M_e
570
0.61
1.46
1.73
ψ = 30°
ψ = 60°
ψ = 90°
ψ = 120°
ψ = 150°
ψ = 40°
ψ = 70°
ψ = 100°
ψ = 130°
ψ = 160°
ψ = 50°
ψ = 80°
ψ = 110°
ψ = 140°
PSD, dB
150
140
130
120
0
.5
1.0
1.5
Frequency, kHz
OASPL, dB
180
170
160
150
10
90
170
ψ, deg

Figure B29

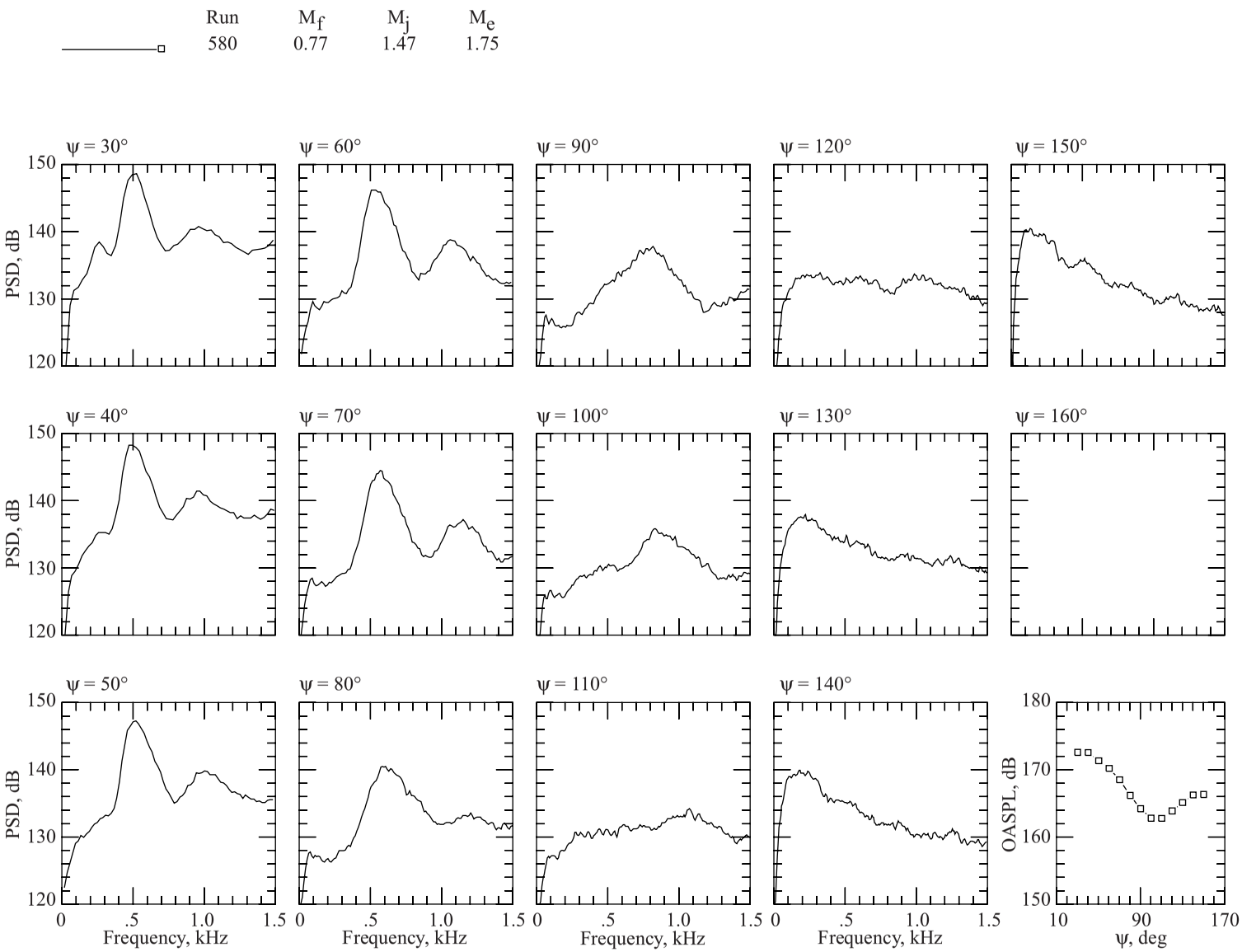
Run
M_f
M_j
M_e
580
0.77
1.47
1.75
ψ = 30°
ψ = 60°
ψ = 90°
ψ = 120°
ψ = 150°
ψ = 40°
ψ = 70°
ψ = 100°
ψ = 130°
ψ = 160°
ψ = 50°
ψ = 80°
ψ = 110°
ψ = 140°
PSD, dB
150
140
130
120
0
.5
1.0
1.5
Frequency, kHz
OASPL, dB
180
170
160
150
10
90
170
ψ, deg

Figure B30

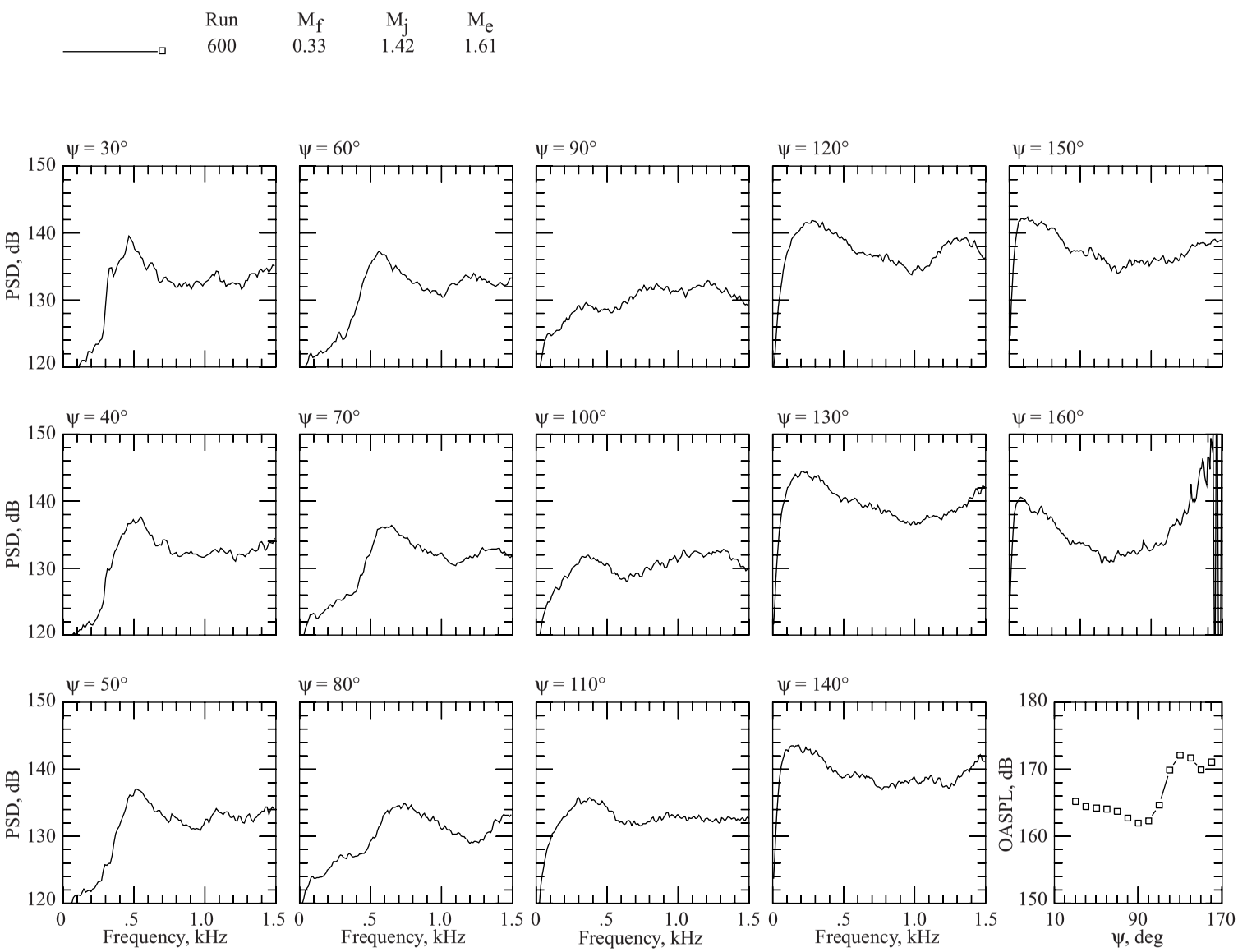
Run
600
M_f
0.33
M_j
1.42
M_e
1.61
ψ = 30°
ψ = 60°
ψ = 90°
ψ = 120°
ψ = 150°
ψ = 40°
ψ = 70°
ψ = 100°
ψ = 130°
ψ = 160°
ψ = 50°
ψ = 80°
ψ = 110°
ψ = 140°
PSD, dB
150
140
130
120
0
.5
1.0
1.5
Frequency, kHz
OASPL, dB
180
170
160
150
10
90
170
ψ, deg

Figure B31

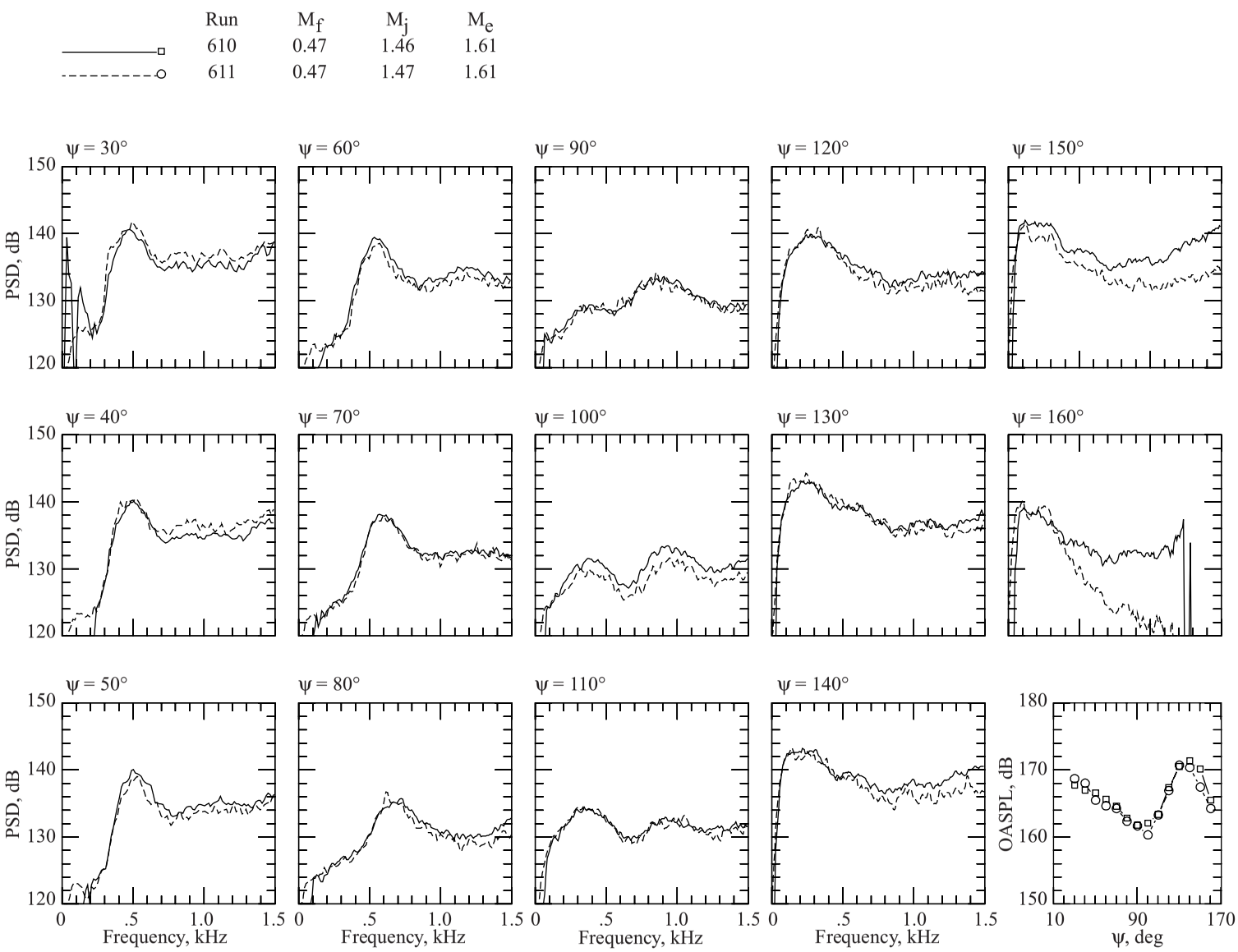
Run
M_f
M_j
M_e
610
0.47
1.46
1.61
611
0.47
1.47
1.61
ψ = 30°
ψ = 60°
ψ = 90°
ψ = 120°
ψ = 150°
ψ = 40°
ψ = 70°
ψ = 100°
ψ = 130°
ψ = 160°
ψ = 50°
ψ = 80°
ψ = 110°
ψ = 140°
PSD, dB
150
140
130
120
0
.5
1.0
1.5
Frequency, kHz
OASPL, dB
180
170
160
150
10
90
170
ψ, deg

Figure B32

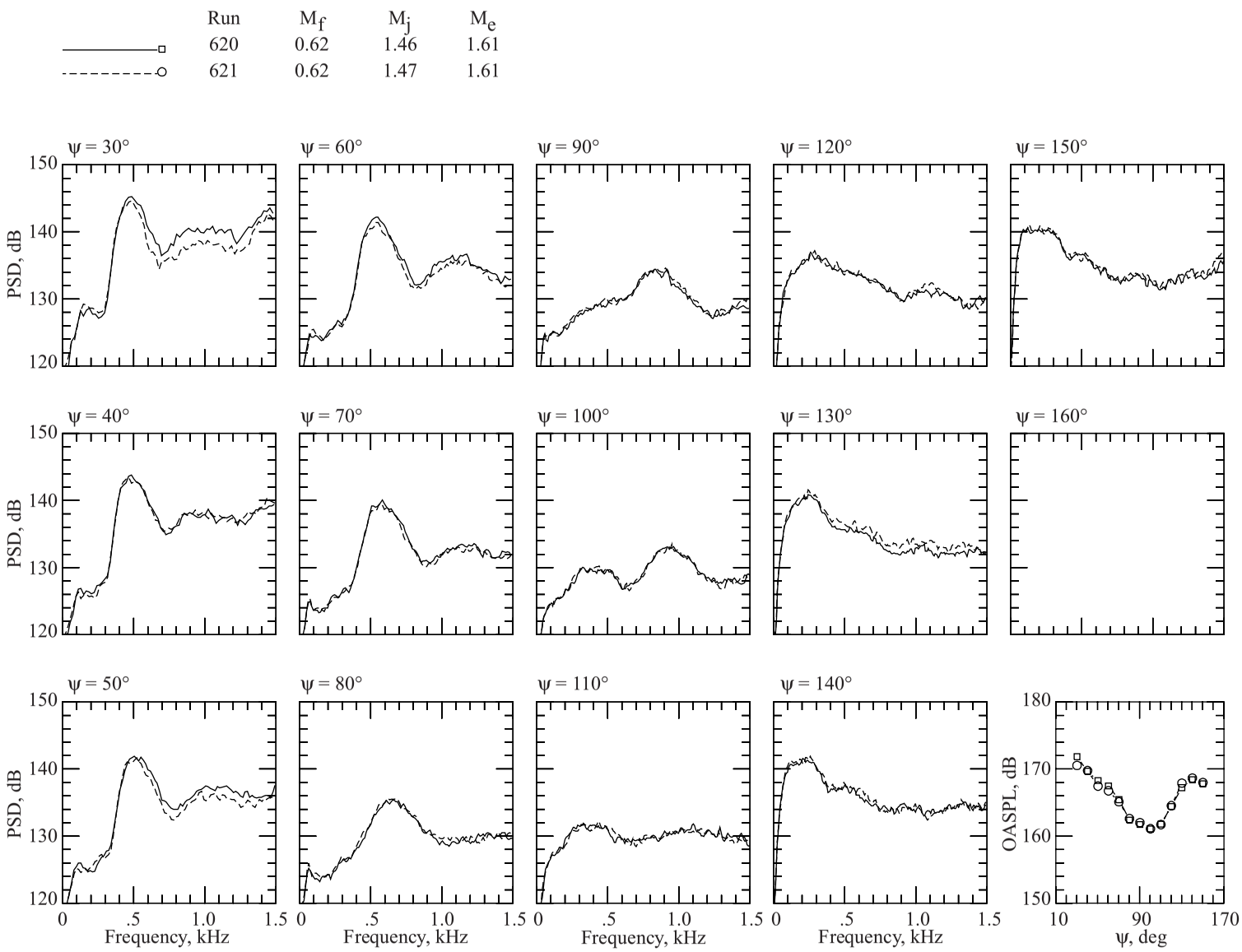
Run
M_f
M_j
M_e
620
0.62
1.46
1.61
621
0.62
1.47
1.61
ψ = 30°
ψ = 60°
ψ = 90°
ψ = 120°
ψ = 150°
ψ = 40°
ψ = 70°
ψ = 100°
ψ = 130°
ψ = 160°
ψ = 50°
ψ = 80°
ψ = 110°
ψ = 140°
PSD, dB
150
140
130
120
0
.5
1.0
1.5
Frequency, kHz
OASPL, dB
180
170
160
150
10
90
170
ψ, deg

Figure B33

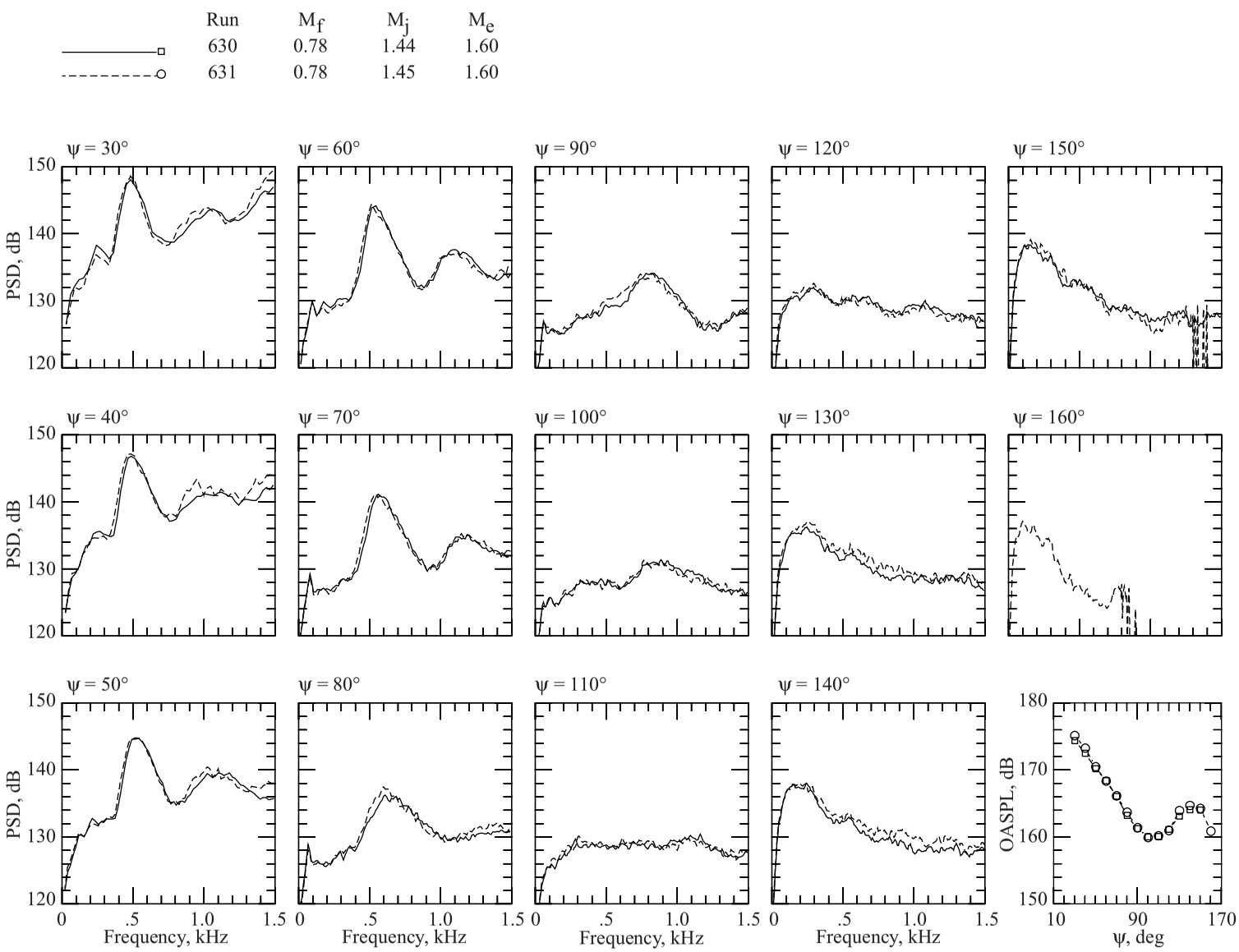
Run
630
631
M_f
0.78
0.78
M_j
1.44
1.45
M_e
1.60
1.60
ψ = 30°
ψ = 60°
ψ = 90°
ψ = 120°
ψ = 150°
ψ = 40°
ψ = 70°
ψ = 100°
ψ = 130°
ψ = 160°
ψ = 50°
ψ = 80°
ψ = 110°
ψ = 140°
PSD, dB
150
140
130
120
0
.5
1.0
1.5
Frequency, kHz
OASPL, dB
180
170
160
150
10
90
170
ψ, deg

Figure B34

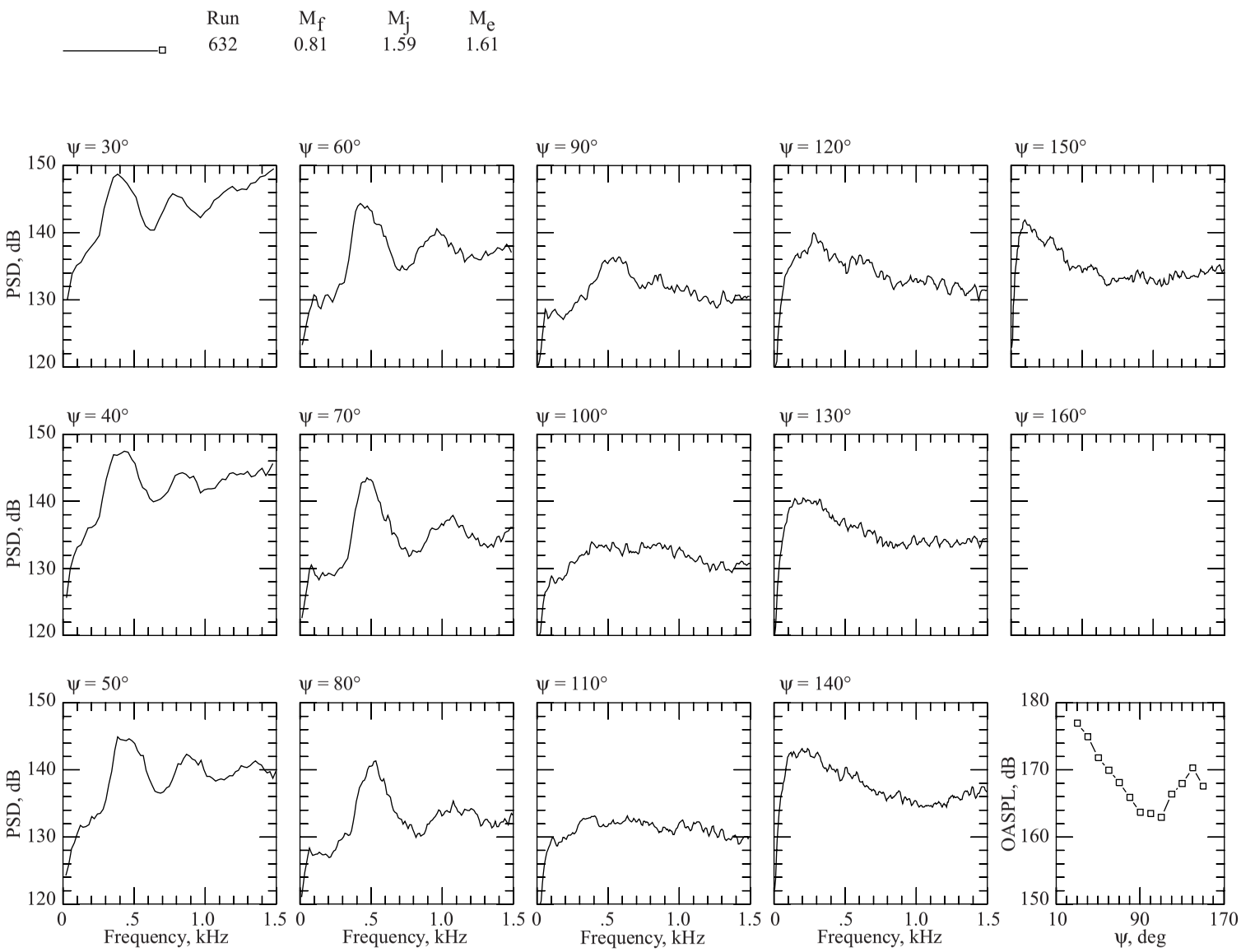
Run
M_f
M_j
M_e
632
0.81
1.59
1.61
ψ = 30°
ψ = 60°
ψ = 90°
ψ = 120°
ψ = 150°
ψ = 40°
ψ = 70°
ψ = 100°
ψ = 130°
ψ = 160°
ψ = 50°
ψ = 80°
ψ = 110°
ψ = 140°
PSD, dB
150
140
130
120
0
.5
1.0
1.5
Frequency, kHz
OASPL, dB
180
170
160
150
10
90
170
ψ, deg

Figure B35

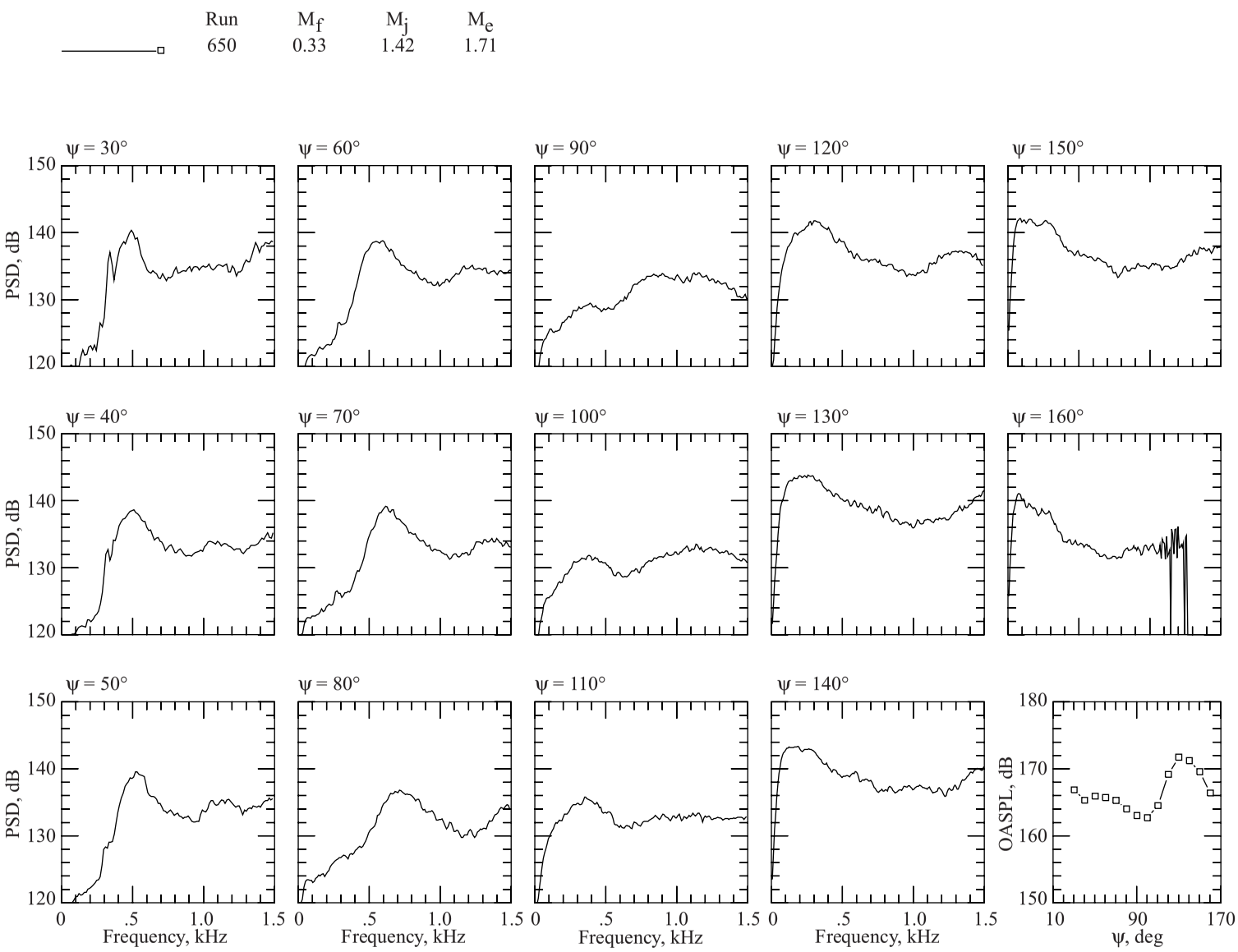
Run
650
M_f
0.33
M_j
1.42
M_e
1.71
ψ = 30°
ψ = 60°
ψ = 90°
ψ = 120°
ψ = 150°
ψ = 40°
ψ = 70°
ψ = 100°
ψ = 130°
ψ = 160°
ψ = 50°
ψ = 80°
ψ = 110°
ψ = 140°
PSD, dB
150
140
130
120
0
.5
1.0
1.5
Frequency, kHz
OASPL, dB
180
170
160
150
10
90
170
ψ, deg

Figure B36

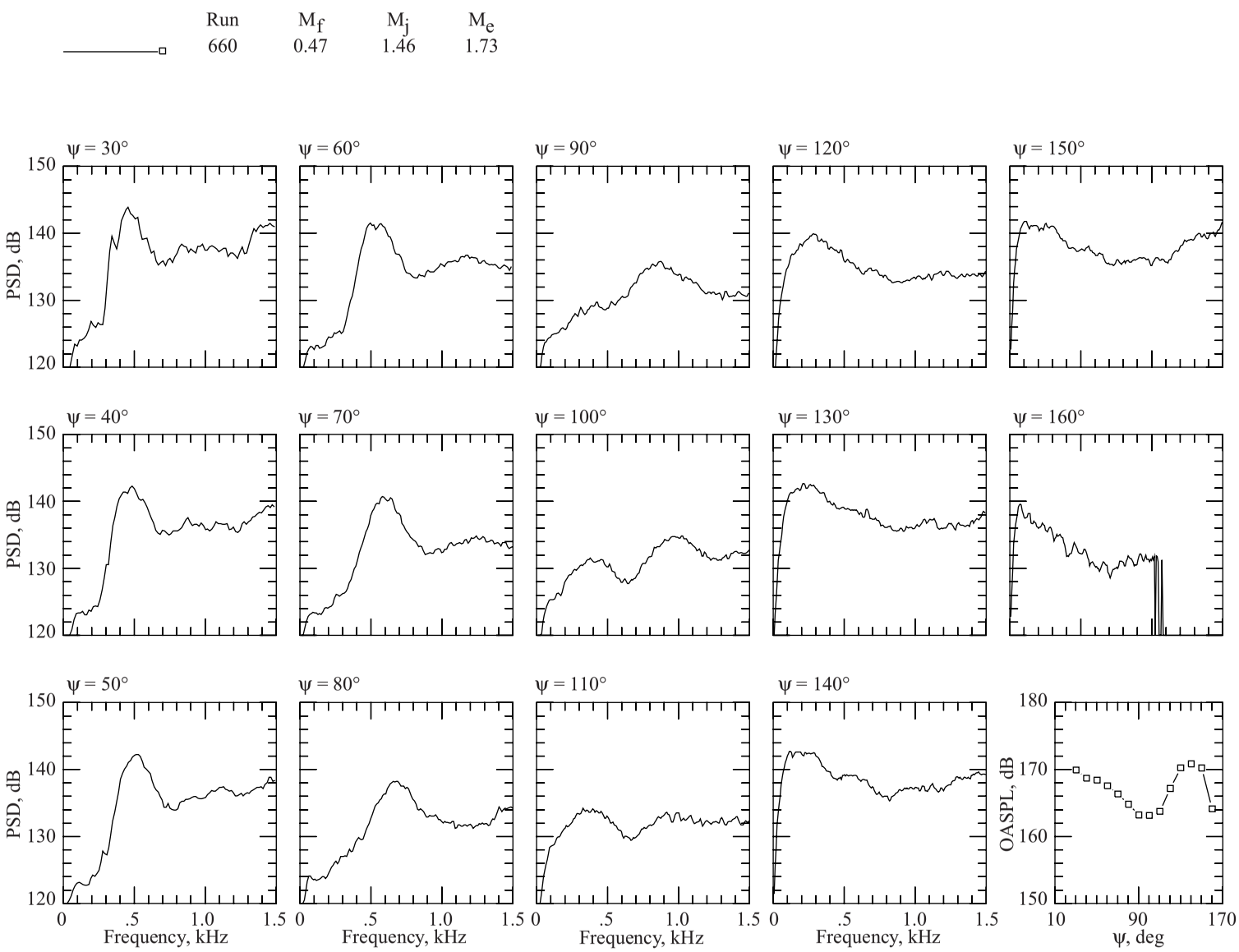
Run
660
M_f
0.47
M_j
1.46
M_e
1.73
ψ = 30°
ψ = 60°
ψ = 90°
ψ = 120°
ψ = 150°
ψ = 40°
ψ = 70°
ψ = 100°
ψ = 130°
ψ = 160°
ψ = 50°
ψ = 80°
ψ = 110°
ψ = 140°
PSD, dB
150
140
130
120
0
.5
1.0
1.5
Frequency, kHz
OASPL, dB
180
170
160
150
10
90
170
ψ, deg

Figure B37

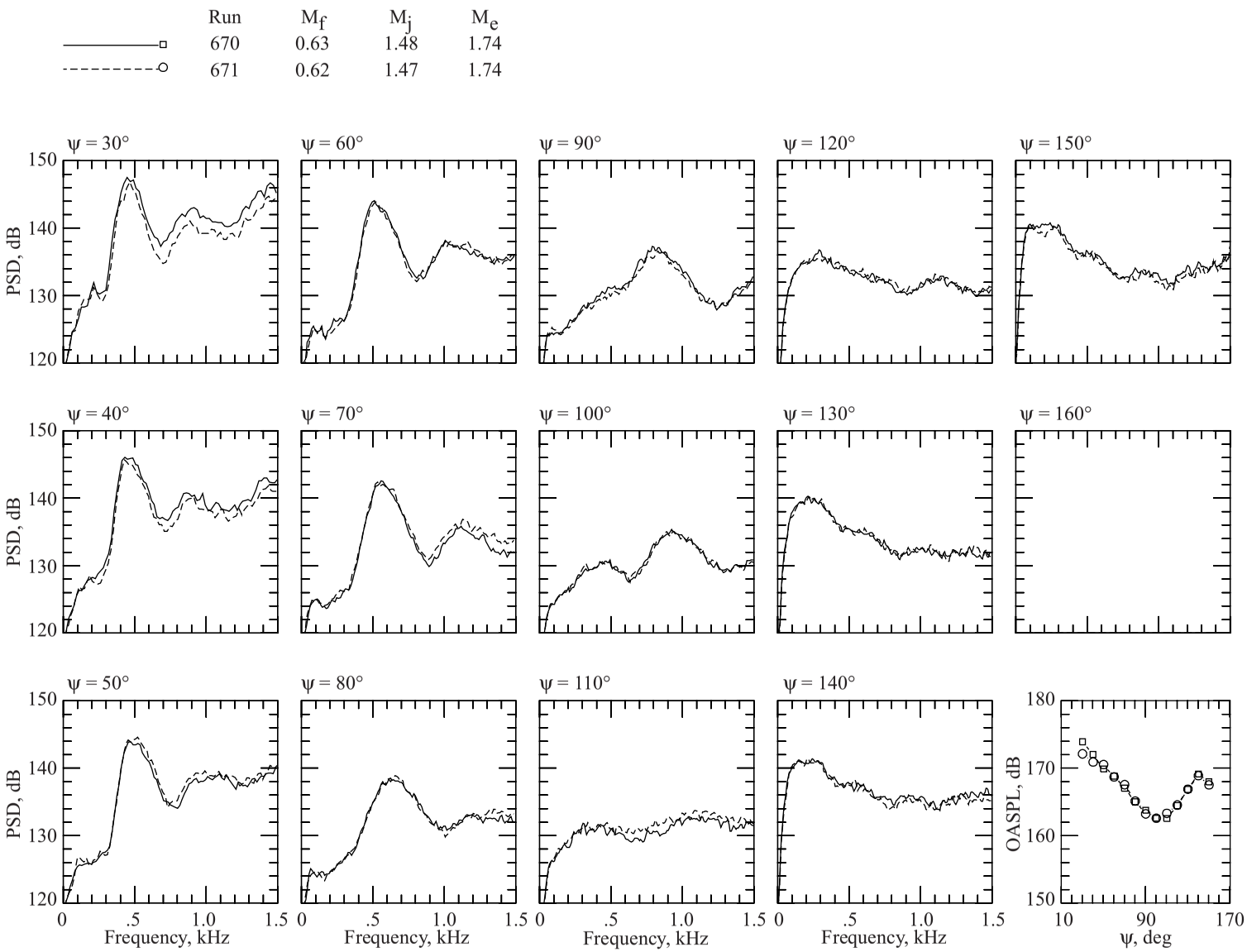
Run
M_f
M_j
M_e
670 0.63 1.48 1.74
671 0.62 1.47 1.74
ψ = 30°
ψ = 60°
ψ = 90°
ψ = 120°
ψ = 150°
ψ = 40°
ψ = 70°
ψ = 100°
ψ = 130°
ψ = 160°
ψ = 50°
ψ = 80°
ψ = 110°
ψ = 140°
PSD, dB
150
140
130
120
0
.5
1.0
1.5
Frequency, kHz
OASPL, dB
180
170
160
150
10
90
170
ψ, deg

Figure B38

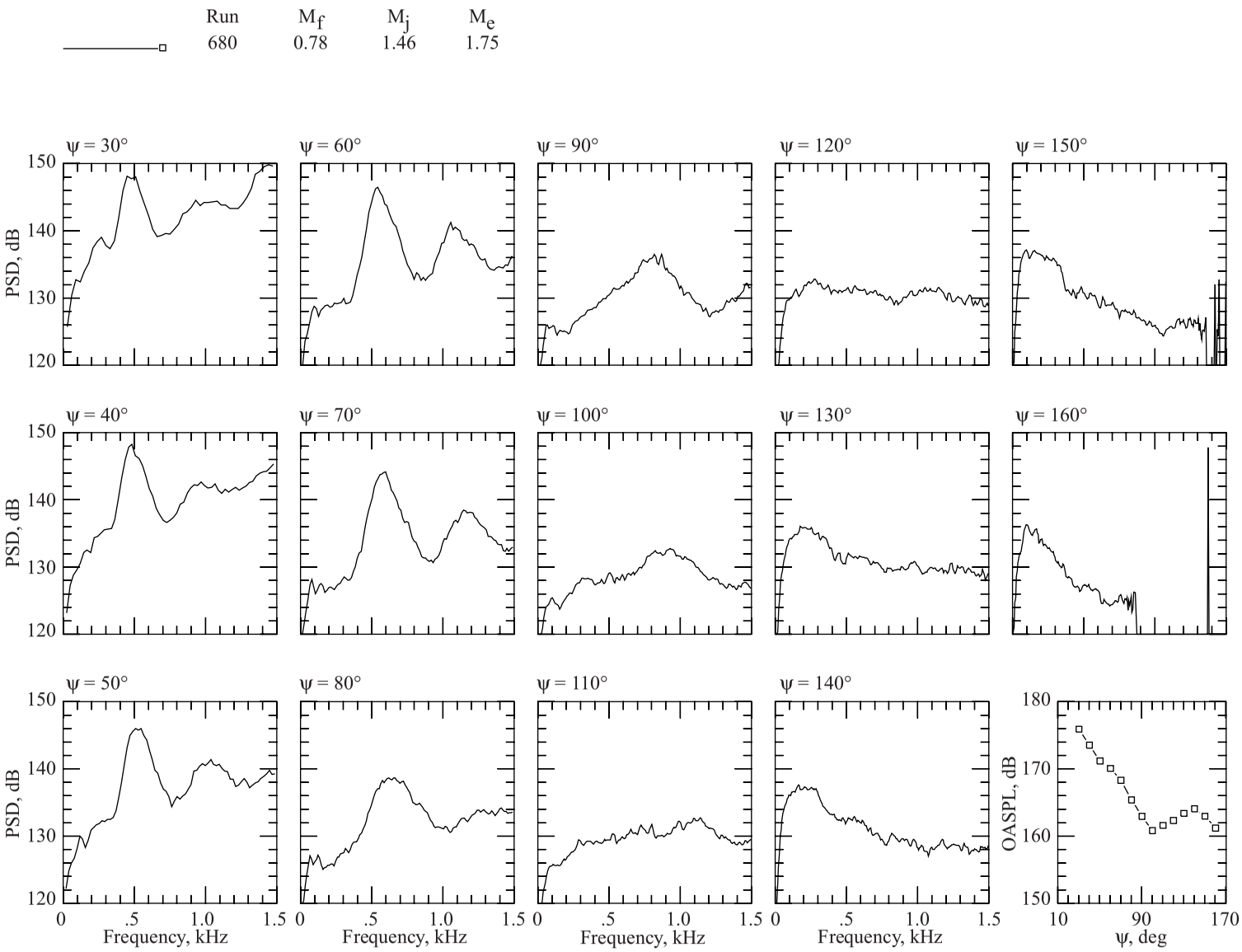
Run
680
M_f
0.78
M_j
1.46
M_e
1.75
ψ = 30°
ψ = 60°
ψ = 90°
ψ = 120°
ψ = 150°
ψ = 40°
ψ = 70°
ψ = 100°
ψ = 130°
ψ = 160°
ψ = 50°
ψ = 80°
ψ = 110°
ψ = 140°
PSD, dB
150
140
130
120
0
.5
1.0
1.5
Frequency, kHz
OASPL, dB
180
170
160
150
10
90
170
ψ, deg

Figure B39

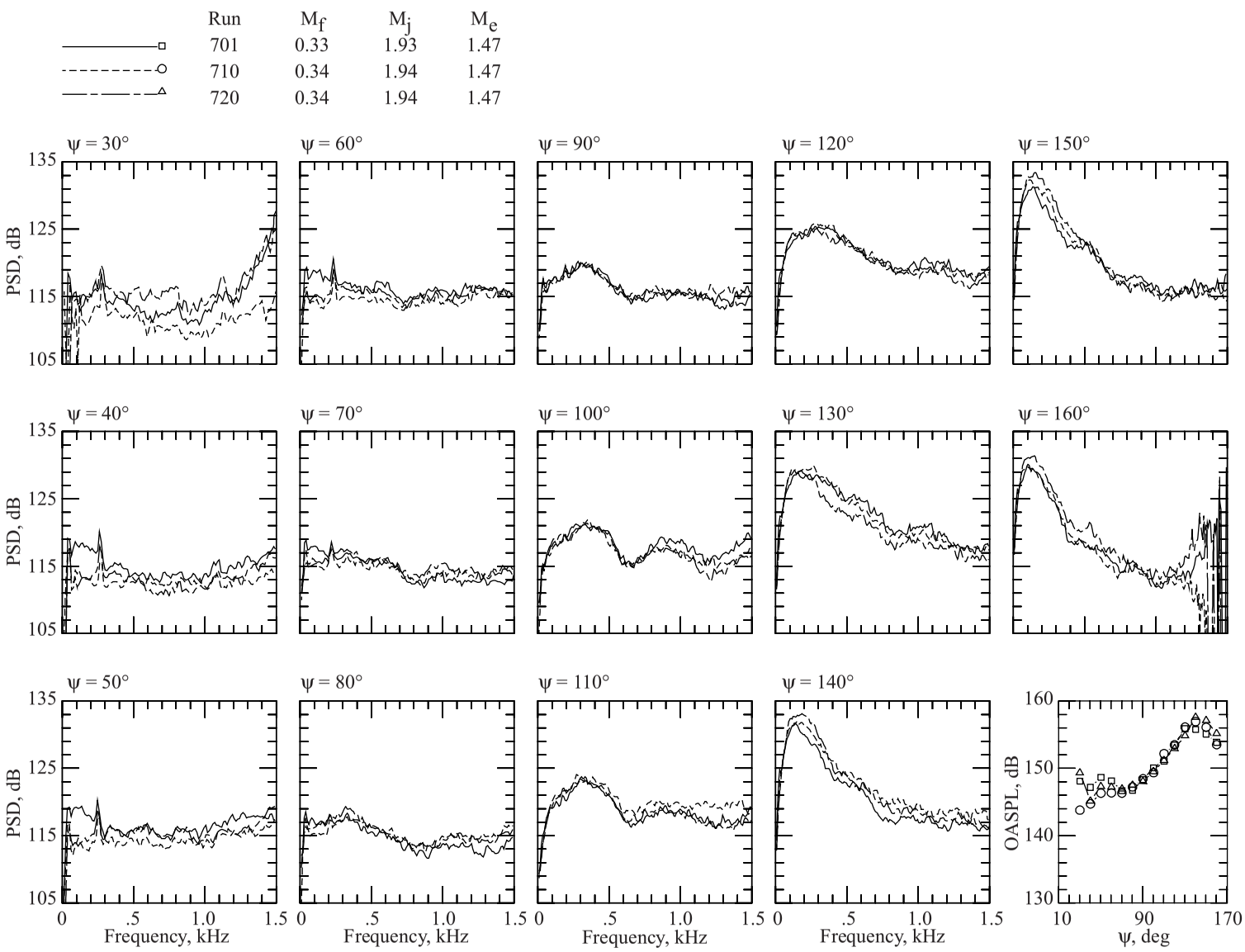
Run
M_f
M_j
M_e
701 0.33 1.93 1.47
710 0.34 1.94 1.47
720 0.34 1.94 1.47
ψ = 30°
ψ = 60°
ψ = 90°
ψ = 120°
ψ = 150°
ψ = 40°
ψ = 70°
ψ = 100°
ψ = 130°
ψ = 160°
ψ = 50°
ψ = 80°
ψ = 110°
ψ = 140°
PSD, dB
135
125
115
105
0
.5
1.0
1.5
Frequency, kHz
OASPL, dB
160
150
140
130
10
90
170
ψ, deg

Figure B40

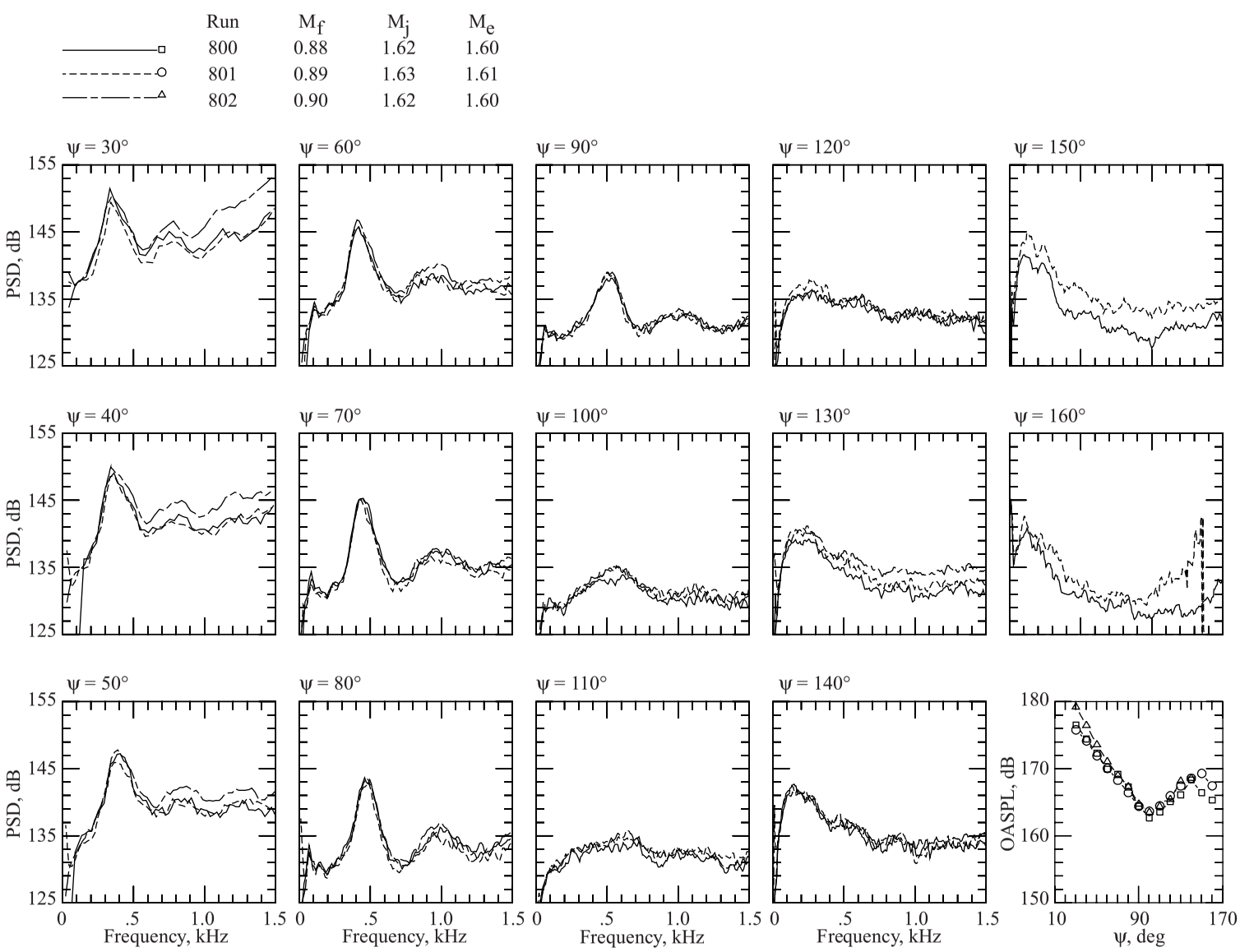
Run
M_f
M_j
M_e
800 0.88 1.62 1.60
801 0.89 1.63 1.61
802 0.90 1.62 1.60
ψ = 30°
ψ = 60°
ψ = 90°
ψ = 120°
ψ = 150°
ψ = 40°
ψ = 70°
ψ = 100°
ψ = 130°
ψ = 160°
ψ = 50°
ψ = 80°
ψ = 110°
ψ = 140°
PSD, dB
155
145
135
125
0
.5
1.0
1.5
Frequency, kHz
OASPL, dB
180
170
160
150
10
90
170
ψ, deg

Figure B41

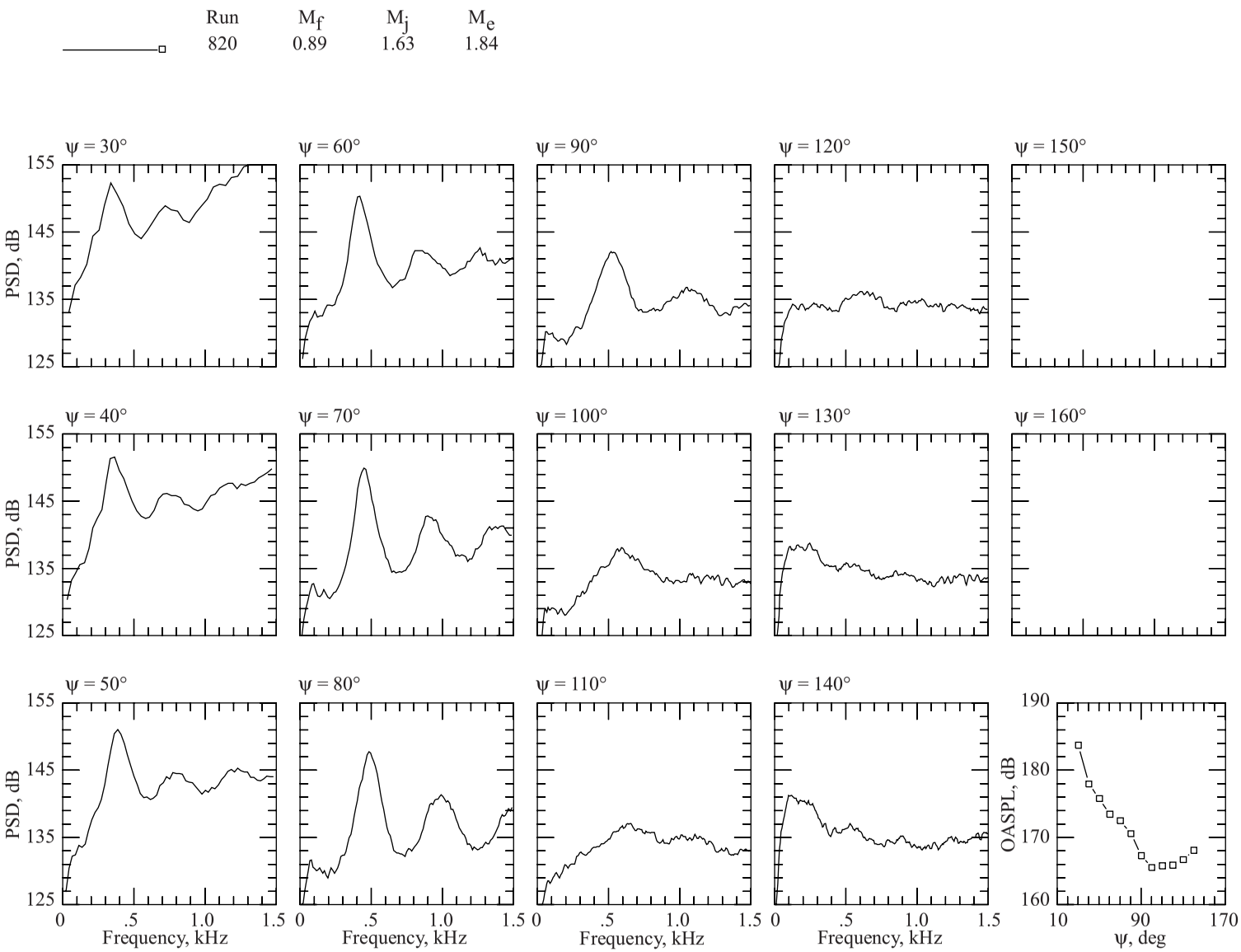
Run
820
M_f
0.89
M_j
1.63
M_e
1.84
ψ = 30°
ψ = 60°
ψ = 90°
ψ = 120°
ψ = 150°
ψ = 40°
ψ = 70°
ψ = 100°
ψ = 130°
ψ = 160°
ψ = 50°
ψ = 80°
ψ = 110°
ψ = 140°
PSD, dB
155
145
135
125
0
.5
1.0
1.5
Frequency, kHz
OASPL, dB
190
180
170
160
10
90
170
ψ, deg

Figure B42

Appendix C

Derivation of Tam's Doppler Factor Exponent

In the shock noise predictions of Tam (ref. 6), the Doppler factor exponent is unclear due to the use of reception coordinates rather than emission coordinates. Tam's dynamic amplification factor is given as

$$R_r^2\left(1 - M_f^2 \sin^2 \psi_r\right) \tag{C1}$$

To transform this expression to emission coordinates, we use the relations

$$R_r \sin \psi_r = R \sin \psi \quad \text{and} \quad \tan \psi_r = \frac{\sin \psi}{\cos \psi - M_f} \tag{C2}$$

Introducing the factor

$$\varsigma = \sqrt{1 - 2M_f \cos \psi + M_f^2} \tag{C3}$$

reduces equations (C2) to

$$R_r = \varsigma R \quad \text{and} \quad \sin \psi_r = \varsigma^{-1} \sin \psi \tag{C4}$$

and the dynamic amplification factor (C1) to

$$R^2 (1 - M_f \cos \psi)^2 \tag{C5}$$

Hence, Tam's prediction for the dynamic amplification factor reduces to the standard Doppler factor with an exponent $m = 2$.

REPORT DOCUMENTATION PAGE

Form Approved
OMB No. 0704-0188

1. REPORT DATE *(DD-MM-YYYY)*	2. REPORT TYPE	3. DATES COVERED *(From - To)*
01- 01 - 2004	Technical Publication	

4. TITLE AND SUBTITLE
Supersonic Jet Exhaust Noise at High Subsonic Flight Speed

5a. CONTRACT NUMBER

5b. GRANT NUMBER

5c. PROGRAM ELEMENT NUMBER

6. AUTHOR(S)
Norum, Thomas D.; Garber, Donald P.; Golub, Robert A.; Santa Maria, Odilyn L.; and Orme, John S.

5d. PROJECT NUMBER

5e. TASK NUMBER

5f. WORK UNIT NUMBER
23-781-30-12

7. PERFORMING ORGANIZATION NAME(S) AND ADDRESS(ES)
NASA Langley Research Center
Hampton, VA 23681-2199

8. PERFORMING ORGANIZATION REPORT NUMBER
L-18319

9. SPONSORING/MONITORING AGENCY NAME(S) AND ADDRESS(ES)
National Aeronautics and Space Administration
Washington, DC 20546-0001

10. SPONSOR/MONITOR'S ACRONYM(S)
NASA

11. SPONSOR/MONITOR'S REPORT NUMBER(S)
NASA/TP-2004-212686

12. DISTRIBUTION/AVAILABILITY STATEMENT
Unclassified - Unlimited
Subject Category 71
Availability: NASA CASI (301) 621-0390 Distribution: Standard

13. SUPPLEMENTARY NOTES
Norum, Garber, Golub, Santa Maria, Langley Research Center. Orme, Dryden Flight Research Center.
An electronic version can be found at http://techreports.larc.nasa.gov/ltrs/ or http://ntrs.nasa.gov

14. ABSTRACT

An empirical model to predict the effects of flight on the noise from a supersonic transport is developed. This model is based on an analysis of the exhaust jet noise from high subsonic flights of the F-15 ACTIVE Aircraft. Acoustic comparisons previously attainable only in a wind tunnel were accomplished through the control of both flight operations and exhaust nozzle exit diameter. Independent parametric variations of both flight and exhaust jet Mach numbers at given supersonic nozzle pressure ratios enabled excellent correlations to be made for both jet broadband shock noise and jet mixing noise at flight speeds up to Mach 0.8. Shock noise correlated with flight speed and emission angle through a Doppler factor exponent of about 2.6. Mixing noise at all downstream angles was found to correlate well with a jet relative velocity exponent of about 7.3, with deviations from this behavior only at supersonic eddy convection speeds and at very high flight Mach numbers. The acoustic database from the flight test is also provided.

15. SUBJECT TERMS
Supersonic jet noise; Jet shock noise in flight; Jet mixing noise in flight

16. SECURITY CLASSIFICATION OF:			17. LIMITATION OF ABSTRACT	18. NUMBER OF PAGES	19a. NAME OF RESPONSIBLE PERSON
a. REPORT	b. ABSTRACT	c. THIS PAGE			STI Help Desk (email: help@sti.nasa.gov)
					19b. TELEPHONE NUMBER *(Include area code)*
U	U	U	UU	90	(301) 621-0390